# 行政院原子能委員會

# 委託研究計畫研究報告

## SOFC 電池堆接合件高溫耐久機械性能分析(II)

## Analysis of High-Temperature Mechanical Durability of SOFC Stack Joints (II)

# 目錄

## 中文摘要

　　本研究主旨在探討經過不同時效處理之 GC-9 封裝玻璃陶瓷燒結試片，在 800 $^o$C 下的潛變性質與破壞模式，並探討金屬連接板不銹鋼(Crofer 22 H)與封裝玻璃陶瓷接合件於 800 $^o$C 下之潛變性質與不同負載模式下之破壞形態。實驗結果顯示，經過 1000 小時時效處理後之 GC-9 玻璃陶瓷燒結試片，於相同的應力負載下，其變形量比未時效及 100 小時時效之試片來得低且具有較長的潛變壽命，此乃於結晶量較多及粗大化所致。藉由最小應變率來看，未時效試片之最小應變率明顯高於其時效處理後的試片，由此可證，時效時間越長，抵抗潛變變形的能力越高。在潛變壽命方面，欲達到 1000 小時以上之壽命，未時效、100 小時時效及 1000 小時時效所施加的應力負載分別需小於 6 MPa、9 MPa 及 15 MPa，再次證明經由時效過後的試片，所能承受之負載較大，抵抗潛變變形的能力越高。關於 GC-9 玻璃陶瓷與 Crofer 22 H 金屬連接板接合件的潛變性質，接合件試片於 800 $^o$C 下的剪力與拉力潛變壽命會隨著負載減少而增加。在剪力試片方面，具 1000 小時壽命的潛變強度約為剪力接合件強度的四分之一，而張力試片具 1000 小時壽命的潛變強度則約為張力接合件強度的百分之九。另外，對於剪力及張力潛變試片，不論其潛變壽命長短，其裂紋皆始於尖晶石與鉻酸鋇層之界面，隨後沿著鉻酸鋇層生長，而後在鉻酸鋇層與玻璃陶瓷基材之間交替遊走，最後在玻璃陶瓷基材內發生破壞。另外，本研究亦利用微硬度壓痕法對 SOFC 電極片的破裂韌性值進行初步的量測。

**Abstract**

Creep properties at 800 $^{\circ}$C are investigated for a newly developed solid oxide fuel cell glass-ceramic sealant (GC-9) in variously aged conditions using a ring-on-ring test technique. Creep properties of sandwich joint specimens made of GC-9 and a interconnect steel (Crofer 22 H) are also investigated at 800 $^{\circ}$C under several constant shear and tensile loadings. When subjected to an applied constant load at 800 $^{\circ}$C, the 1000 h-aged GC-9 can last longer than the non-aged and 100 h-aged ones before rupture. The 1000 h-aged GC-9 also exhibits a much smaller minimum creep strain rate than do the non-aged and 100 h-aged ones. Therefore, a longer aging time of 1000 h leads to a greater extent of crystallization and creep resistance at 800 $^{\circ}$C for the given GC-9 glass-ceramic sealant. The creep strength at 1000 h is about 6 MPa, 9 MPa, and 15 MPa, for the non-aged, 100 h-aged, and 1000 h-aged GC-9, respectively.

The creep rupture time of Crofer 22 H/GC-9/Crofer 22 H joint specimens is increased with a decrease in the applied constant load at 800 $^{\circ}$C for both shear and tensile loading modes. The creep strength at 1000 h under shear loading is about one quarter of the shear strength at 800 $^{\circ}$C. The tensile creep strength at 1000 h is about 9% of the tensile strength at 800 $^{\circ}$C. Failure patterns of both shear and tensile joint specimens are similar regardless of the creep rupture time. Cracks initiate at the interface between the spinel layer and chromate ($BaCrO_4$) layer, penetrate through the $BaCrO_4$ layer, and propagate along the interface between the chromate layer and glass-ceramic substrate until final fracture. Final, fast fracture occasionally takes place within the glass-ceramic layer. In addition, a micro-indentation technique was also applied to evaluate the fracture toughness for each layer of the SOFC cell.

# INTRODUCTION

## 1.1  Solid Oxide Fuel Cell

A solid oxide fuel cell (SOFC) is a device for conversion of chemical energy into electricity by means of electrochemical reactions of a fuel and an oxidant across an ion conducting electrolyte [1].   There are two gas flows in an SOFC stack, fuel and air.   Hydrogen as the fuel flows into the anode side of the cell for an oxidation reaction.   Oxidant is fed to the cathode that accepts electrons from the external circuit and undergoes a reduction reaction. The operating temperature of SOFCs is about 600-1000 $^{o}$C which is higher than other fuel cells because solid oxides possess highly ionic conductivity at elevated temperature.   There are two typical configuration designs of SOFC, tubular and planar cells.   Planar SOFCs attract more attention than tubular ones because they are cost effective and have a lower ohmic lose [2].   The latter advantage leads to a superior performance and a much higher power density.

Figure 1 shows the structural scheme of a planar SOFC stack [3].   A unit cell which is all made of ceramic can produce electricity by electrochemical reactions.   It consists of a fully dense electrolyte layer capable of conducting oxygen ions, and a porous anode and cathode of electrically conducting capability.   An integrated cathode-electrolyte-anode cell for planar SOFCs is referred to as a positive electrode-electrolyte-negative electrode (PEN) plate [4].   A porous nickel mesh as a current connector and fuel gas manifold is placed between the anode and interconnect.   Because of the difference in coefficient of thermal expansion (CTE) for each component in SOFC, thermal stresses are expected to be generated during operation of an SOFC.   The flexibility of the porous nickel mesh can reduce the thermal stress.   An important component of planar SOFCs is the interconnect which connects the PENs in an electrical series.   The interconnect must be chemically and mechanically stable for long-term operation at high temperatures.   In order to prevent leakage of fuel and air, gas tight seals which are called sealant in SOFC must be applied along the edges of connecting components [5]. Sealants can maintain the electrical performance of SOFC by avoiding a mixing of fuel and air.   Therefore one of the key issues in development of planar SOFCs is the technique of sealing adjacent components to obtain gas tightness.

## 1.2  Glass Sealant

As mentioned before, the sealant in SOFCs must be chemically stable and compatible with other components to minimize thermal stress during operation. Two approaches of sealing, rigid and compressive seals, are being developed for SOFCs [6]. The compressive seals use mica-based materials and need externally applied forces to compress the fuel cell stack for tight sealing. There are still some problems with through-seal leakage, interface reactions, etc. for compressive seals [7]. For compressive seals, matching of CTE is not so important as that in the rigid sealing. Another approach of sealing is rigid seals that have been shown no significant degradation for operation time more than 1000 h [7]. Rigid seals need no externally applied compressive forces but their CTEs should closely match with those of the neighboring components like electrode and interconnect. Many glasses and glass-ceramics developed for rigid seals in SOFCs contain alkali metals. The alkali metals can react with other SOFC components and enhance the volatility of chromium, which can lead to poisoning of the cell [6]. Instead of alkali metals, alkaline-earth-metal-based glasses are commonly used for SOFC applications as they can sustain the severe operation conditions of SOFCs [5].

A rigid sealant must offer sufficient viscosity and good wetting behavior to form well adherent bond during joining process and operation stage. The important criterion for selection of a suitable glass sealant is the glass transition temperature ($T_g$) [6]. A suitable seal should have a sufficient ability to flow and maintain enough rigidity for mechanical integrity decided by $T_g$. Glass-ceramics are a composite which consists of amorphous and crystallization phases. During the SOFC operation, some glass phases may transform into glass-ceramics due to formation of crystalline phases that could increase the strength and change the CTE. The mismatch of CTE between these two phases may cause cracks, microvoids or fracture by thermal stress. Crystallization of a glass is sometimes dependent on its composition and thermal events so that it is important to have suitable viscosity and wetting behavior during bonding process and to have sufficient integrity during operation. Therefore, crystallization of glass sealants is an important factor related to thermal stress distribution which may generate some defects during operation.

In the case of barium-containing glass-ceramics for SOFCs, the CTE is increased by the crystallization due to formation of barium silicate ($BaSiO_3$) [6]. Crystallization of a barium-containing glass is faster than that of one containing other alkaline-earth metal elements due to a lower activation energy of barium [6]. Barium is used as a network modifier in the glass. There is a proof that BaO/SrO can reduce $T_g$ and glass crystallization temperature ($T_c$) along with raising the CTE [5]. Other elements offer different functions. For example, $La_2O_3$ is a viscosity modifier and long-term CTE stabilizer, while $B_2O_3$ is a low temperature glass former and a

wetting agent.

A new glass-ceramic sealant (designated as GC-9) containing BaO, $B_2O_3$, $Al_2O_3$, and $SiO_2$ for intermediate-temperature of planar SOFC (IT-pSOFC) at 700 $^o$C-750 $^o$C has been developed at the Institute of Nuclear Energy Research (INER). The properties of CTE, viscosity, crystallization, and chemical interaction between this sealant and other planar SOFC components (electrolyte, electrode, interconnect, and frame) have been investigated [8-10]. The GC-9 glass-ceramic shows good thermal properties and chemical compatibility with other planar SOFC components according to these reports [8-10]. Mechanical properties of the GC-9 glass-ceramic sealant have been investigated at various temperatures by Chang [11]. In that study [11], GC-9 samples were sintered at 850 $^o$C and aged at 750 $^o$C for 4 and 100 h, designated as non-aged and aged, sintered GC-9 glass-ceramic, respectively, for generating different degrees of crystallization. Results showed that the extent of crystallization was increased with a longer aging time up to 100 h, but the types of crystalline phases were not changed [11]. Both types of GC-9 glass-ceramic had a significant strength enhancement with temperature due to a crack healing effect at temperature below $T_g$, as compared to the room-temperature strength [11]. At temperature above $T_g$, the flexural strength and Young's modulus of both aged and non-aged GC-9 glass-ceramics were decreased. A greater flexural strength and stiffness of the aged, sintered GC-9 glass-ceramic than the non-aged one was found at temperature higher than 700 $^o$C due to a greater extent of crystallization [11]. Although, the sintered GC-9 glass-ceramic had a greater flexural strength and stiffness with a longer aging time, the ability for relaxing thermal stresses at high temperature may be decreased due to a less amount of residual glass [11].

A research of Yeh [12] further studied the mechanical properties of 1000 h-aged, sintered GC-9 glass-ceramic in comparison with those in the study of Chang [11]. Figure 2 shows the XRD patterns of the non-aged, 100 h-aged, and 1000 h-aged GC-9. There are several phase peaks indicating existence of certain crystalline phases in those materials. The main phase peaks in the XRD patterns of the non-aged and 100 h-aged GC-9 glass-ceramic correspond to structures of $BaSiO_3$, alpha-$Ba(Al_2Si_2O_8)$, and $Ba_3La_6(SiO_4)_6$. On the other hand, crystallization also took place in the 1000 h-aged GC-9 glass-ceramic and the dominant crystalline phases are $Ca(Al_2Si_2O_8)$ and alpha-$Ba(Al_2Si_2O_8)$. A longer aging time of 1000 h generated additional crystalline phases ($Ca(Al_2Si_2O_8)$ and $Al_2SiO_5$) in the sintered GC-9 glass-ceramic [12]. Because of a greater extent of crystallization, an improvement of flexural strength and stiffness of the aged GC-9 glass-ceramic over the non-aged one was observed at temperature higher than 700 $^o$C [12].

## 1.3   Joint of Glass-Ceramic Sealant, Metallic Interconnect, and Cell

Both ceramic and metallic materials have been used as interconnects for SOFCs.   Ceramic interconnects are made of semiconducting oxides which have good stability in air and are generally compatible with other ceramic components [7].   The electrical conductivity of ceramic interconnects increases with temperature, which is suitable for the high-temperature SOFCs.   As for metallic interconnects, they are excellent electrical conductors but the oxidation resistance is a challenge for them.   When the oxide scales are formed, the electrical conductivity would degrade [7].   However, metallic interconnects are favored for IT-SOFC over the expensive ceramic interconnects due to their low cost and easy fabrication [7].

Interconnects separate the fuel at the anode side from the air or oxidant at the cathode side by sealants.   At the same time, they act as bipolar plates which electrically connect PENs in series in the stack.   In order to maintain good performance of an SOFC stack, interconnects must be hermetically sealed to adjacent SOFC components such as PEN supporting frames.   Figure 3 [13] shows the locations where seals are used in a planar SOFC stack with metallic internal gas manifolds and metallic interconnects.   Common seals include: (a) cell to metal frame; (b) metal frame to metal interconnect; (c) frame/interconnect pair to electrically insulating spacer; (d) stack to base manifold plate [13].   For type (a) seal, the edges of a cell are bonded with a metal frame which is usually made of the same material of the interconnect.   Seals (b) and (d) can be referred to as a joint of glass-ceramic sealant and metallic interconnect.

During cyclic operation of an SOFC, generation of thermal stresses is inevitable leading the seals to be subjected to tensile and shear stresses [14-16].   If the stresses exceed the corresponding strength of the joint, a degradation of cell performance will result from failure of the seal.   Therefore, it is necessary to investigate the mechanical properties of the joint of glass-ceramic sealant and metallic interconnect for assessment of structural reliability of an SOFC stack.   Any interaction between glass-ceramic and metal may influence mechanical properties of the joint.   Moreover, the interactions of glass sealants with different components of planar SOFCs can also produce different crystalline phases due to internal diffusion of anions and cations.   Unfortunately, those interactions such as undesirable chromate formation [17] and electrical short-circuiting [18] are difficult to avoid if ferritic chromia-forming alloys are applied as interconnect.

The joint strength between glass-ceramic sealants and metallic interconnects in SOFCs have been characterized using various testing techniques.   A modified rupture testing technique was developed by placing a sealed disk specimen in a test fixture and pressurizing the backside of the

sample until rupture of seal [19]. An anode-supported bilayer made of nickel oxide-5 mol% yttria stabilized zirconia and 5 mol% yttria stabilized zirconia (NiO-5YSZ/5YSZ) and eight different ferritic stainless steels, five of which had a chromia scale and three of which had an alumina scale, were sealed using a G-18 paste to make sealed disk specimens. In addition to testing as-joined specimens, aging tests were conducted by exposing the sealed disk specimens to ambient air at 750 $^o$C for various hold times. Cyclic thermal testing was performed between room temperature and 750 $^o$C for a number of cycles. The results showed that in both the as-joined and exposure tested conditions, alumina-forming ferritic steel substrates offered greater bond strength with G-18 [19]. The composition and thickness of the reaction zone between the metal's oxide scale and G-18 glass were the dominant factors in determining the joint strength [19]. The barium chromate layer that developed on the chromia-forming steels exhibited poorer thermal expansion match and tended to grow to a greater thickness than the celsian zone observed on the alumina-formers [19].

The tensile joint strength between a glass-ceramic ($SiO_2$-$Al_2O_3$-CaO-$Na_2O$, SACN) and a metallic interconnect (Crofer 22 APU) at room temperature was characterized by Smeacetto et al. [20]. It was observed that fracture always occurred in the glass-ceramic and never at the interface of the joint [20]. Another study by Stephens et al. [21] investigated the interfacial strength between the G18 glass-ceramic and Crofer 22 APU substrate at temperatures ranging from 25 $^o$C to 800 $^o$C under both tensile and shear loading. However, two different failure modes were observed in the tensile tests, glass bulk failure mode referring to failure occurring through the glass layer, and interfacial failure mode referring to failure occurring at the glass-metal interface [21]. In the study of Malzbender et al. [22], the shear strength of the joint between a glass-ceramic sealant (BaO-CaO-$Al_2O_3$-$SiO_2$, BCAS) and a Crofer 22 APU interconnect at the SOFC operating temperature was characterized by a symmetric shear test. In addition to shear strength, shear modulus and viscosity of the joint were also determined by a rheological model [22]. At the SOFC operating temperature, the as-joined specimens exhibited viscous shear deformation while the viscous shear deformation became more difficult for additionally crystallized specimens [22].

The tensile joint strength of a novel high-temperature sealing glass (SrO-CaO-$Y_2O_3$-$B_2O_3$-$SiO_2$) with a metallic interconnect (Crofer 22 APU) at room temperature was investigated by Chou et al. [17]. The bonding/wetting behavior of glasses to metals is dependent on the nature of the surface of the metal. In order to simulate long-term exposure conditions, the samples were pre-oxidized to generate oxide layers. Effects of environmental aging, including oxidizing and reducing, were also studied. The effect of aluminization of the metallic interconnect on the tensile strength

of the joint at room temperature was further studied by Chou et al. [23]. Three different processes for aluminization were evaluated. The results of that study [23] showed that aluminization could reduce undesirable chromate formation between the alkaline earth silicate glass and chromia-forming alloys.

The joint strength of interconnect/sealant/cell is another important factor in maintaining the electrical performance of planar SOFCs and the effectiveness of sealants under typical operating conditions. The effectiveness of a recently developed sealant has been investigated for the electrical performance of an anode-supported cell under typical SOFC operating conditions [24]. In that study, the variation of open circuit voltage with time for joined Crofer 22 APU/glass-ceramic sealant/anode-supported cell in dual atmospheres was measured. It showed that a $SiO_2$-$CaO$-$Al_2O_3$-$Na_2O$ based sealant provided an effective gas stream separation between the anode and cathode side, as indicated by a very high open circuit potential (1075 mV, close to the theoretical one) [24]. The absence of cracks near the interfaces of the glass-ceramic with Crofer 22 APU and cell demonstrated its good thermo-mechanical compatibility with both substrates [24]. However, a small number of closed pores was observed [24]. This should not be a problem because the sealants didn't make gases permeable.

## 1.4 Creep

As mentioned before, sealants are used to bond components of planar SOFCs. Sealants must be able to withstand the thermal cycling of SOFC operation. They need to have long-term durability due to their difficulty to repair in SOFCs. A seal should not display significant creep deformation at high temperatures to maintain the geometric stability of an SOFC stack. By understanding the creep properties, the life of a seal may be predicted in terms of creep deformation [25]. Creep is normally regarded as deformation at a constant stress/load as a function of time and temperature [26]. Creep deformation can not be neglected for metals and crystalline ceramics at a high temperature in the range of 30 to 60% of the melting temperature ($T_m$) [27]. Figure 4 [27] shows strain versus time during creep under constant load. There is an initial instantaneous response of elastic and perhaps plastic strain, then followed by a gradual accumulation of creep strain, as shown in Fig. 4 [27]. In the primary stage, the strain rate is relatively high. However, strain rate decreases and becomes constant when the primary stage is ended. The second stage is called steady-state creep. At the end of the secondary stage, strain rate increases in an unstable manner as rupture failure approaches [27]. Creep cavities may form inside the material and cause rupture in the

tertiary stage.

The mechanical properties of glass-ceramics vary with degree of crystallinity. Nanoindentation was applied to measure the elastic modulus, hardness, and creep properties of a G18 sealant glass from room temperature to 400 $^{\circ}$C [25]. The maximum load was held constant for 60 s before unloading in order to obtain creep properties. G18 samples were sintered at 850 $^{\circ}$C, and aged at 750 $^{\circ}$C for 5, 50, and 100 h to possess different extents of crystallization. The results showed that elastic modulus slightly increased with temperature below 300 $^{\circ}$C. There was a significant jump of about 100% in elastic modulus from 300 $^{\circ}$C to 400 $^{\circ}$C in all the variously crystallized specimens due to self-healing of cracks [25]. The samples with a longer aging time didn't show a significant increase in deformation before it reached the secondary stage. It indicated that specimens having a higher degree of crystallinity were more resistant to creep at high temperature. At secondary state, there was no clear dependence of creep strain rate on aging time at a given testing temperature because the tests were performed below $T_g$ (620 $^{\circ}$C for G18). Under this condition, there was no phase change and viscoelasticity provided by glassy phase [25]. However, an increase in steady-state strain rate with temperature was found for each aging condition.

A research further studied the nanoindentation creep behavior of G18 at 25 $^{\circ}$C, 550 $^{\circ}$C, 650 $^{\circ}$C, and 750 $^{\circ}$C using samples of different extents of crystallization [28]. One set of samples was sintered at 850 $^{\circ}$C for 1 h, and aged at 750 $^{\circ}$C for 4 h. Another set of samples was aged further for 100 h at 800 $^{\circ}$C. Creep deformation variation was taken for 120 s, when held at maximum load. The results showed that the 4 h-aged sample had a greater elastic modulus than did the 100 h-aged one at room temperature. Further aged samples contained micro-voids in glass phases which surrounded the crystalline phase. These micro-voids which might cause cracking during cooling resulted in a lower elastic modulus for a 100 h-aged sample. Above 500 $^{\circ}$C, the 100 h-aged sample had a greater elastic modulus, compared to the 4 h-aged one, due to a self-healing effect of cracks. The results also showed that creep deformation increased with temperature, especially above $T_g$. The 4 h-aged G18 which had less crystalline phases displayed more creep deformation than did the 100 h-aged one. The crystalline phases with a higher $T_g$ were most likely to impede flow of the glassy phases [28].

## 1.5  Purposes and Scope

The leading candidates for planar SOFC sealants are glasses and glass-ceramics. It is difficult to repair sealants when they fail or fracture because they are bonded to several components, such as interconnects and PENs. The high-temperature operation of SOFC gives rise to significant

thermal stresses due to CTE mismatch and temperature gradients. Some pre-existent pores or defects in a ceramic component subjected to a prolonged thermal stress can grow to failure and degrade the performance of an SOFC system. Therefore, it is necessary to study the high-temperature creep properties of the glass/glass-ceramic sealant to assess the structural integrity of a planar SOFC stack during cyclic operation. It is also needed to study the creep behavior of joints between the glass-ceramic sealant and interconnect at high temperature. During long-term steady operation with thermal stresses, creep may generate larger deformation or rupture at the joints in a stack. The PENs in an SOFC stack are also made of ceramics and the existing pores may grow to become cracks by thermal stresses [29]. Cracks may initiate at the interface of the joint of PENs and glass-ceramic sealants and/or penetrate through the glass-ceramic sealants. It is thus interesting to study the cracking path in the joint of PEN/glass-ceramic sealant/interconnect of an SOFC stack.

There are three parts in the present study. Firstly, creep properties at high temperature are investigated for a newly developed GC-9 glass-ceramic sealant in variously aged conditions. Creep deformation and rupture time were measured by conducting ring-on-ring tests at 800 $^{\circ}$C at different constant loadings. The glass sealant applied to a planar SOFC stack may crystallize during operation at high temperature such that the effect of crystallization on creep properties of GC-9 is characterized. Secondly, creep properties of the joint between the GC-9 glass-ceramic sealant and an interconnect steel are also investigated. Two loading modes, tensile and shear loading, were applied to characterize the creep properties of the joints at 800 $^{\circ}$C. Microstructural and fractography analyses were conducted with scanning electron microscopy (SEM) to correlate with the creep testing results. Thirdly, testing techniques to characterize the high-temperature fracture energy of a joint made of PEN, glass-ceramic sealant, and metallic interconnect are developed. The third part is not finished completely at present such that only the preliminary results and relevant discussion are presented. It is hoped that results of the current study can provide some useful information for assessing the long-term structural reliability of planar SOFC.

# 2. MATERIALS AND EXPERIMENTAL PROCEDURES

## 2.1  Creep Test of GC-9 Glass-Ceramic

### 2.1.1    Materials and specimen preparation

The GC-9 glass sealant used in the present work was developed at INER for IT-pSOFC.  The major chemical composition of the GC-9 glass sealant includes 0-40 mol% BaO, 0-40 mol% $SiO_2$, 0-15 mol% $B_2O_3$, 0-15 mol% CaO, 0-15 mol% $La_2O_3$, 0-10 mol% $Al_2O_3$, and 0-5 mol% $ZrO_2$.  It was made by mixing the constituent oxide powders followed by melting at 1550 $^o$C for 10 h.  After melting, it was poured into a mold preheated to 680 $^o$C to produce GC-9 glass ingots.  The GC-9 glass ingots were then annealed at 680 $^o$C for 8 h and cooled down to room temperature.

GC-9 glass powders were made by crushing the as-cast glass ingots and sieving with 325 mesh sieves.  The average size of the glass powder is 45 μm.  Slurries were made by adding into the GC-9 powders the desired amounts of solvent (alcohol), binder (ethyl celluloid), and plasticizer (polyethylene glycol).  The slurries were dried at 80 $^o$C for 1 h and the mixture was ground into powders again after well mixing.  The GC-9 glass powders were then put into a mold and pressed to form a circular disk with a diameter of 35 mm and thickness of 1.5 mm for ring-on-ring test. Heat-treatment of the circular disk-shape specimens included the following steps: heated from room temperature to 550 $^o$C at 5 $^o$C/min, held at 550 $^o$C for 1 h, heated up to 850 $^o$C at 5 $^o$C/min, sintered at 850 $^o$C for 4 h, cooled down to 750 $^o$C at 5 $^o$C/min, held at 750 $^o$C for 4 h, and cooled down to room temperature.  Specimens through such heat-treatments are designated as non-aged GC-9 glass-ceramic.  In order to understand the effects of crystallization under a longer aging time on the creep properties of the sintered GC-9 glass-ceramic, some specimens were also prepared by the same heat-treatment profile, except the holding time at 750 $^o$C.  These specimens were held at 750 $^o$C for 100 h or 1000 h instead of 4 h.  They are designated as 100 h-aged and 1000 h-aged GC-9 glass-ceramic, respectively.  All of the specimens were polished with an 80-grit SiC paper to reduce surface roughness before creep testing.

### 2.1.2    Ring-on-ring creep test

Biaxial flexural test is a suitable method for determining the strength of plate-like materials because edge effects can be minimized.  In the current

work, a biaxial flexural ring-on-ring test of ASTM Standard C1499 [30] was applied to determine the creep properties of the non-aged, 100 h-aged, and 1000 h-aged GC-9 specimens at 800 $^{\circ}$C.   Short-term ring-on-ring creep tests were performed using a commercial closed-loop servo-hydraulic material test machine attached with a furnace.  Long-term creep tests (> 100 h) were conducted using a direct-load creep test machine. The flexural loading fixture with a 10-mm-diameter inner loading ring and a 20-mm-diameter outer supporting ring was made of a nickel-based superalloy.   Figure 5 shows the schematic of the ring-on-ring test fixture.   Creep tests of variously aged GC-9 glass-ceramic were conducted under constant loading at 800 $^{\circ}$C.   Each specimen was heated to 800 $^{\circ}$C at a heating rate of 6 $^{\circ}$C/min and then held at 800 $^{\circ}$C for 3 min before applying the load.   Several constant loadings were applied for each aged condition to obtain the stress-rupture time relationship. For each applied constant load, 4-5 specimens were used for repeated creep tests.   After creep tests, fracture surfaces of the broken specimens were observed with SEM to identify the fracture origins and mechanisms.

According to ASTM Standard C1499 [30], the formula for calculating the biaxial flexural stress, σ, of a circular plate is given as

$$\sigma = \frac{3P}{2\pi h^2}\left[(1-v)\frac{D_S{}^2 - D_L{}^2}{2D^2} + (1+v)\ln\frac{D_S}{D_L}\right] \tag{1}$$

where $P$ is the applied force, $h$ is the thickness of specimen, and $D_L$, $D_S$, and $D$ are the diameters of the load ring, support ring, and specimen, respectively. In the present study, the Poisson's ratio $v$ in Eq. (1) was assumed equal to 0.3. The deflection contour in the thickness direction from center to edge of the specimen was derived in a previous study [31] and is given as

$$\delta = \frac{3P(1-v^2)R_L^2}{2\pi h^3 E}\left\{\left(\frac{R_S}{R_L}\right)^2 - 1 - \left[\left(\frac{R}{R_L}\right)^2 + 1\right]\ln\left(\frac{R_S}{R_L}\right) + \frac{1}{2}\frac{1-v}{1+v}\frac{R_S^2 - R_L^2}{R_{SP}^2}\frac{R_S^2 - R^2}{R_L^2}\right\}$$
$$\text{for } 0 \le R \le R_L \tag{2}$$

where $\delta$ is the deflection of the specimen, $E$ is the Young's modulus of the specimen, $R$ is the radial distance from the disk center to specified point, and $R_L$, $R_S$, and $R_{SP}$ are the radii of the load ring, support ring, and specimen, respectively.   In the present study, the displacement of the actuator was measured and is regarded as the deflection of the specimen at the contact point with the inner loading ring ($R = R_L$).   Rearrangement of Eq. (2) gives

$$E = \frac{3P(1-v^2)R_L^2}{2\pi h^3 \delta}\left\{\left(\frac{R_S}{R_L}\right)^2 - 1 - \left[\left(\frac{R}{R_L}\right)^2 + 1\right]\ln\left(\frac{R_S}{R_L}\right) + \frac{1}{2}\frac{1-v}{1+v}\frac{R_S^2 - R_L^2}{R_{SP}^2}\frac{R_S^2 - R^2}{R_L^2}\right\} \tag{3}$$

The Young's modulus of the GC-9 glass-ceramic can be obtained by substituting the applied load ($P$), actuator displacement ($\delta$), and inner loading ring radius ($R = R_L$) into Eq. (3). The biaxial strain in a plane stress condition can be determined as follows,

$$\varepsilon = (1-\nu)\frac{\sigma}{E} \tag{4}$$

Substitution of Eqs. (1)-(3) with $R = R_L$ into Eq. (4) yields

$$\varepsilon = \frac{(1-\nu)h\delta}{R_L^{\,2}}\left\{\frac{(1-\nu)\dfrac{R_S^{\,2}-R_L^{\,2}}{R_{SP}^{\,2}}+(1+\nu)\ln\dfrac{R_S}{R_L}}{\left(\dfrac{R_S}{R_L}\right)^2 -1-2\ln\left(\dfrac{R_S}{R_L}\right)+\dfrac{1}{2}\dfrac{1-\nu}{1+\nu}\dfrac{R_S^2-R_L^2}{R_{SP}^2}\dfrac{R_S^2-R_L^{\,2}}{R_L^2}}\right\} \tag{5}$$

During a creep test, the actuator displacement $\delta$ will vary with time. Accordingly, the strain-time relationship in a ring-on-ring creep test can be obtained through Eq. (5).

## 2.2 Creep Test of Joint of Glass-Ceramic Sealant and Metallic Interconnect

### 2.2.1 Materials and specimen preparation

As mentioned in Section 1.3, glass-ceramic sealants are applied as a rigid sealing to bond each layer together and prevent leakage of air and fuel in a planar SOFC stack. Among the four sealing locations shown in Fig. 3, sealings of a metallic frame to a metallic interconnect (S2) and a stack to a base manifold plate (S4) are classified as a joint of glass-ceramic sealant and metallic interconnect. In order to simulate the conditions of a joint subjected to thermal stresses at operating temperature, two types of sandwich-like specimens (metal/sealant/metal) were designed in this study for determining the creep properties of the joint and investigating the interfacial reactions.

The metallic parts of the joint specimens were made of a commercial ferritic stainless steel, Crofer 22 H (ThyssenKrupp VDM GmbH, Werdohl, Germany), which is a heat-resistant alloy developed for application in SOFCs. Chemical compositions and mechanical properties of the Crofer 22 H alloy are listed in Tables 1 and 2 [32], respectively. The aforementioned GC-9 glass-ceramic was used to join two metal slices to make a sandwich specimen. Table 3 [12] lists the Weibull characteristic strength and Weibull modulus of the sintered GC-9 glass at various temperatures.

Figure 6 shows the scheme of two types of joint specimens for tensile test (Fig. 6(a)) and shear test (Fig. 6(b)), respectively. Dimensions of each rectangular steel slice are 95 mm x 25 mm with a thickness of 2.5 mm. A pin hole was drilled in each steel slice for applying pin loading. It is effective to minimize bending and twisting effects during a creep test by means of pin loading. For shear specimens, one edge of each steel slice with an area of 8 mm x 25 mm was milled from the original thickness of 2.5 mm to 1 mm. After machining, a GC-9 glass slurry was spread on the joining region of each steel slice to make a half-specimen. The apparent joining areas are 25 mm x 2.5 mm and 25 mm x 6 mm for tensile and shear specimens, respectively. The glass slurry was made of a mixture of GC-9 glass powders dispersed in ethanol. The half-specimen was then put in a furnace to dry the slurry at 80 $^o$C. A joint specimen was assembled by placing a half-specimen onto another one to form a steel/glass-ceramic sealant/steel sandwich specimen through appropriate heat treatments. In the assembling process, the joint specimens were firstly held at 500 $^o$C for 1 h and heated to 900 $^o$C followed by a hold time of 4 h. The heating rate at each heating step in the given assembling process is 5 $^o$C/min.

## 2.2.2    Creep test

Tensile and shear creep tests were conducted at 800 $^o$C under a constant load using a direct-load creep test machine. Four loadings were selected for each type of creep test based on the strength data of Chen [33]. About 5 specimens were repeatedly tested at each given constant loading.

## 2.2.3    Microstructural analysis

After creep testing, fracture surface of each specimen was examined with an optical microscope to determine the true joining area. In order to investigate the characteristics of interfaces in the joint, some samples were cut along the longitudinal direction to observe the cross section of the joint. The cross sections were finely polished to optical finish. SEM was also employed to examine the interfacial morphology between the glass-ceramic sealant and metallic interconnect. An energy dispersive spectrometer (EDS) module was used for composition analysis in order to determine various elemental distributions in the glass-ceramic sealant and metallic interconnect. The creep fracture modes of the joint under tensile stress and shear stress were also characterized.

## 2.3 Fracture Toughness Test of PEN

### 2.3.1 Materials and specimen preparation

Vickers indentation fracture test has been an experimental technique for estimate of the fracture resistance of brittle ceramics [35]. It requires only a small piece of specimen and the measurements can be quickly completed with a low cost. This technique was also applied in the current study to determine the fracture toughness of the anode, cathode, and electrolyte in a PEN (full cell) and a half cell plate. Both sides of the full cell and half cell were indented to determine the fracture toughness. For a sandwich-type full cell, the two sides are anode and cathode with an electrolyte layer in between. For a half cell, there are only two layers, anode and electrolyte. The indentation sides are polished by 0.3 μm $Al_2O_3$ powders to minimize the effect of surface defect.

### 2.3.2 Vickers indentation fracture toughness of PEN

A Vickers pyramidal microhardness indenter was employed to press on the surface of the given specimens (a full cell and an half cell). The Vickers indentation tests were conducted with an applied load of 9.8 N. All indentation tests were performed with a constant indenter dwell time of 10 s. Ten independent indentation tests at various locations were conducted for each material condition in the current work. The Vickers indenter creates a square impression in which two surface-projected diagonals are measured with an optical microscope [36]. The Vickers hardness is computed as follows,

$$H_v = 1.8544(\frac{P}{d^2}) \tag{6}$$

where $H_v$ is the hardness in unit of GPa, $P$ is the applied load in unit of N, and $d$ is the average length of the two diagonals of the indentation in unit of mm.

The deformed region by indentation leads to generation of four cracks emanating from the corners of the Vickers diamond impression. The lengths of the cracks, the applied load, the impression size, the hardness and elastic modulus of the material, and an empirical calibration constant are used to compute the fracture toughness of the material [35]. There are two types of cracks formed by indentation, median/radial (R-type) and Palmqvist (P-type), as shown in Fig. 7 [37]. A R-type crack is formed under a large load. The equation of fracture toughness for R-type cracking is given as [38],

R-type: $\quad K_{IC} = 0.018 \dfrac{P}{C_o^{\frac{3}{2}}}(\dfrac{E}{H_v})^{\frac{1}{2}}$ $\hspace{4cm}$ (7)

where $P$ is the applied load in unit of N, $C_o$ is the length from the center of the impression to the crack tip in unit of m, $E$ is the Young's modulus in unit of GPa, and $H_v$ is the hardness in unit of GPa. The equation of fracture toughness for P-type cracking is in the following [34],

P-type: $\quad K_{IC} = 0.035(\dfrac{H_v}{E})^{-\frac{2}{5}}(\dfrac{I_0}{a_d})^{-\frac{1}{2}}(H_v a_d^{\frac{1}{2}} \phi^{-\frac{3}{5}})$ $\hspace{2cm}$ (8)

where $I_o$ is the crack length of Palmqvist from the corner of the impression to the crack tip in unit of m, $a_d$ is the half length of the average of two diagonals of the indentation in unit of m, and $\phi$ is a geometrical constant.

## 3.  RESULTS AND DISCUSSION

## 3.1   Creep Properties of Variously Aged GC-9 Glass-Ceramic

### 3.1.1  Microstructure

Microstructure of variously aged GC-9 glass-ceramic is shown in Figs. 8-10 [11-12].   Needle-shape crystals which are the primary crystalline phase, alpha-Ba($Al_2Si_2O_8$), are observed in the given three conditions.   The aggregated particles are difficult to identify their phases because they are buried in the residual glassy phase.   Microvoids are found in variously aged GC-9 resulting from burning of the binder or plasticizer during sintering process.   For the non-aged GC-9, it shows a fewer amount of crystalline phases in Fig. 8 [11].   The amount and size of crystalline phases in a further aged GC-9 are greater than those in the non-aged GC-9, as shown in Fig. 9(c) and 9(c) [12].   The crystalline phases of variously aged GC-9 have already been discussed in Section 1.2.   The main phases in the non-aged and 100 h-aged GC-9 are $BaSiO_3$, alpha-Ba($Al_2Si_2O_8$), and $Ba_3La_6(SiO_4)_6$.   For the 1000 h-aged GC-9, the dominant crystalline phases are $Ca(Al_2Si_2O_8)$ and alpha-Ba($Al_2Si_2O_8$) in addition to $Al_2SiO_5$ due to a longer aging time.

A longer aging heat-treatment changes the volume fraction of the crystalline phases in a glass-ceramic microstructure.   The crystalline phases can be determined by the peaks in the XRD analysis results, as shown in Fig. 2.   The entire area below the XRD curve, including crystalline and amorphous phases, can be integrated using a commercial Jade 5 (EasyQuant, New York, NY) software [19].   For each crystalline phase, the area below the corresponding peaks means the diffracting integrated intensity.   The volume fraction of the crystalline phases can be determined as follows,

$$X_c = \frac{\sum I_c}{\sum I_c + \sum I_a} \times 100\% \tag{9}$$

where $X_c$ is the percent crystallinity, $\Sigma I_c$ is the diffracting integrated intensities of the crystalline phases, and $\Sigma I_a$ is the scattering integrated intensities of the amorphous phases.   The crystallinity for variously aged GC-9 can be estimated by calculating the relevant areas in the XRD patterns. The crystallinity for the non-aged, 100 h-aged, and 1000 h-aged GC-9 is thus determined as 40%, 42%, and 49%, respectively.   The crystallinity increases with aging time.   The crystalline phases apparently have been formed during the sintering process in the given three conditions.   In the further aging

process, the size of the crystalline phase increases, as shown in Figs. 8-10.

## 3.1.2  Creep deformation

Figure 11 shows the typical creep strain curves for the non-aged, 100 h-aged, and 1000 h-aged GC-9 tested at 800 $^{\circ}$C.  As shown in Fig. 11, a larger loading causes a shorter creep rupture time.  For the non-aged GC-9, the applied constant loads include 70 N, 60 N, 50 N, 40 N, and 30 N.  The apparent biaxial flexural stresses applied on the specimens can be calculated by Eq. (1).  The corresponding applied stresses are 13 MPa, 11 MPa, 10 MPa, 8 MPa, and 6 MPa.  For a given load of 70 N and 60 N, the creep rupture time is less than 1 h and no secondary-stage creep is observed, as shown in Fig. 11(a).  When the applied constant load is equal to 30 N (6 MPa), it shows a large scattering in the creep rupture time.  Some specimens failed at a time less than 30 h, while others last longer than 1000 h.  The strain rate decreases initially and becomes constant after the primary stage in the 30-N (6-MPa) curve presented in Fig. 11(a).  Under a high stress, the secondary stage may be replaced by an inflection point followed by the tertiary stage.  In contrast, the tertiary stage disappears in some low-stress cases.  For example, the 30-N creep curve (Fig. 11(a)) shows a long-term secondary stage without a tertiary stage.  A greater flexural strength and stiffness of the aged GC-9 over the non-aged one is observed at 800 $^{\circ}$C due to a greater extent of crystallization [12].  Therefore, the applied constant loads are slightly increased for the aged GC-9 to reach a certain rupture time.  As shown in Fig. 11(b), for a given constant load of 60 N (11 MPa) and above, the creep rupture time of the 100-h aged GC-9 is less than 10 h with no noticeable secondary stage of creep deformation.  Secondary-stage creep deformation is observed for an applied constant load of 55 N (10 MPa) and below, and the creep rupture time is in the range of hundreds to thousands of hours, as shown in Fig. 11(b).  For an applied constant load of 50 N (9 MPa), the specimen exhibits a long-term secondary creep and runs out without fracture at more than 1000 h (Fig. 11(b)).

For the 1000 h-aged GC-9, a preliminary comparison is shown in Fig. 11(c) due to a limited number of data available at the present time.  As the 1000 h-aged GC-9 contains a greater amount of crystalline phases, it exhibits a greater strength and creep resistance as compared to the non-aged and 100 h-aged ones.  For example, given a load of 70 N (15 MPa), the 1000 h-aged GC-9 can last longer than 1000 h which is much longer than those of the non-aged and 100 h-aged ones.  Figure 12 shows a comparison of creep strain curves of variously aged GC-9 under a constant loading of 70 N in the first 10 h.  Rupture of the non-aged and 100 h-aged GC-9 occurred at less than 1 h and 8 h, respectively.  For the 1000 h-aged GC-9, it shows a

long-term secondary creep and didn't fail when the test time exceeded 1000 h. A rapid, large deformation in the non-aged GC-9 is caused by a greater amount of amorphous phase. The creep strains don't have a drastic increase for the aged ones before they reach the secondary stage. In the secondary stage of creep deformation, the curve of the 1000 h-aged GC-9 shows a slope smaller than that of the 100 h-aged one. Therefore, GC-9 with a higher extent of crystallinity is more resistant to creep at 800 $^o$C.

The analysis of creep results is usually related to the secondary stage. It avoids the problems in defining equations that quantify creep-curve shapes [39]. Although some limitations arise when the primary or tertiary stage becomes nonnegligible, the Norton relationship is most often used for ceramics [39]. The Norton's power law [27] which is used to correlate the minimum strain rate with applied stress at a given temperature is given as below,

$$\dot{\varepsilon}_{min} = f(T)\sigma^n \tag{10}$$

where $\dot{\varepsilon}_{min}$ is the minimum creep strain rate, $f(T)$ is a temperature-dependent function, $\sigma$ is the applied stress, and $n$ is the stress exponent. The stress exponent ($n$) plays an important role and depends on the creep deformation mechanisms acting during a creep test. A value of $n$ in the range of 3-8 represents a dislocation type of creep mechanism [27]. Dislocation creep, also called power-law creep, involves a more drastic motion of dislocations which are vacancies or some defects [27]. Figure 13 shows the relationship between the minimum creep strain rate and applied stress for variously aged GC-9 at 800 $^o$C. The fitted equation and correlation coefficient ($r$) for each curve in Fig. 13 are expressed as follows,

$$\text{Non-aged: } \dot{\varepsilon}_{min} = 6.59\,\sigma^{5.59} , \quad r^2 = 0.64 \tag{11}$$

$$\text{100h-aged: } \dot{\varepsilon}_{min} = 3.41\,\sigma^{16.47} , \quad r^2 = 0.94 \tag{12}$$

$$\text{1000 h-aged: } \dot{\varepsilon}_{min} = 5.67\,\sigma^{31.25} , \quad r^2 = 0.99 \tag{13}$$

where $\dot{\varepsilon}_{min}$ is the minimum creep strain rate in unit of s$^{-1}$ and $\sigma$ is the applied stress in unit of MPa. The non-aged GC-9 exhibits a higher minimum strain rate than do the 100 h-aged and 1000 h-aged ones under a similar constant load. The values of stress exponent ($n$) are 6, 16, and 31 for the non-aged, 100 h-aged, and 1000 h-aged GC-9, respectively. It indicates a power-law dislocation creep mechanism for the non-aged GC-9. There is limited

literature dealing with the higher stress exponent ($n > 8$) for glass-ceramics. Therefore, it is not clear at present whether there is any other creep mechanism, in addition to the power-law dislocation mechanism, is involved in the creep deformation of the 100 h-aged and 1000 h-aged GC-9.  However, a longer aging time and greater extent of crystallization exhibits a greater stress exponent value.


### 3.1.3 Creep rupture time


Figure 14 shows the relationship between the applied stress and creep rupture time at 800 $^o$C for variously aged GC-9.  As shown in Fig. 14, the creep rupture time for a given aged condition increases with a decrease in applied loading.  The relationship between the applied stress and creep rupture time can be described by a simple power law for each aged condition. The fitted equation and correlation coefficient ($r$) for each curve in Fig. 14 are expressed as follows,

Non-aged: $\quad \sigma t_r^{0.14} = 10.54, \quad r^2 = 0.79$ $\qquad$ (14)

100 h-aged: $\quad \sigma t_r^{0.051} = 13.49, \quad r^2 = 0.68$ $\qquad$ (15)

1000 h-aged: $\quad \sigma t_r^{0.067} = 23.12, \quad r^2 = 0.77$ $\qquad$ (16)

where $\sigma$ is the applied stress in unit of MPa and $t_r$ is time to rupture in unit of h.  The creep rupture time at 800 $^o$C for variously aged GC-9 can be estimated through these power-law relations.  The slope of the curve for the non-aged GC-9 is steeper than those of the 100 h-aged and 1000 h-aged ones. For the non-aged GC-9, the creep rupture time is longer than 1000 h when the applied apparent stress is less than 6 MPa.  For the 100 h-aged and 1000 h-aged GC-9, the maximum applied apparent stresses can be increased to 9 and 15 MPa, respectively, if the creep rupture time needs to be longer than 1000 h.  Again, this indicates that the creep resistance of GC-9 at 800 $^o$C can be improved through an aging treatment of crystallization.  The Weibull characteristic strength ($\sigma_o$) of variously aged GC-9 investigated by Yeh [12] is given in Table. 3.  The Weibull characteristic strength at 800 $^o$C for the non-aged, 100 h-aged, and 1000 h-aged GC-9 is 19 MPa, 34 MPa, and 38 MPa, respectively.  Therefore, the creep strength at 1000 h for the non-aged, 100 h-aged, and 1000 h-aged GC-9 is about 31%, 26%, and 39%, respectively, of the Weibull characteristic strength.  Apparently, a longer aging time of 1000 h significantly improves the creep strength of GC-9 glass-ceramic at 800 $^o$C.

### 3.1.4  Failure analysis

Typical failure patterns in the ring-on-ring specimens for a monotonic equibiaxial flexural strength test of ceramics are shown in Fig. 15 [30]. Fracture of the specimen broken into two or three pieces is a type of low-energy failure according to ASTM C1499 (Fig. 15) [30].   In the current study, the failure patterns of crept specimens are different from those in the flexural strength tests.   Figure 16 shows the failure patterns on the tensile surface under different constant loads for the non-aged GC-9.   Similar failure patterns are also observed for the crept specimens of the 100-h aged and 1000-h aged GC-9, as shown in Figs. 17 and 18, respectively.   The cracks for all the crept specimens initiated at the span between the inner load ring and the outer support ring.   For a high constant load, the cracks initiated near the outer support ring on the tensile surface and propagated along the periphery of the outer ring, as shown in Fig. 16(a).   The circular disk specimen of GC-9 under a high constant load didn't deform a lot before fracture, as shown in Fig. 16(a).

On the other hand, the cracks initiated near the inner loading ring given a low constant load.   Figure 16(b) shows the fracture pattern of a low-stress specimen which was not ruptured completely.   As shown in Fig. 16(b), the crack initiated on the tensile surface and then penetrated through the thickness when flexural deflection of the specimen continuously increased.   It is difficult to identify the crack initiation site by SEM analysis.   Porosity may be one of the reasons not to clearly identify the origin of failure.   Most of the characteristic fractographic features such as mirror, mist and hackle regions are not observed on the fracture surface due to a high level of porosity in the variously aged GC-9 specimens.   Figure 19 shows the possible failure origins of variously aged GC-9 specimens.   Some defects and cavities which are observed in Fig. 19 may be the failure origins.   Microcracks may initiate at the large defects and propagate on the tensile surface.   The microcracks may coalesce to become a large macrocrack which may also penetrate through the thickness due to the deflection of the plate in the secondary stage of creep, as shown in Fig. 16(b).   Once the macrocrack grows to a certain length along the circumference, rupture may occur suddenly in the tertiary stage of creep.

## 3.2 Creep Properties of Joint of Glass-Ceramic Sealant and Metallic Interconnect

### 3.2.1 Creep rupture behavior

Creep rupture characteristics of the joint of GC-9 glass-ceramic sealant and Crofer 22 H interconnect subjected to constant shear and tensile loads at 800 $^o$C are shown in Fig. 20 by plotting the applied stress versus creep rupture time.  Four constant loads (280 N, 200 N, 190 N, and 180 N) are applied for shear joint specimens (Fig. 20(a)).  For tensile joint specimens (Fig. 20(b)), the applied constant loads are 100 N, 80 N, 70 N, and 60 N.  As shown in Fig. 20, the relationship between the applied stress and creep rupture time can be well described by a simple power law for each loading mode.  The fitted equation and correlation coefficient ($r$) for each loading mode in Fig. 20 are expressed as follows,

shear loading:  $\tau t_r^{0.066} = 1.68, \quad r^2 = 0.90$ (17)

tensile loading:  $\sigma t_r^{0.074} = 1.85, \quad r^2 = 0.97$ (18)

where $\tau$ and $\sigma$ are the applied shear and tensile stresses in unit of MPa and $t_r$ is time to rupture in unit of h.  The creep rupture time for the joint specimen subjected to a constant shear or tensile load at 800 $^o$C can be estimated through these power-law relations thanks to the high correlation coefficient values.  As shown in Fig. 20, the creep rupture time increases with a decrease in applied stress for both loading modes.  For an applied constant stress of about 1.6 MPa, the creep rupture time is less than 10 h for both loading modes.  On the other hand, for a creep rupture time longer than 100 h, or even longer than 1000 h, the applied constant stress should be smaller than 1.1 MPa for both loading modes.  This applied shear stress level is about 23% of the average ultimate shear joint strength (4.7 MPa) [33].  In other words, the shear creep strength at 1000 h for the GC-9/Crofer 22 H joint at 800 $^o$C is about a quarter of the average ultimate shear joint strength.  The tensile creep strength at 1000 h is only about 9% of the average ultimate tensile joint strength (12.7 MPa) [33].

### 3.2.2 Failure analysis

Formation of adhesive oxide layers is the main mechanism of interfacial joining between the glass-ceramic sealant and metallic interconnect.  The bonding strength of the joint originates from the mutual Van Der Waals force

of the formed oxide layers. The high-temperature joining mechanism of the GC-9 glass-ceramic sealant and Crofer 22 H alloy involves formation of two oxide layers with a $Cr_2O_3$ layer on the surface of Crofer 22 H connected with a $BaCrO_4$ layer on the surface of GC-9 [33]. A spinel (($Cr,Mn)_3O_4$) layer is formed between these two oxide layers. Figure 21 shows the location of each oxide layer between Crofer 22 H and GC-9 glass-ceramic.

Figure 22 shows the failure patterns in the shear specimens tested at 800 °C. As shown in Fig. 22(a), for a short creep rupture time (< 100 h), cracks initiated at the interface between the spinel layer and $BaCrO_4$ layer at the periphery of the joining area and propagated into the $BaCrO_4$ layer, followed by final, fast fracture at the inner glass-ceramic substrate. Evidences of microstructural observation for selected regions in the fracture surfaces of Fig. 22(a) are provided as follows. Optical and SEM micrographs of two outlined regions of the fracture surface without adhered glass-ceramic in the upper micrograph of Fig. 22(a) are shown in Fig. 23. Figure 23(b) shows a microstructure of (($Cr,Mn)_3O_4$) spinel layer. The $BaCrO_4$ chromate layer shown in Fig. 23(c) has some embedded spinels. Figure 24 shows the optical and SEM micrographs of two outlined regions of the fracture surface with adhered glass-ceramic in the lower micrograph of Fig. 22(a). The counterpart of region 1 in Fig. 23(b) is shown in Fig. 24(b) which indicates a chromate structure. A similar microstructure in Fig. 23(c) is also observed in Fig. 24(c).

For a medium-term creep rupture time (100 h $< t_r <$ 1000 h), cracking first took place peripherally at the interface between the spinel layer and $BaCrO_4$ layer (yellow region in the lower micrograph of Fig. 22(b)), and then proceeded inward through the $BaCrO_4$ layer and along the interface between the chromate layer and glass-ceramic substrate (pink region in the lower micrograph of Fig. 22(b)). The lime green film in the upper micrograph of Fig. 22(b) is a $BaCrO_4$ layer near the Crofer 22 H side. Optical and SEM micrographs of an outlined region of the fracture surface with adhered glass-ceramic in the lower micrograph of Fig. 22(b) are shown in Fig. 25. As shown in Fig. 25(a), there are two distinct zones in the outlined region, pink and light green. The pink region contains some residual chromate left on the GC-9 glass-ceramic and the light green one is the chromate ($BaCrO_4$). By means of EDS analysis, element distributions in these zones are confirmed and shown in Fig. 26. A high intensity of Si and Al is found in the region of GC-9 glass-ceramic, as shown in Fig. 26(c) and (f). The region having a high intensity of Cr (Fig. 26(b)) and Ba (Fig. 26(d)) agrees with the corresponding $BaCrO_4$ layer.

For a creep rupture time longer than 1000 h, four regions of different colors (yellow, pink, red, and brown) are observed in the lower micrograph of Fig. 22(c). A linescan module of the SEM was applied to detect the major chemical elements in these regions. The analyzed area is outlined in the

micrograph shown in Fig. 27(a). Each region in the observed area is labeled with the corresponding color, as shown in the SEM micrograph of Fig. 27(b). The arrow in Fig. 27(b) shows the direction of linescan from bottom to top. A high intensity of Cr is found in the yellow region in comparison with the other regions, as shown in Fig. 28(f). The yellow region is the interface between the spinel layer and chromate ($BaCrO_4$) layer. The intensity of Al, Ca, and Si which are the compositions of GC-9 glass-ceramic is lower than that of Cr at this yellow interface. Note that all of the pink, red, and brown regions in Fig. 27(b) are the residual chromate left on the GC-9 glass-ceramic substrate. In the upper micrograph of Fig. 22(c), some white glass-ceramic spots are left on the Crofer 22 H surface, corresponding to the pink, red, and brown regions in the lower micrograph of Fig. 22(c). The pink, red, and brown colors indicate that some chromate is left on the white glass-ceramic substrate. Fig. 29(a) shows the cross section of the outlined region in Fig. 27(a) with various colors. Four regions of different colors are labelled in Fig. 29(a). As shown in Fig. 29(a), the red and brown regions are higher than the pink one. Similar to that in Fig. 25 of a medium-term creep rupture time, the pink region in Fig. 27(b) contains some leftover chromate spots. Fig. 29(b) shows the outlined region in Fig. 29(a) and indicates the oxide layers between GC-9 glass-ceramic and Crofer 22 H. Various microstructures are visible in the micrograph of back-scattered electron (BSE) mode (Fig. 29(b)). Chromate in the four color regions are shown in Fig. 30 with both secondary electron (SE) and BSE modes. As shown in Fig. 30(b), the black layer on GC-9 glass-ceramic is the chromate layer. For pink region, there exist some black spots of chromate in Fig. 30(d). More chromate is observed in red and brown regions, as shown in Fig. 30(f) and (h). Apparently, a greater amount of chromate is left on the glass-ceramic substrate in the deep color regions (red and brown). An in-situ diffusion mechanism took place between the GC-9 glass-ceramic and Crofer 22 H alloy during a long-term creep test such that the fractured GC-9 layer shows different colors on the crack propagating path. The yellow region which is the initial cracking area represents a weaker interface between the spinel layer and $BaCrO_4$ layer. The slow crack growth regions (pink, red, and brown) accompany a leftover chromate layer on the GC-9 substrate by continuous Cr diffusion from Crofer 22 H alloy. Final fast fracture occasionally occurs within the white glass-ceramic substrate. Therefore, the crack propagating path in the shear specimens with a much longer rupture time (> 1000 h) is similar to that with a medium-term rupture time. In the previous study of Chen [33], fracture surface in the GC-9 glass-ceramic layer of a 1000-h pre-aged joint specimen also shows a brown color, as shown in Fig. 31(a). That joint specimen was aged at 800 $^o$C for 1000 h first before undergoing a shear strength test at 800 $^o$C. For non-aged or short-term aged (250 h and 500 h) specimens, the GC-9 glass-ceramic layer on the fracture surface exhibits a white color after a shear

strength test at 800 $^{\circ}$C [33].

In the present study, comparison of the GC-9 glass-ceramic microstructure of two different rupture times (Fig. 22(b) and (c)) is shown in Fig. 32. For a rupture time longer than 1000 h, needle-shape crystalline phases (alpha-Ba(Al$_2$Si$_2$O$_8$)) are observed in the brown region, as shown in Fig. 32(b). This type of crystalline phase is not found in the medium-term (100 h $< t_r <$ 1000 h) crept specimen (Fig. 32(a)). Apparently, an in-situ crystallization mechanism took place in the glass-ceramic layer and caused the glass-ceramic layer to become brittle in a long-term crept specimen. Therefore, the crack initiated at the weakest spinel/BaCrO$_4$ interface firstly, penetrated through the chromate layer, and propagated along the interface between the chromate layer and glass-ceramic substrate with brittle crystalline phases during a long-term creep test. SEM micrographs of various color regions in the lower part of Fig. 22(c) are shown in Fig. 33. As mentioned above, the yellow region is the interface between the spinel layer and chromate (BaCrO$_4$) layer, as shown in Fig. 33(a). The pink region (Fig. 33(b)) exhibits some needle-shape crystanlline phases with some chromate spots. Both red and brown regions exhibit some flat facets shown in Fig. 27(b). Some needle-shape crystanlline phases are observed beneath the flat chromate layer, as shown in Fig. 33(c) and (d). For a GC-9 glass-ceramic disk sample aged at 800 $^{\circ}$C for 1000 h, no color change into red or brown is observed. An exhibition of different colors on the fracture surface is attributed to existence of the BaCrO$_4$ chromate on the glass-ceramic substrate. When the chromate layer is left on the Crofer 22 H side, a lime green color is observed. When the chromate layer is left on the glass-ceramic substrate, pink, red, and brown colors are observed. Therefore, the chromate layer is related to the change of glass-ceramic color on the fracture surface of the crept shear specimens.

The failure patterns for tensile specimens tested at 800 $^{\circ}$C are shown in Fig. 34. Figure 34(a) shows fracture of a short rupture time ($<$ 10 h) occurred at the interface between the chromate (BaCrO$_4$) layer and the spinel ((Cr,Mn)$_3$O$_4$) layer. Optical and SEM micrographs of an outlined region without adhered glass-ceramic in the upper micrograph of Fig. 34(a) are shown in Fig. 35. As shown in Fig. 35(a), the spinels embedded in the chromate layer are observed in the black region. Figure 35(c) and (d) show the microstructures in the black region and GC-9 glass-ceramic substrate, respectively. No needle-shape crystalline phase in the glass-ceramic substrate is observed (Fig. 35(d)). Figure 36 shows the optical and SEM micrographs of an outlined region in the lower micrograph of Fig. 34(a). Two distinct zones, white and lime green, in the outlined region of Fig. 36(a) represent the GC-9 glass-ceramic substrate and chromate, respectively. The chromate layer has some leftover spinels, as shown in Fig. 36(c).

For a medium rupture time (100 h $< t_r <$ 1000 h) under tensile loading, as

shown in Fig. 34(b), cracking took place at the interface between the chromate layer and spinel layer firstly, and then penetrated through the chromate layer into the interface between the chromate layer and glass-ceramic substrate.   The pink region represents some leftover chromate on the glass-ceramic substrate.   SEM micrographs of an outlined region without adhered glass-ceramic in the upper micrograph of Fig. 34(b) are shown in Fig. 37.   Figure 37(b) shows the SEM micrograph of the outlined region in Fig. 37(a).   High-magnification SEM micrographs of the spinel layer and glass-ceramic substrate are presented in Fig. 37(c) and (d), respectively.   The microstructure of GC-9 substrate in Fig. 37(d) is different from that in Fig. 35(d).   The crystalline phases found in Fig. 37(d) are formed during a longer creep test.   As shown in Fig. 38 of the EDS analysis results, the high-intensity Cr and Mn areas bounded by the dash line agree with the region of the spinel layer (Fig. 37(b)).   Figure 39 shows the optical and SEM micrographs of an outlined region in the lower micrograph of Fig. 34(b).   Figure 39(c) shows the microstructure of the chromate layer which is the lime green region in Fig. 39(a).   It appears that cracking took place at the spinel/chromate interface firstly.   As shown in Fig. 39(d), the microstructure of the residual chromate on the glass-ceramic substrate (the pink region in Fig. 39(a)) is similar to that in Fig. 37(d).   It implies that the crack propagated along the interface between the chromate layer and glass-ceramic substrate in a later stage.   EDS mapping results of the area shown in Fig. 39(b) confirm the corresponding regions of the chromate layer and the GC-9 substrate with some leftover chromate, as shown in Fig. 40.

Optical and SEM micrographs of an outlined region of the fracture surface in the upper micrograph of Fig. 34(c) for a rupture time longer than 500 h are shown in Fig. 41.   Microstructure of the spinel layer in Fig. 41(b) is shown in Fig. 41(c).   Figure 42 shows the optical and SEM micrographs of two outlined regions in the lower micrograph of Fig. 34(c).   It seems that cracking took place at the interface between the spinel layer and the chromate layer firstly, followed by propagation along the interface between the chromate layer and glass-ceramic substrate (pink and red regions in Fig. 42(a)).   The regions 1 and 2 in Fig. 42(a) represent the pink and red regions, respectively.   The different colors indicate a different thickness in the chromate layer.   Microstructures of these two regions are shown in Fig. 42(b) and (c).   The amount of pores increases in the red region.   It implies that the glass-ceramic substrate becomes brittle due to a crystallization mechanism. Therefore, the crack initiated and grew at the spinel/$BaCrO_4$ interface firstly and then propagated along the interface between the chromate layer and glass-ceramic substrate containing brittle crystalline phases during a long-term tensile creep test.

In summary, for both shear and tensile loading modes, cracking of the crept joint specimens initiated and grew at the spinel/chromate interface along

the periphery of the joining area.  The crack then penetrated through the chromate layer and propagated along the interface between the chromate layer and glass-ceramic substrate.  Final fast fracture occasionally took place within the glass-ceramic layer.  Figure 43 shows a schematic of crack propagation path in both loading modes.  The sites corresponding to different colors observed in the fracture surfaces of both shear and tensile loading modes are summarized in Table 4.

## 3.3  Fracture Toughness of PEN

Figure 44 shows the Vickers indentation impressions on both sides of a half cell.  Cracks extending from the corner of the impression on the anode side are observed in Fig. 44(a).  On the electrolyte side, no apparent cracks are observed in Fig. 44(b).  The reason is that porosity in the anode is larger than that in the electrolyte.  The values of hardness calculated by Eq. (6) for anode and electrolyte are 14.39 GPa and 11.42 GPa, respectively.  For a full PEN cell, the impressions of Vickers indentation on both sides are shown in Fig. 45.  The values of hardness for anode and cathode are 4.70 GPa and 1.23 GPa, respectively.  No extending cracks are observed on the anode side of the full cell.  Because of the absence of extending cracks for anode in the full cell, the parameter $I_o$ of P-type can not be determined.  Therefore, the R-type equation (Eq. 7) is used to estimate the fracture toughness of the given two cells.  The values of fracture toughness of anode and electrolyte in a half cell are 4.11 MPa $\cdot$ m$^{1/2}$ and 4.09 MPa $\cdot$ m$^{1/2}$, respectively.  For a full cell, the values of fracture toughness of anode and cathode are 5.82 MPa $\cdot$ m$^{1/2}$ and 0.96 MPa $\cdot$ m$^{1/2}$, respectively.  A greater porosity for cathode results in the lower value of fracture toughness, as shown in Fig. 45(b).  Therefore, the materials with a less amount of pores such as anode and electrolyte have higher values of fracture toughness.  The hardness and Vickers indentation fracture toughness values for the given full cell and half cell are summarized in Table 5.

## 4. CONCLUSIONS

(1) The extent of crystallization in the GC-9 glass-ceramic sealant is increased with a longer aging time. The crystallinity for the non-aged, 100 h-aged, and 1000 h-aged GC-9 is 40%, 42%, and 49%, respectively.

(2) Given an applied constant load, the creep rupture time of the 1000 h-aged GC-9 at 800 $^{\circ}$C is much longer than those of the non-aged and 100 h-aged ones. The non-aged GC-9 exhibits a higher minimum strain rate than do the 100 h-aged and 1000 h-aged ones. Therefore, GC-9 with a higher degree of crystallinity is more resistant to creep at 800 $^{\circ}$C.

(3) The values of creep stress exponent ($n$) are 6, 16, and 31 for the non-aged, 100 h-aged, and 1000 h-aged GC-9, respectively. The GC-9 with a longer aging time and greater extent of crystallization exhibits a greater stress exponent value.

(4) If the creep rupture time needs to be longer than 1000 h for the non-aged, 100 h-aged, and 1000 h-aged GC-9, the applied apparent stress should be less than 6 MPa, 9 MPa, and 15 MPa, respectively. It indicates that the creep resistance of GC-9 at 800 $^{\circ}$C can be improved through an aging treatment of crystallization.

(5) Fractography analysis results indicate that cracks in the crept, non-aged and aged GC-9 specimens initiate near the outer support ring on the tensile surface and propagate along the periphery of the outer ring for a high constant load. On the other hand, the cracks initiate near the inner loading ring given a low constant load.

(6) For the creep test of the Crofer 22 H/GC-9/Crofer 22 H joint specimens at 800 $^{\circ}$C, the creep rupture time is shorter than 10 h when the applied stress is about 1.6 MPa and above in both shear and tensile loading modes. If the applied stress is smaller than 1.1 MPa, the creep rupture time is over 1000 h for both loading modes. The shear creep strength at 1000 h at 800 $^{\circ}$C is about a quarter of the average ultimate shear joint strength. The tensile creep strength at 1000 h is only about 9% of the average ultimate tensile joint strength.

(7) For both shear and tensile joint specimens, creep cracking first takes place at the spinel/$BaCrO_4$ interface followed by penetration through the $BaCrO_4$ layer and propagation along the interface between the chromate layer and glass-ceramic substrate. Final fast fracture occasionally takes

place within the glass-ceramic layer.

(8) An exhibition of various color regions in the glass-ceramic substrate on the fracture surface is attributable to the formation of chromate. When the chromate layer is left on the Crofer 22 H side, a lime green color is observed. When the chromate layer is left on the glass-ceramic substrate, pink, red, and brown colors are also observed. Therefore, the chromate layer is related to the change of glass-ceramic color on the fracture surface of the crept specimens.

# REFERENCES

1. N. Q. Minh, "Solid Oxide Fuel Cell Technology-Features and Applications," *Solid State Ionics*, Vol. 174, pp. 271-277, 2004.

2. R. Bove and S. Ubertini, *Modeling Solid Oxide Fuel Cells Methods, Procedures and Techniques*, 1st Ed., Springer, New York, 2008.

3. T. L. Wen, D. Wang, M. Chen, H. Tu, Z. Lu, Z. Zhang, H. Nie, and W. Huang, "Material Research for Planar SOFC Stack," *Solid State Ionics*, Vol. 148, pp. 513-519, 2002.

4. M. Radovic and E. Lara-Curzio, "Mechanical Properties of Tape Cast Nickel-Based Anode Materials for Solid Oxide Fuel Cells Before and After Reduction in Hydrogen," *Acta Materialia*, Vol. 52, pp. 5747–5756, 2004.

5. G. Kaur, O. P. Pandey, and K. Singh, "Interfacial Study Between High Temperature $SiO_2$-$B_2O_3$-AO-$La_2O_3$ (A= Sr, Ba) Glass Seals and Crofer 22APU for Solid Oxide Fuel Cell Applications," *International Journal of Hydrogen Energy*, Vol. 37, pp. 6862-6874, 2012.

6. J. W. Fergus, "Sealants for Solid Oxide Fuel Cells," *Journal of Power Sources*, Vol. 147, pp. 46-57, 2005.

7. J. Fergus, R. Hui, X. Li, D. P. Wilkinson, and J. Zhang, *Solid Oxide Fuel Cells: Materials Properties and Performance*, CRC Press, New York, USA, 2008.

8. C.-K. Liu, T.-Y. Yung, and K.-F. Lin, "Effect of La Addition on the Thermal and Crystalline Properties of $SiO_2$-$B_2O_3$-$Al_2O_3$-BaO Glasses," *Proceedings of the Annual Conference of the Chinese Ceramic Society*, 2007 (CD-ROM). (in Chinese)

9. C.-K. Liu, T.-Y. Yung, S.-H. Wu, and K.-F. Lin, "Study on a $SiO_2$-$B_2O_3$-$Al_2O_3$-BaO Glass System for SOFC Applications," *Proceedings of the MRS_Taiwan Annual Meeting*, 2007 (CD-ROM). (in Chinese)

10. C.-K. Liu, T.-Y. Yung, and K.-F. Lin, "Isothermal Crystallization Properties of $SiO_2$-$B_2O_3$-$Al_2O_3$-BaO Glass," *Proceedings of the Annual Conference of the Chinese Ceramic Society*, 2008 (CD-ROM). (in Chinese)

11. H.-T. Chang, "High-Temperature Mechanical Properties of a Glass Sealant for Solid Oxide Fuel Cell," Ph.D. Thesis, National Central University, 2010.

12. J.-H. Yeh, "Analysis of High-Temperature Mechanical Durability for the Joint of Glass Ceramic Sealant and Metallic Interconnect for Solid Oxide Fuel Cell," M.S. Thesis, National Central University, 2011.

13. P. A. Lessing, "A Review of Sealing Technologies Applicable to Solid Oxide Electrolysis Cells," *Journal of Materials Science*, Vol. 42, pp. 3465-3476, 2007.

14. C.-K. Lin, T.-T. Chen, Y.-P. Chyou, and L.-K. Chiang, "Thermal Stress Analysis of a Planar SOFC Stack," *Journal of Power Sources,* Vol. 164, pp. 238-251, 2007.

15. A.-S. Chen, "Thermal Stress Analysis of a Planar SOFC Stack with Mica Sealants," M.S. Thesis, National Central University, 2007.

16. C.-K. Lin, L.-H. Huang, L.-K. Chiang, and Y.-P. Chyou, "Thermal Stress Analysis of a Planar Solid Oxide Fuel Cell Stacks: Effects of Sealing Design," *Journal of Power Sources,* Vol. 192, pp. 515-524, 2009.

17. Y.-S. Chou, J. W. Stevenson, and P. Singh, "Effect of Pre-Oxidation and Environmental Aging on the Seal Strength of a Novel High-Temperature Solid Oxide Fuel Cell (SOFC) Sealing Glass with Metallic Interconnect," *Journal of Power Sources*, Vol. 184, pp. 238-244, 2008.

18. V. A. Haanappel, V. Shemet, I. C. Vinke, and W. J. Quadakkers, "A Novel Method to Evaluate the Suitability of Glass Sealant-Alloy Combinations under SOFC Stack Conditions," *Journal of Power Sources*, Vol. 141, pp. 102-107, 2005.

19. K. S. Weil, J. E. Deibler, J. S. Hardy, D. S. Kim, G.-G. Xia, L. A. Chick, and C. A. Coyle, "Rupture Testing as a Tool for Developing Planar Solid Oxide Fuel Cell Seals," *Journal of Materials Engineering and Performance*, Vol. 13, pp. 316-326, 2004.

20. F. Smeacetto, M. Salvo, M. Ferraris, V. Casalegno, P. Asinari, and A. Chrysanthou, "Characterization and Performance of Glass-Ceramic Sealant to Join Metallic Interconnects to YSZ and Anode-Supported-Electrolyte in Planar SOFCs," *Journal of the European Ceramic Society*, Vol. 28, pp. 2521-2527, 2008.

21. E. V. Stephens, J. S. Vetrano, B. J. Koeppel, Y. Chou, X. Sun, and M. A. Khaleel, "Experimental Characterization of Glass-Ceramic Seal Properties and their Constitutive Implementation in Solid Oxide Fuel Cell Stack Models," *Journal of Power Sources*, Vol. 193, pp. 625-631, 2009.

22. J. Malzbender, J. Mönch, R. W. Steinbrech, T. Koppitz, S. M. Gross, and J. Remmel, "Symmetric Shear Test of Glass-Ceramic Sealants at SOFC Operation Temperature," *Journal of Materials Science*, Vol. 42, pp. 6297-6301, 2007.

23. Y.-S. Chou, J. W. Stevenson, and P. Singh, "Effect of Aluminizing of Cr-Containing Ferritic Alloys on the Seal Strength of a Novel High-Temperature Solid Oxide Fuel Cell Sealing Glass," *Journal of Power Sources*, Vol. 185, pp. 1001-1008, 2008.

24. F. Smeacetto, M. Salvo, P. Leone, M. Santarelli, and M. Ferraris, "Performance and Testing of Joined Crofer22APU-Glass-Ceramic Sealant-Anode Supported Cell in SOFC Relevant Conditions," *Materials Letters*, Vol. 65, pp. 1048-1052, 2011.

25. J. Mihans, M. Khaleel, X. Sun, and M. Tehrani, "Creep Properties of Solid Oxide Fuel Cell Glass-Ceramic Seal G18," *Journal of Power Sources*, Vol. 195, pp. 3631-3635, 2010.

26. D. W. Richerson, *Modern Ceramic Engineering*, 2nd Ed., Marcel Dekker, New York, USA, 1992.

27. N. E. Dowling, *Mechanical Behavior of Materials: Engineering Methods for Deformation, Fracture, and Fatigue*, 3rd Ed., Prentice Hall, New Jersey, USA, 2007.

28. J. Milhans, D. S. Li, M. Khaleel, X. Sun, M. S. Al-Haik, A. Harris, and H. Garmestani, "Mechanical Properties of Solid Oxide Fuel Cell Glass-Ceramic at High Temperatures," *Journal of Power Sources*, Vol. 196, pp. 5599-5603, 2011.

29. J. Malzbender, R. W. Steinbrech, and L. Singheiser, "Determination of the Interfacial Fracture Energies of Cathodes and Glass Ceramic Sealants in a Planar Solid-Oxide Fuel Cell Design," *Journal of Material Research*, Vol. 18, pp. 929-934, 2003.

30. "Standard Test Method for Monotonic Equibiaxial Flexural Strength of

Advanced Ceramics at Ambient Temperature," *ASTM Standard C1499*, ASTM International, West Conshohocken, PA, USA, 2008.

31. R. W. Schmitt, K. Blank, and G. Schönbrunn, "Experimentelle Spannungsanalyse zum Doppelringverfahren," *Sprechsaal*, Vol. 116, pp. 397-409, 1983. (in German)

32. Y.-T. Chiu and C.-K. Lin, "Effects of Nb and W Additions on High-Temperature Creep Properties of Ferritic Stainless Steels for Solid Oxide Fuel Cell Interconnect," *Journal of Power Sources*, Vol. 198, pp. 149-157, 2012.

33. J.-Y. Chen, "Analysis of Mechanical Properties for the Joint of Metallic Interconnect and Glass Ceramic in Solid Oxide Fuel Cell," M.S. Thesis, National Central University, 2010.

34. P. G. Charalambides, J. Lund, A. G. Evans, and R. M. McMeeking, "A Test Specimen for Determining the Fracture Resistance of Bimaterial Interfaces," *Journal of Applied Mechanicals,* Vol. 56, pp. 77-82. 1989.

35. G. D. Quinn and R. C. Bradt, "On the Vickers Indentation Fracture Toughness Test," *Journal of the American Ceramic Society*, Vol. 90, pp. 673-680, 2007.

36. "Standard Test Method for Vickers Indentation Hardness of Advanced Ceramics," *ASTM Standard C1327*, ASTM International, West Conshohocken, PA, USA, 2012.

37. J. H. Gong, "Determining Indentation Toughness by Incorporating True Hardness into Fracture Mechanics Equation," *Journal of the European Ceramic Society*, Vol. 19, pp. 1585-1592, 1999.

38. P. Chantikul, G. R. Anstis, B. R. Lawn, and D. B. Marshall, "A Critical Evaluation of Indentation Techniques for Measuring Fracture Toughness: II, Strength Method," *Journal of the American Ceramic Society*, Vol. 64, pp. 539-543, 1981.

39. G. Fantozzi, J. Chevalier, C. Olagnon, and J. L. Chermant, "Creep of Ceramic Matrix Composites," pp. 115-162 in *Comprehensive Composite Materials, Vol. 4: Carbon/Carbon, Cement, and Ceramic Matrix Composites*, edited by A. Kelly, and C. Zweben, Pergamon, Fresno, USA, 2000.

Table 1　Chemical composition of Crofer 22 H alloy (in wt.%)

| Fe | C | Cr | Mn | Si | Ti | Nb |
|---|---|---|---|---|---|---|
| Bal. | 0.007 | 22.93 | 0.43 | 0.21 | 0.07 | 0.51 |

| Cu | S | P | Al | W | La | |
|---|---|---|---|---|---|---|
| 0.02 | <0.002 | 0.014 | 0.02 | 1.94 | 0.08 | |

Table 2　Mechanical property of Crofer 22 H alloy [32]

| Temperature ($^{o}$C) | Yield strength (MPa) | Ultimate tensile strength (MPa) | Young's modulus (GPa) | Elongation (in 12 mm) (%) |
|---|---|---|---|---|
| 25 | 406 | 567 | 205 | 27 |
| 600 | 286 | 359 | 181 | 29 |
| 650 | 241 | 295 | 161 | 30 |
| 700 | 204 | 219 | 142 | 39 |
| 750 | 140 | 147 | 88 | 54 |
| 800 | 120 | 123 | 86 | 55 |

Table 3　Weibull characteristic strength ($\sigma_o$) and Weibull modulus ($m$) for variously aged GC-9 glass at different temperatures [12]

| | | Temperature | | | | |
|---|---|---|---|---|---|---|
| | Aged condition | 25 $^{o}$C | 650 $^{o}$C | 700 $^{o}$C | 750 $^{o}$C | 800 $^{o}$C |
| | Non-aged | 42 | 54 | 51 | 36 | 19 |
| $\sigma_o$ (MPa) | 100 h-aged | 41 | 53 | 63 | 59 | 34 |
| | 1000 h-aged | 49 | 67 | 61 | 64 | 38 |
| | Non-aged | 4 | 5.2 | 5 | 6 | 5.8 |
| $m$ | 100 h-aged | 5.5 | 5 | 4.8 | 4.9 | 6 |
| | 1000 h-aged | 6.5 | 4.8 | 4.2 | 5.4 | 5.3 |

Table 4　Sites of different colors in fracture surfaces of both shear and tensile loading modes

| Color | Site |
|-------|------|
| Yellow | Spinel/chromate interface |
| Pink | Chromate spots on top of GC-9 |
| Red | Chromate/GC-9 interface on top of GC-9 |
| Brown | Chromate/GC-9 interface on top of GC-9 |

Table 5　Hardness and fracture toughness of a full cell and a half cell by Vickers indentation

| Cell type | Side | Hardness (GPa) | R-type $K_{IC}$ (MPa $\cdot$ m$^{1/2}$) |
|-----------|------|----------------|------------------|
| Full cell | Anode | 4.70±1.10 | 5.82±0.30 |
|  | Cathode | 1.23±0.13 | 0.96±0.19 |
| Half cell | Anode | 14.39±1.38 | 4.11±0.96 |
|  | Electrolyte | 11.42±0.86 | 4.09±0.80 |
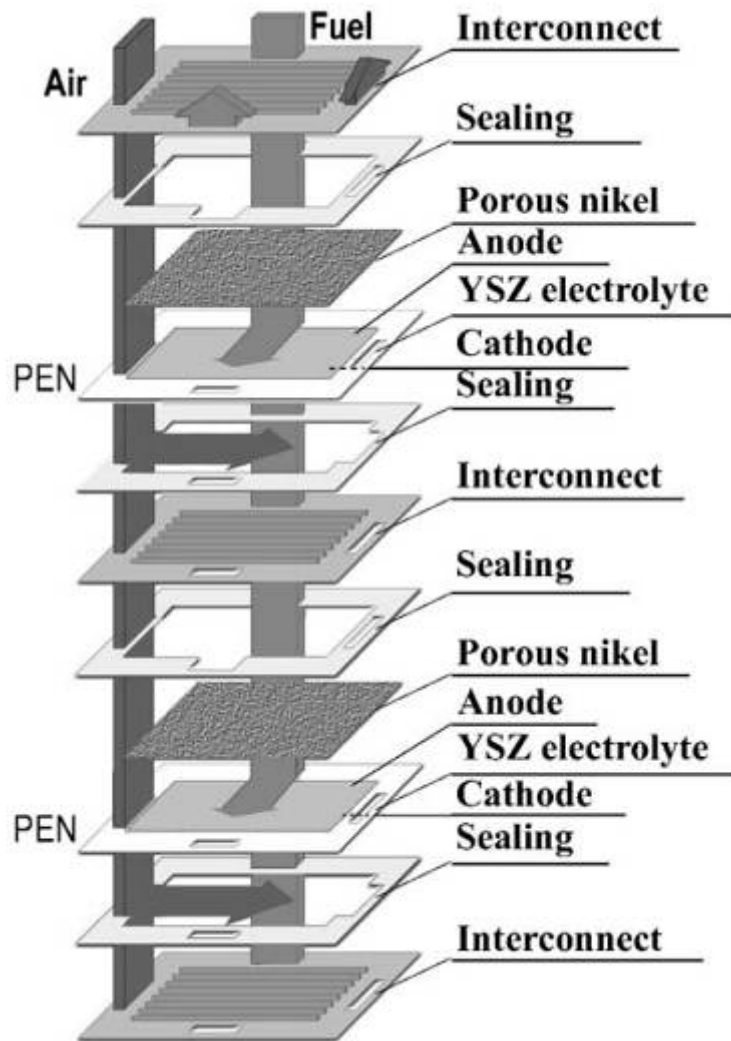
Fig. 1    Structural scheme of a planar SOFC stack. [3]
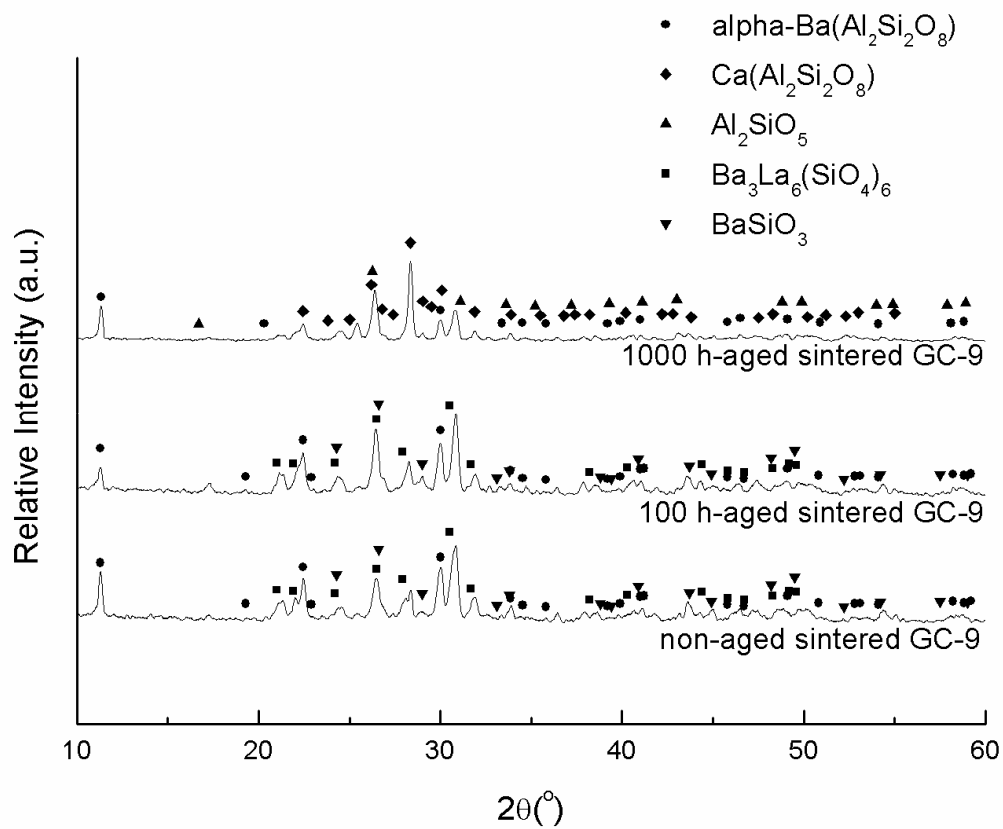
Fig. 2    XRD patterns of GC-9 glass in various conditions. [12] (Note data of the non-aged and 100 h-aged conditions are taken from Ref. [11].)
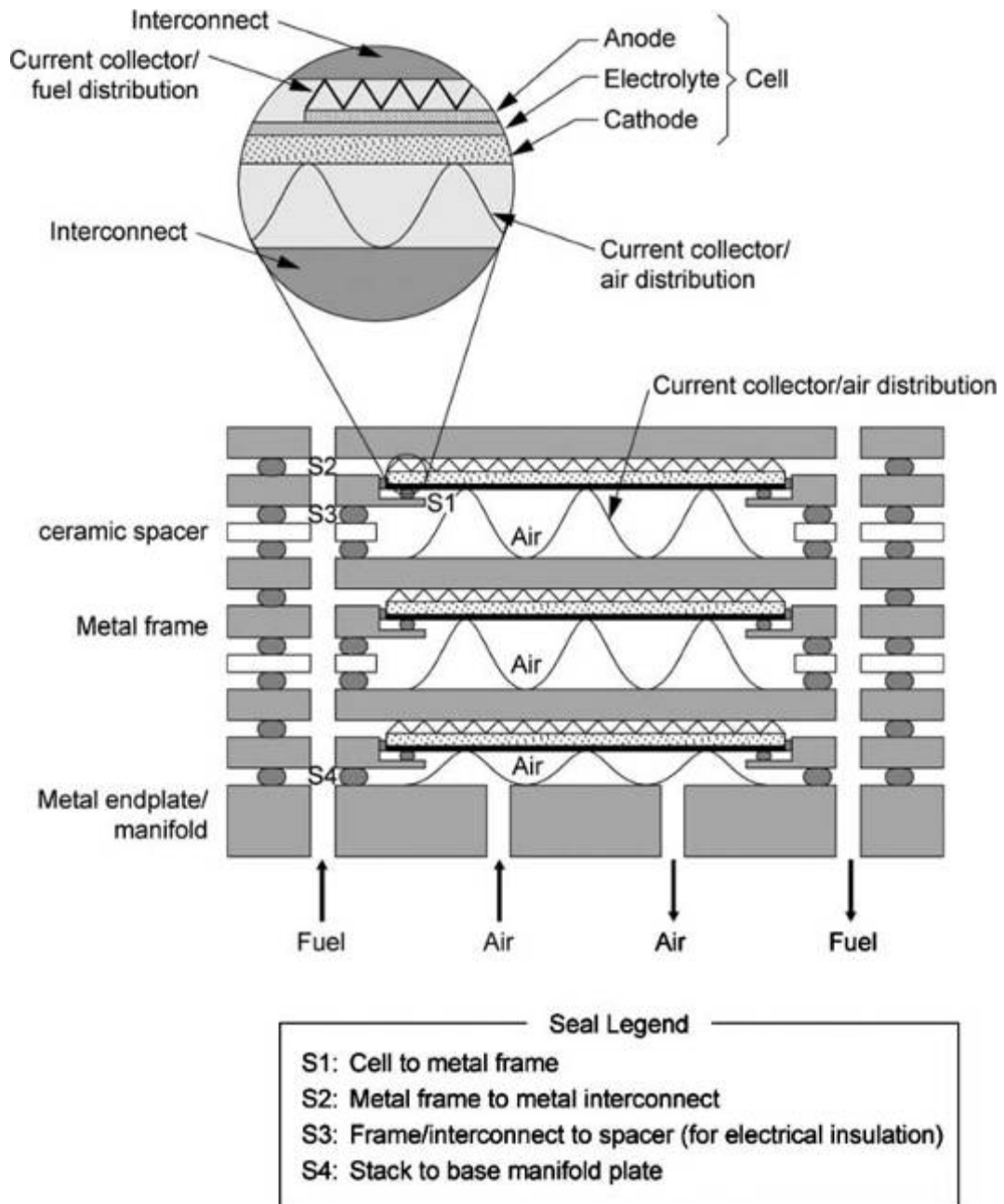
Fig. 3    Scheme of seals used in a planar SOFC stack with metallic interconnects and metallic internal gas manifold channels. [13]
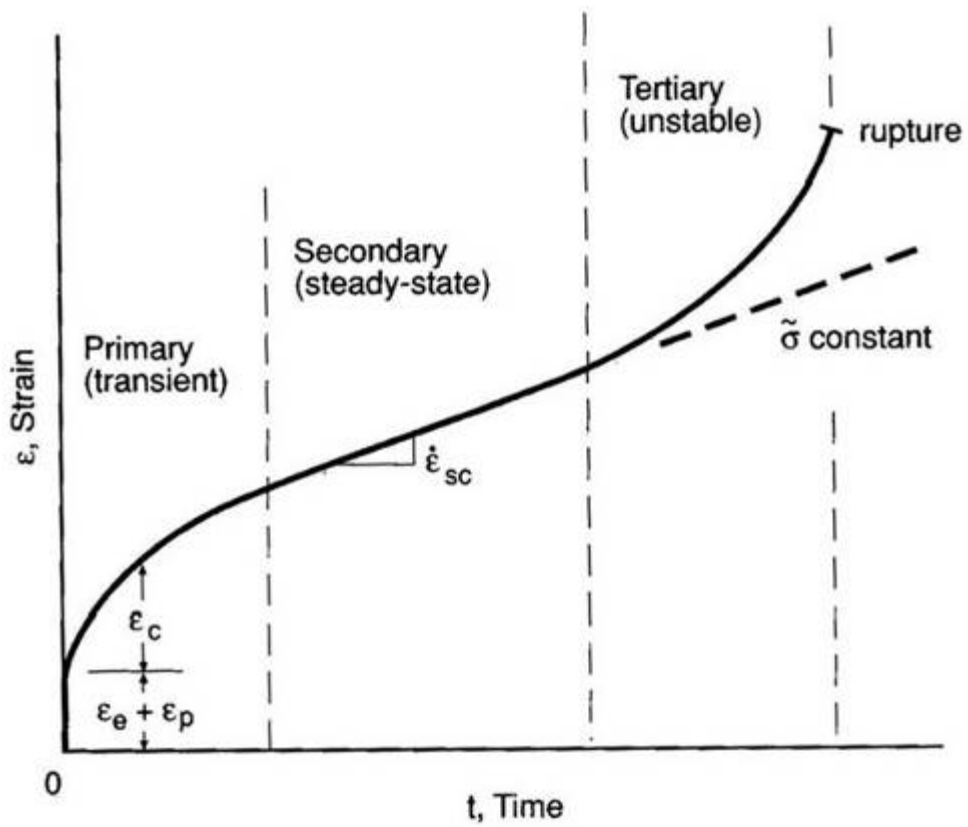
Fig. 4    A typical strain-time relationship during creep under constant load. [27]
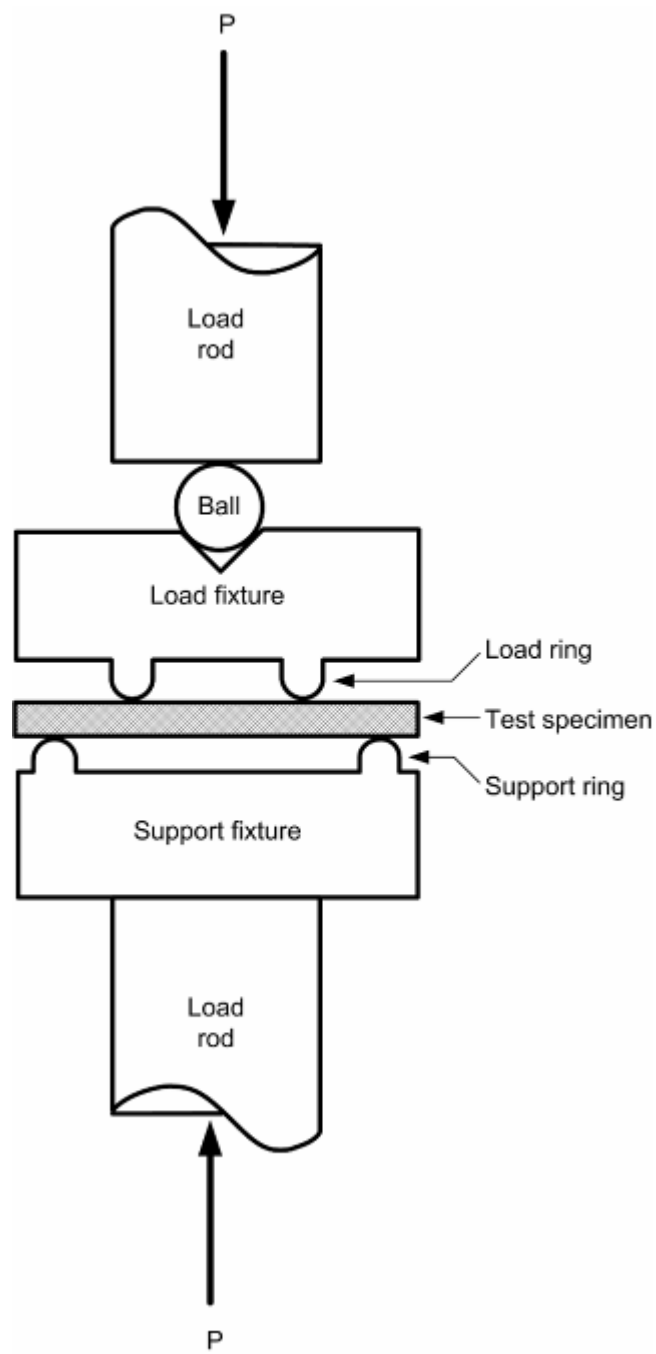
Fig. 5     Schematic of ring-on-ring test fixture.
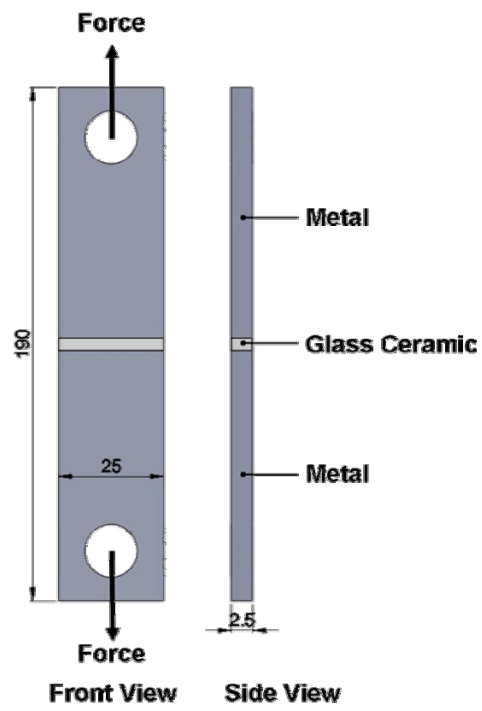
(a)
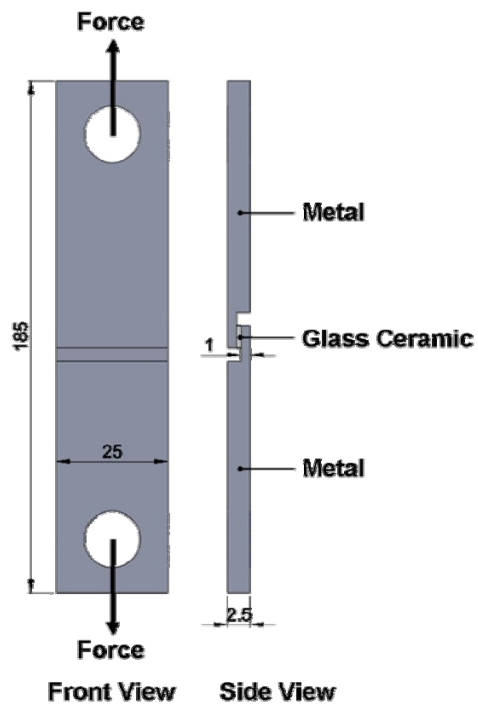


(b)

Fig. 6    Scheme of two types of joint specimens: (a) tensile specimen; (b) shear specimen.
(Dimensions: mm)
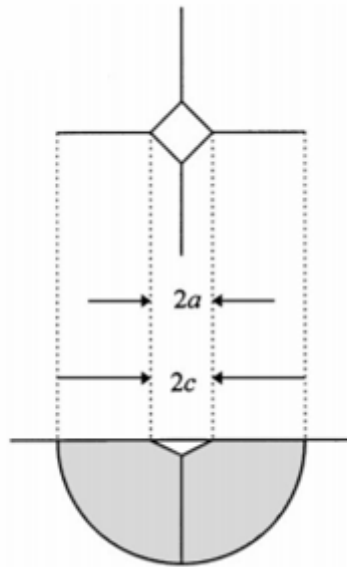
(a)
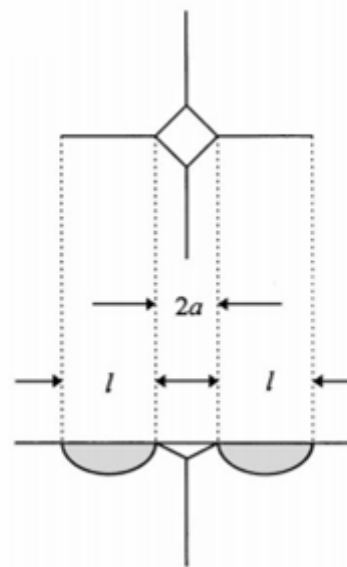


(b)

Fig. 7     Crack types around a Vickers indentation: (a) median/radial; (b) Palmqvist. [40]
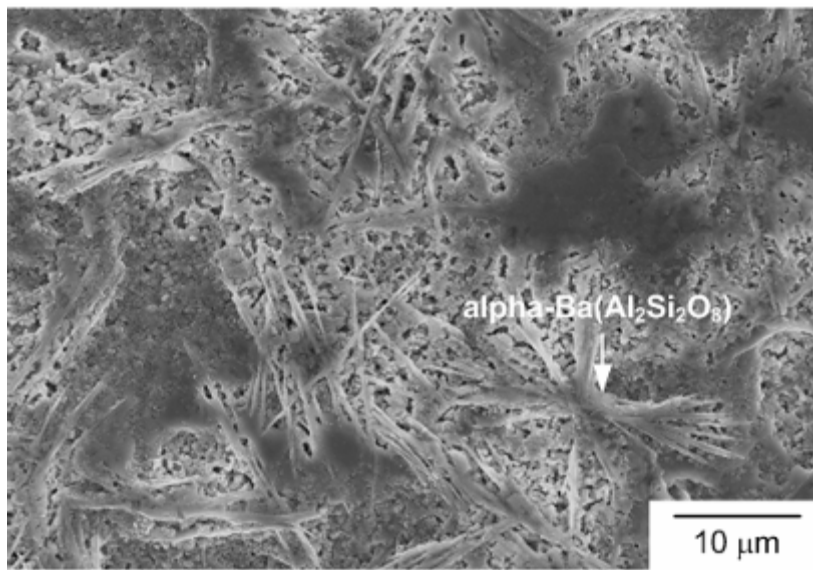
(a)
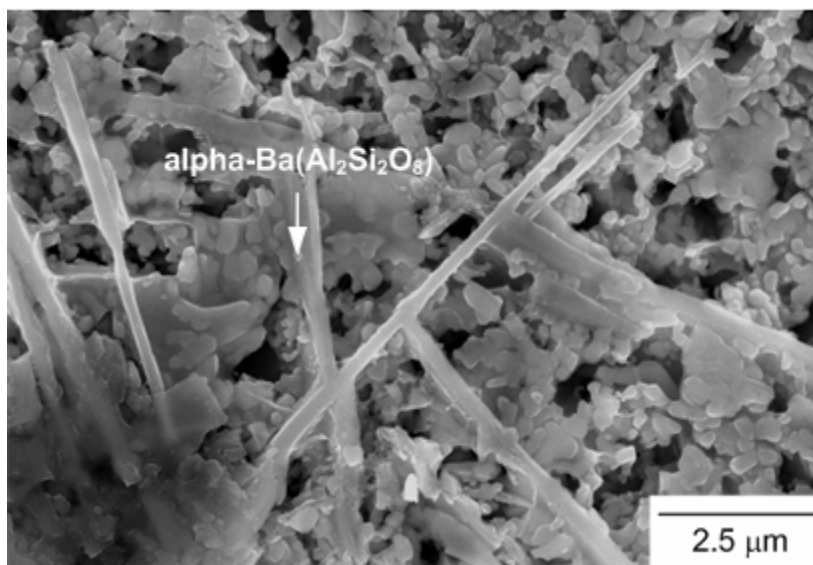


(b)

Fig. 8    Microstructure of non-aged GC-9 glass-ceramic: (a) low magnification; (b) high magnification. [11]
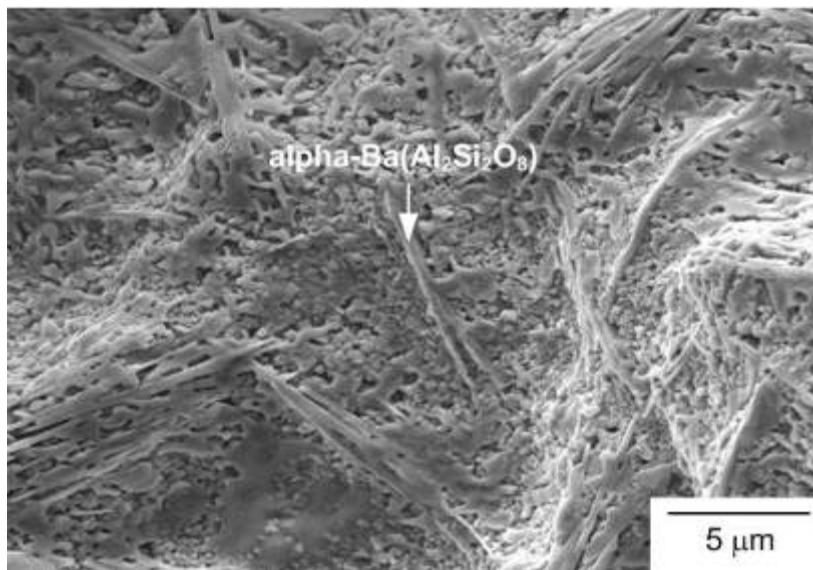
(a)
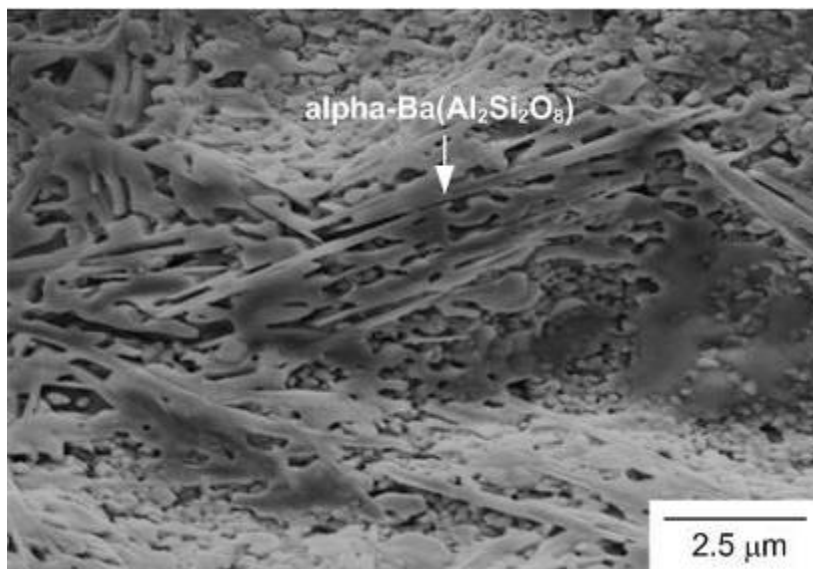


(b)

Fig. 9    Microstructure of 100 h-aged GC-9 glass-ceramic: (a) low magnification; (b) high magnification; (c) higher magnification. [12]
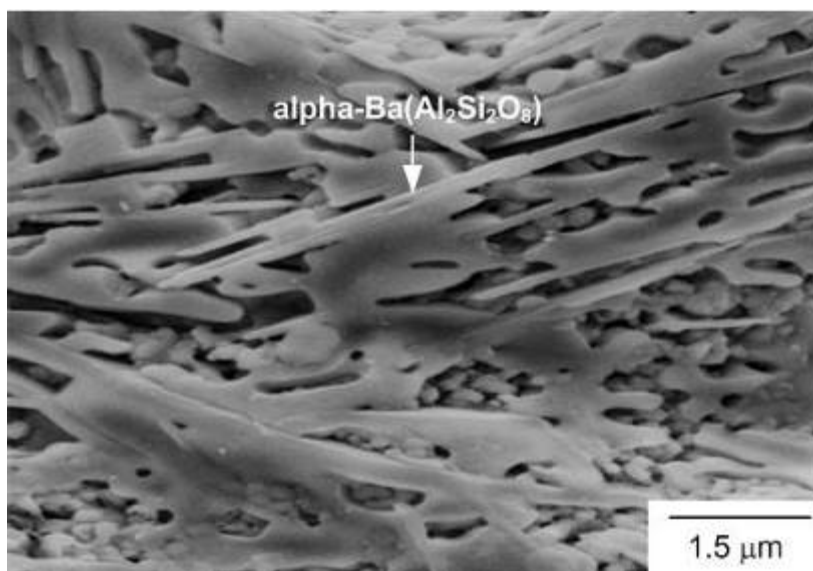
(c)

Fig. 9      (continued)
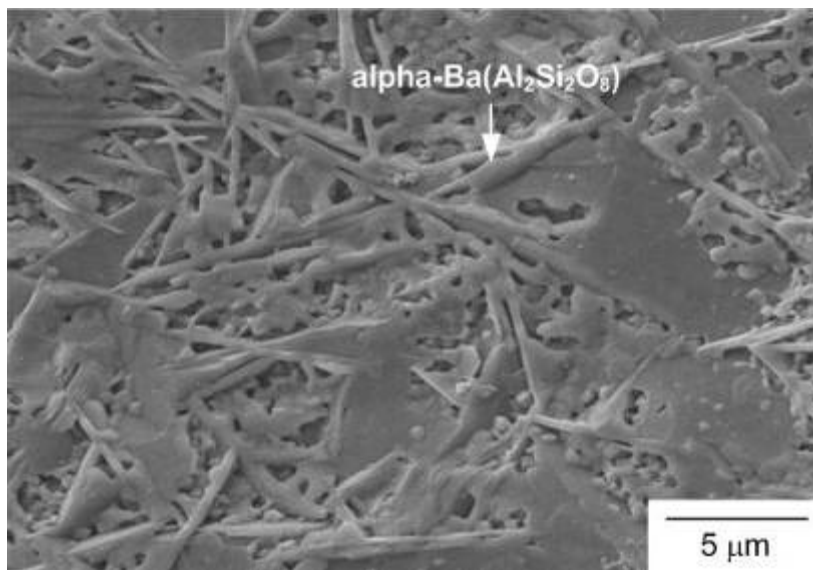
(a)
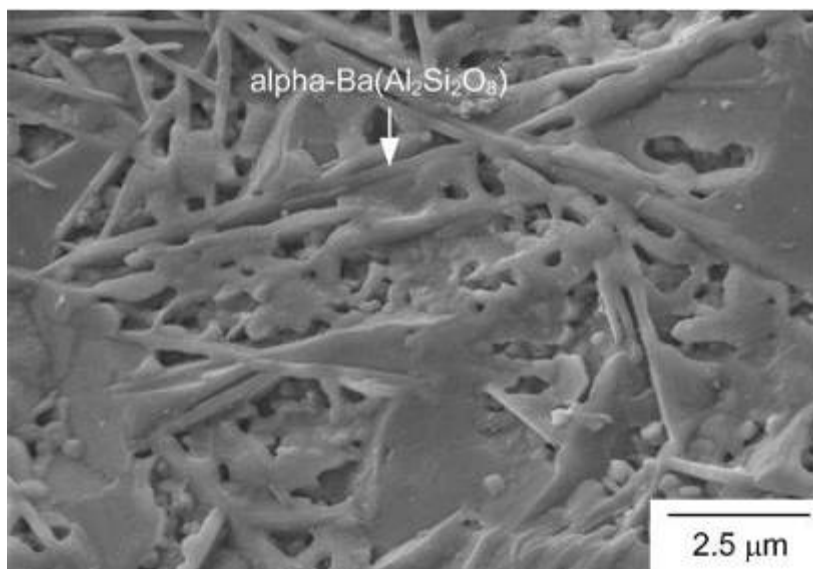


(b)

Fig. 10    Microstructure of 1000 h-aged GC-9 glass-ceramic: (a) low magnification; (b) high magnification; (c) higher magnification. [12]

alpha-Ba(Al$_2$Si$_2$O$_8$)

1.5 µm
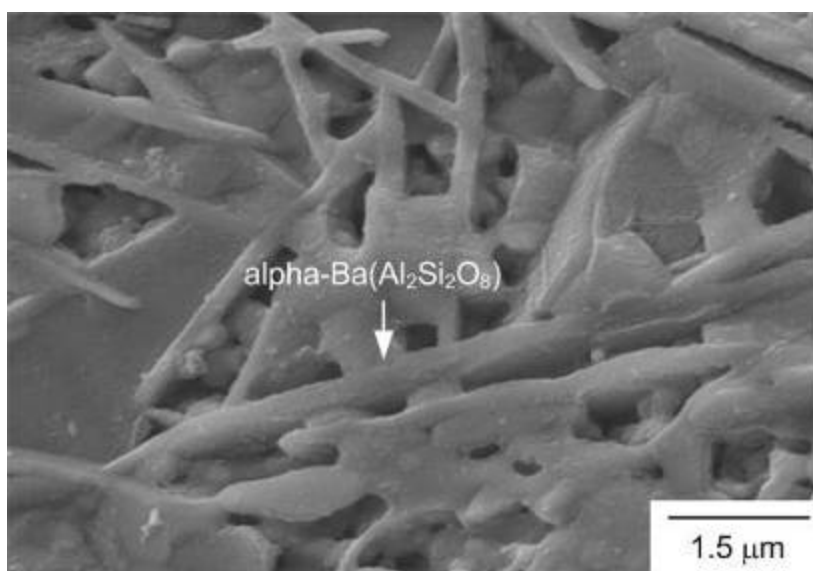
(c)
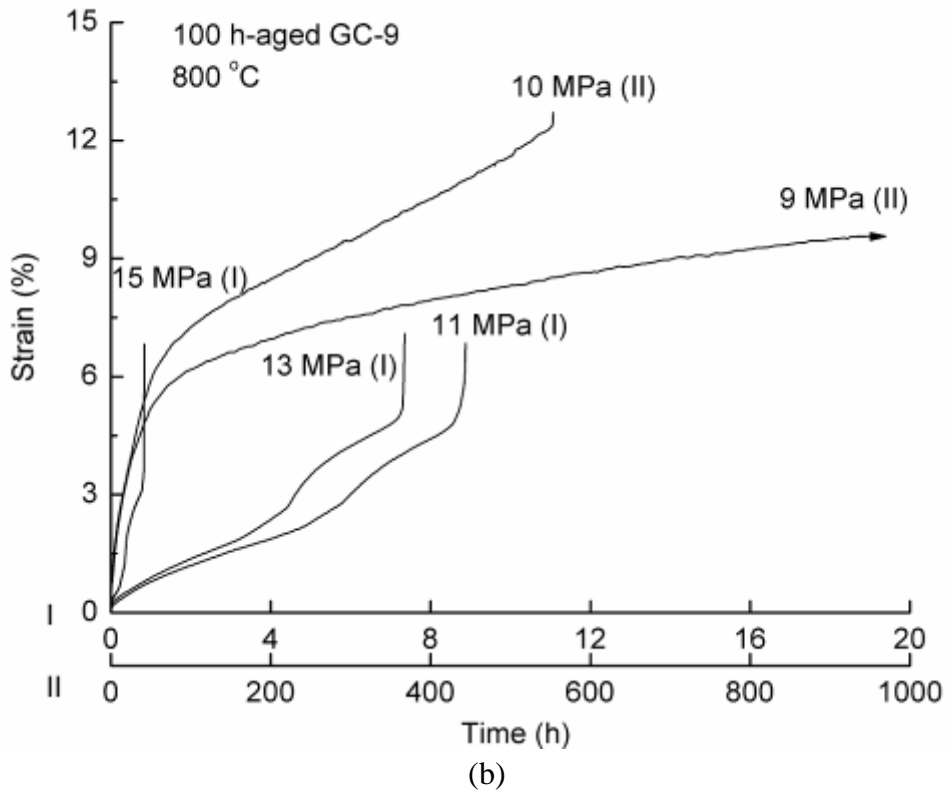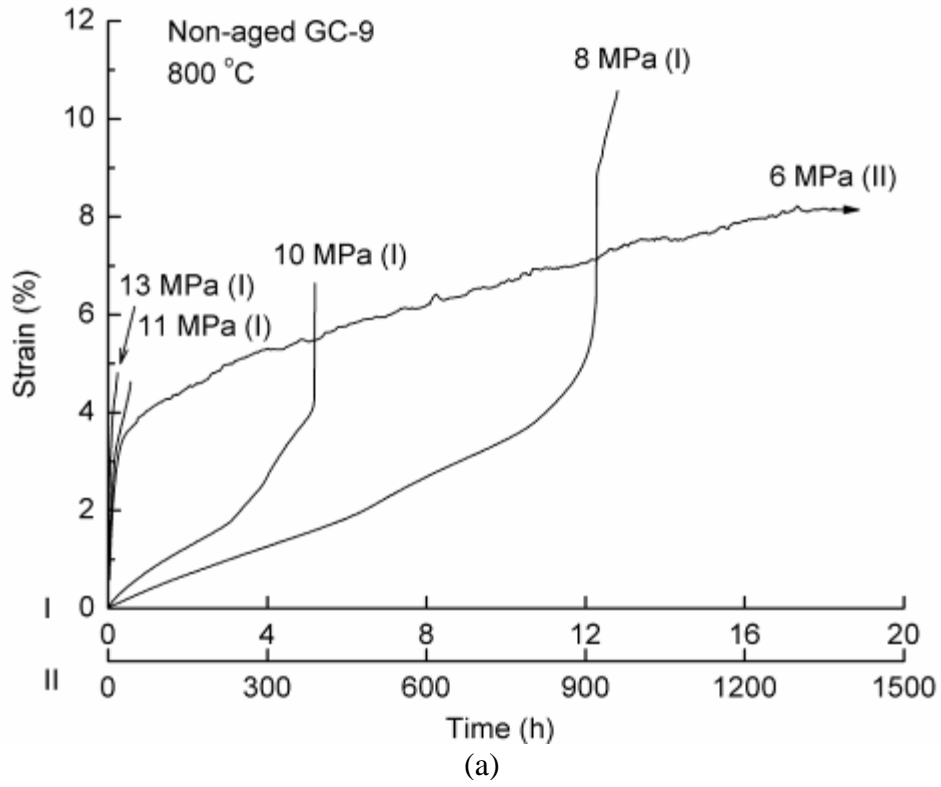
Fig. 10    (continued)

Fig. 11    Typical creep curves for variously aged GC-9 at 800 °C: (a) non-aged GC-9; (b) 100 h-aged GC-9; (c) 1000 h-aged GC-9. (Arrows indicate the specimens were not ruptured when the test was terminated.)

48
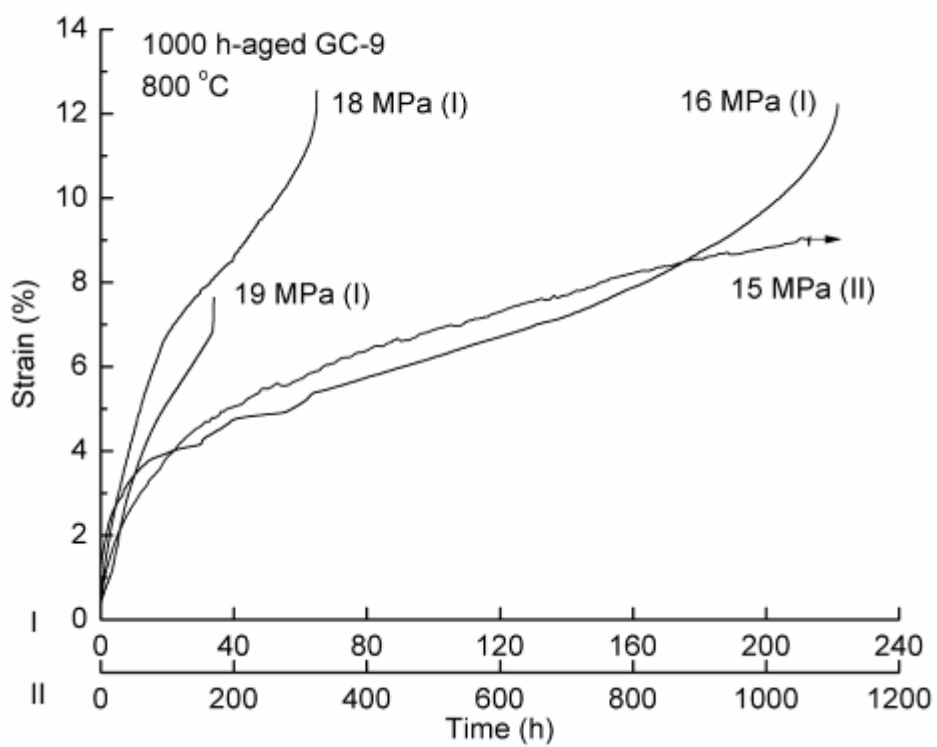
(c)

Fig. 11    (continued)
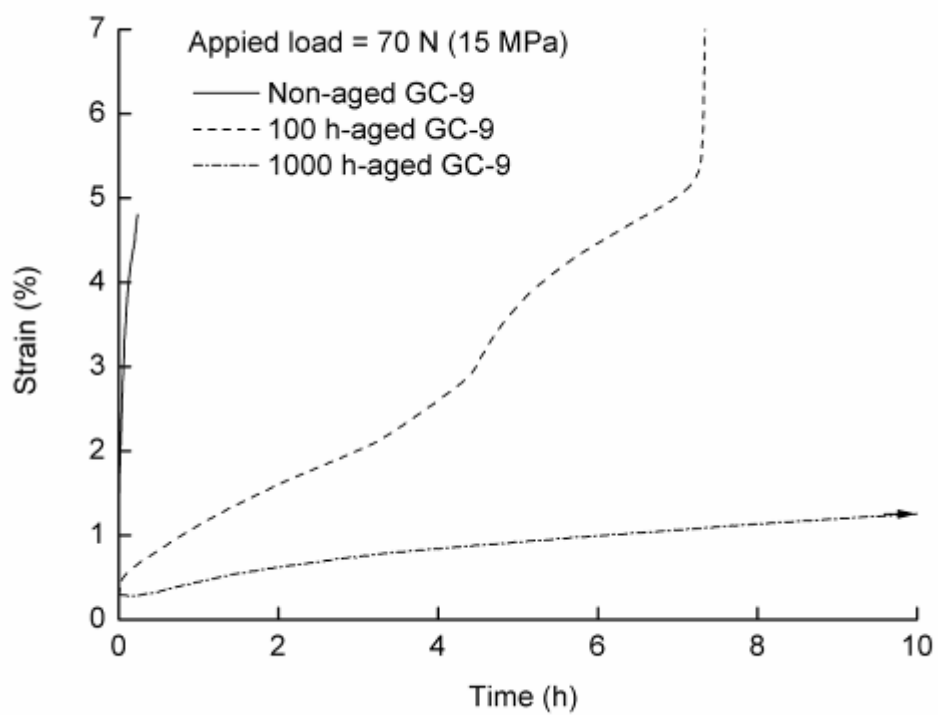
Fig. 12 Typical creep curves of variously aged GC-9 under a constant load of 70 N in the first 10 h. (The arrow indicates the specimen was not ruptured when the test was terminated.)
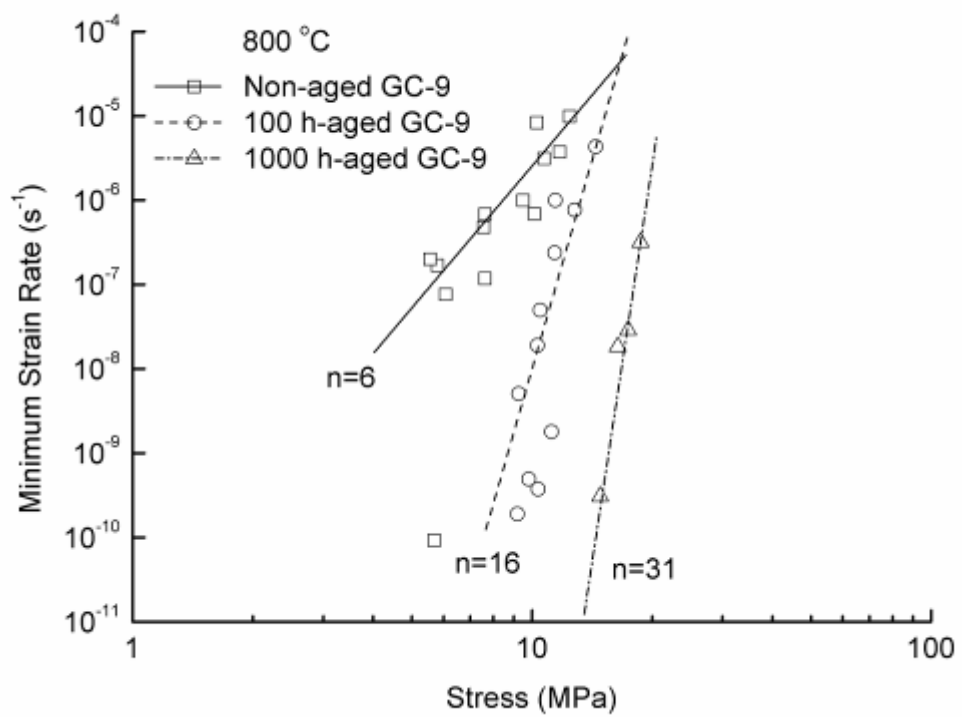
Fig. 13   Relationship between minimum creep strain rate and applied stress for variously aged GC-9 at 800 $^{\circ}$C.
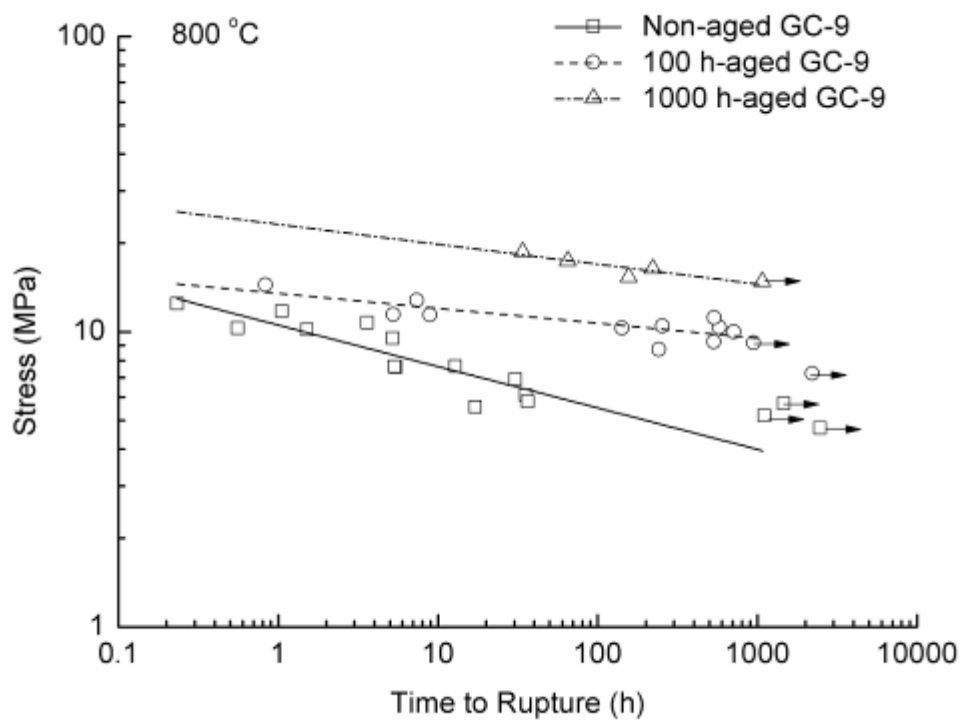
Fig. 14    Applied  stress  versus  rupture  time  for  variously  aged  GC-9  glass-ceramic.
(Arrows indicate the specimens were not ruptured when the test was terminated.)
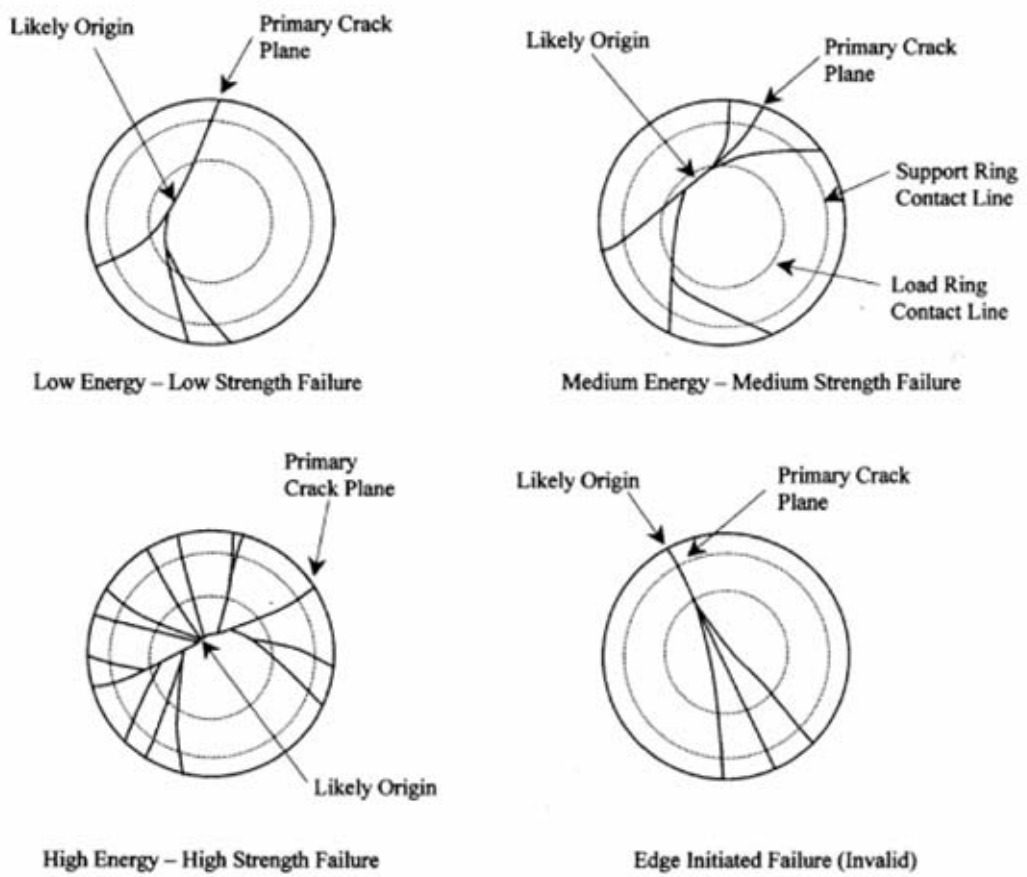
Fig. 15    Illustrations of failure patterns in concentric ring test specimens. [30]
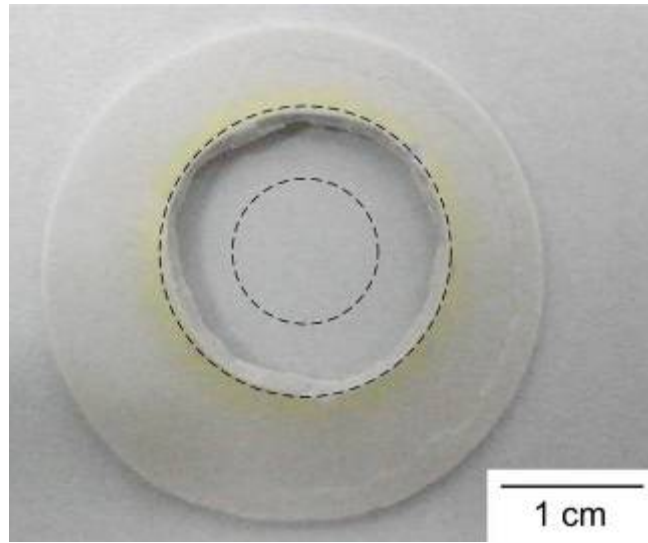
(a)
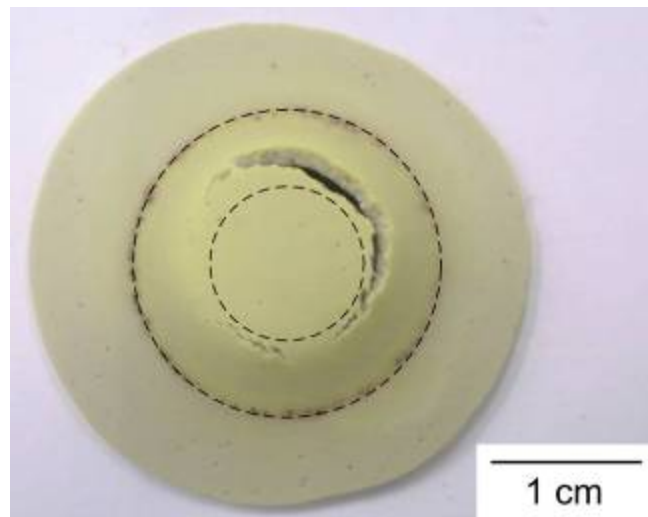


(b)

Fig. 16    Failure patterns in the ring-on-ring creep test specimens of non-aged GC-9: (a) high constant load; (b) low constant load. (The dash lines indicate the circumferences of the inner loading ring and the outer support ring.)
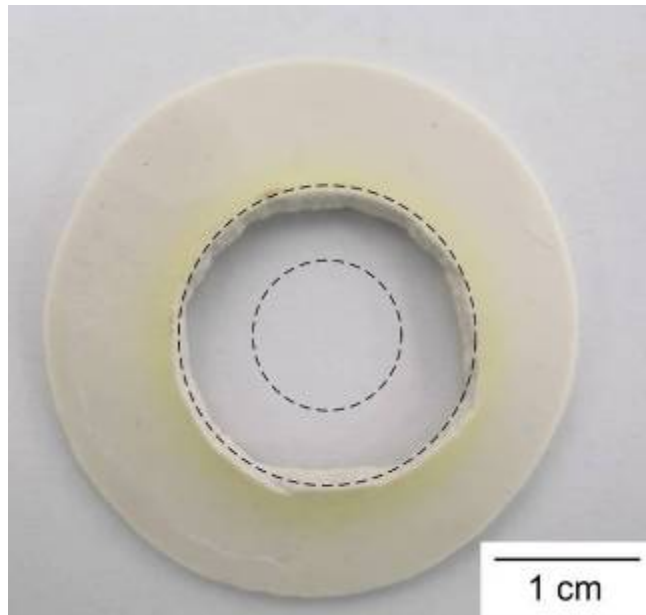
(a)
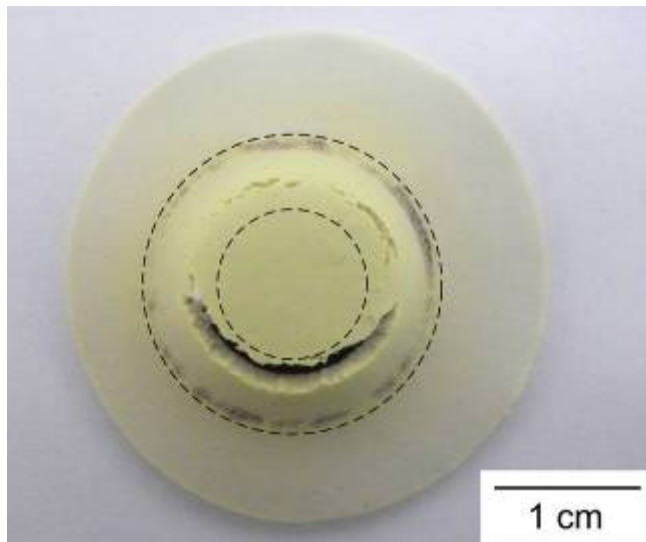


(b)

Fig. 17    Failure patterns in the ring-on-ring creep test specimens of 100 h-aged GC-9: (a) high constant load; (b) low constant load. (The dash lines indicate the circumferences of the inner loading ring and the outer support ring.)
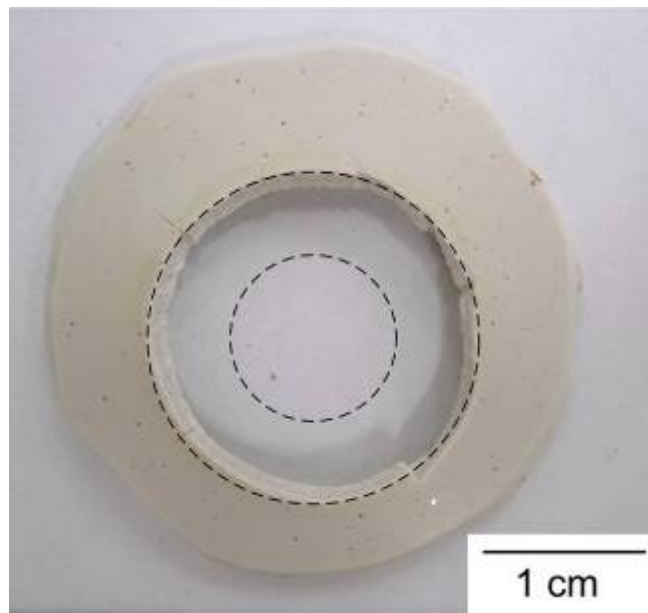
(a)
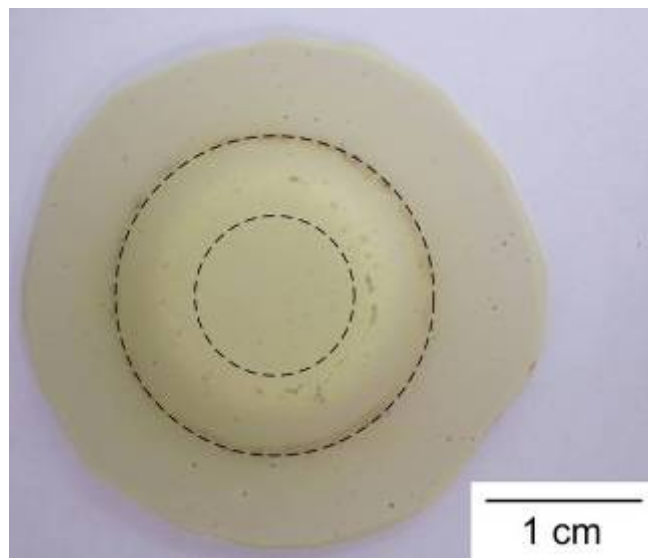


(b)

Fig. 18 Failure patterns in the ring-on-ring creep test specimens of 1000 h-aged GC-9: (a) high constant load; (b) low constant load. (The dash lines indicate the circumferences of the inner loading ring and the outer support ring.)

**Tension**

250 μm

(a)

**Tension**

250 μm
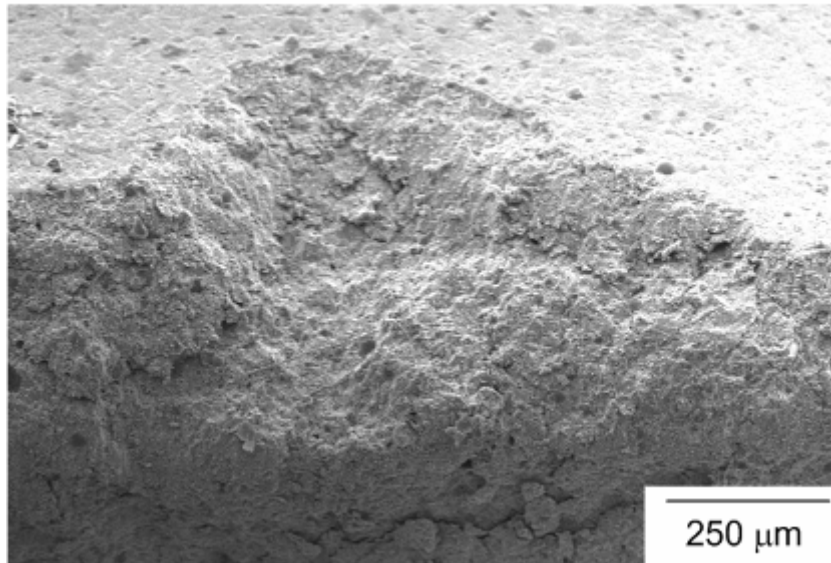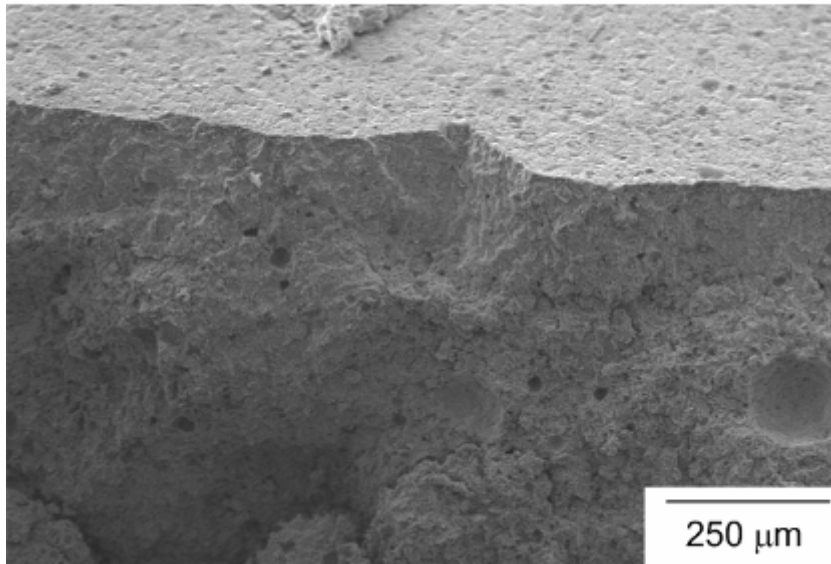
(b)

Fig. 19  Failure origins of variously aged GC-9 specimens: (a)-(b) non-aged GC-9; (c)-(d)
100 h-aged GC-9; (e)-(f) 1000 h-aged GC-9.

**Tension**



500 μm

(c)

**Tension**



100 μm

(d)

Fig. 19    (continued)

58

**Tension**

250 µm

(e)



**Tension**

100 µm

(f)
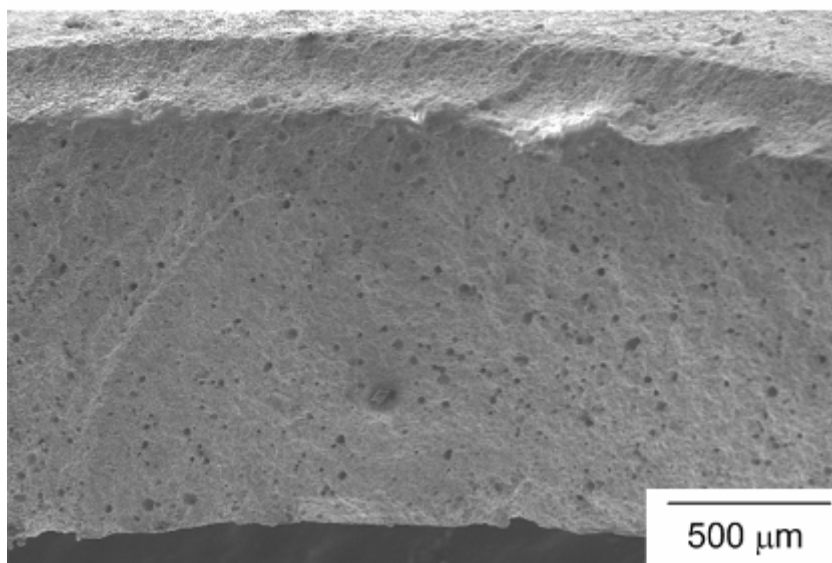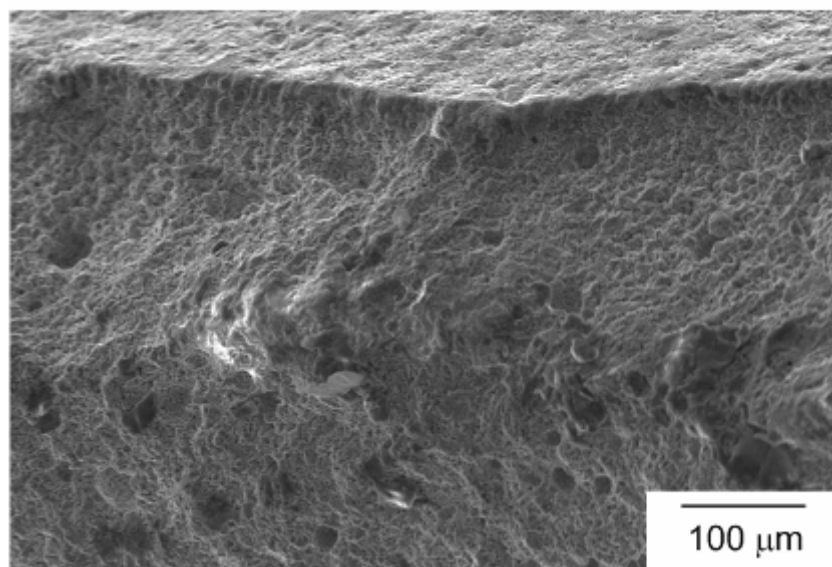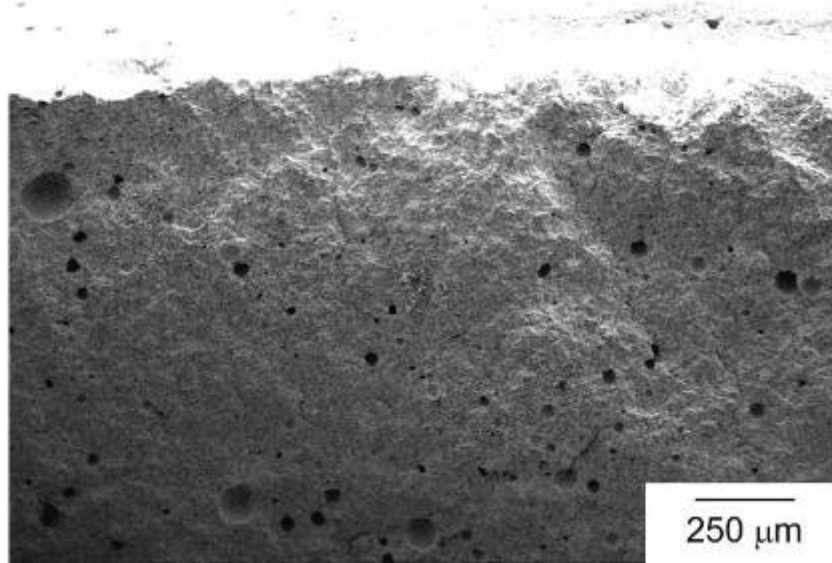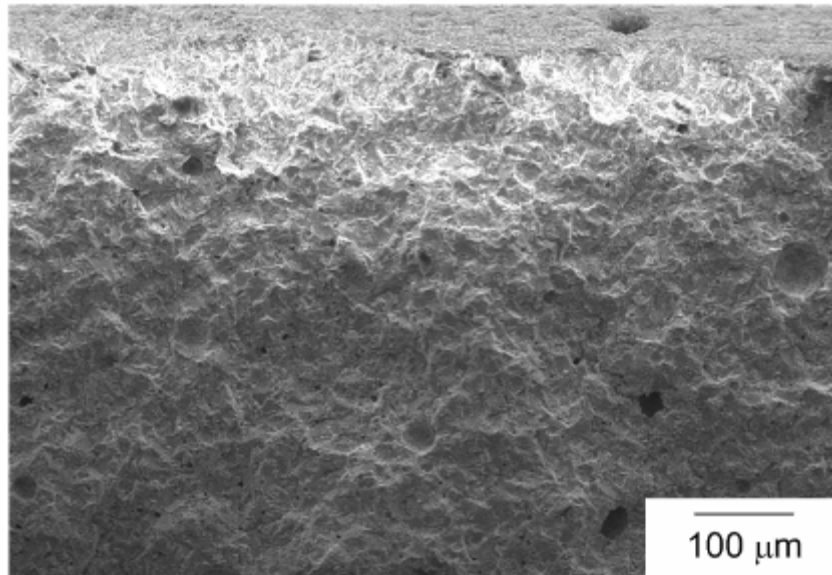
Fig. 19    (continued)
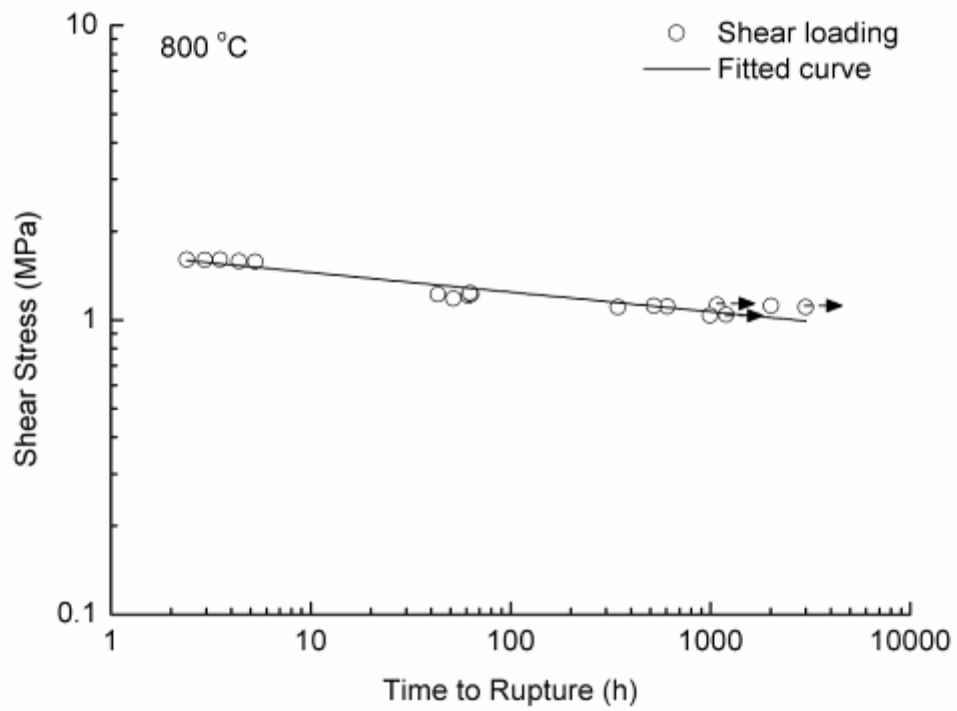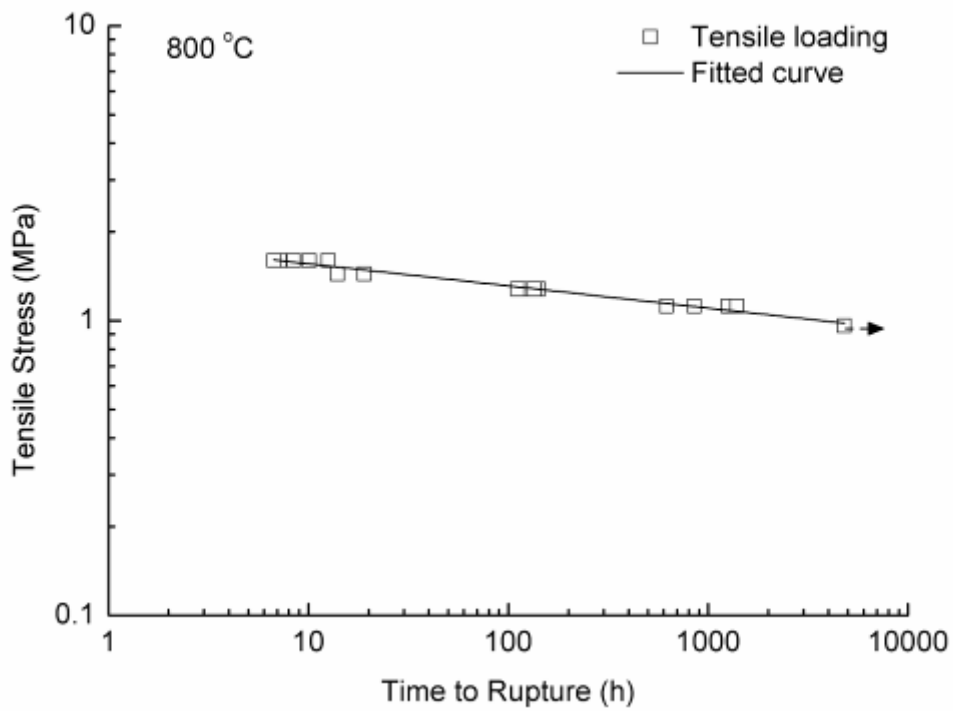
Fig. 20    Applied stress versus rupture time for the joint specimens subjected to constant (a) shear and (b) tensile loading. (Arrows indicate the specimens were not ruptured when the test was terminated.)
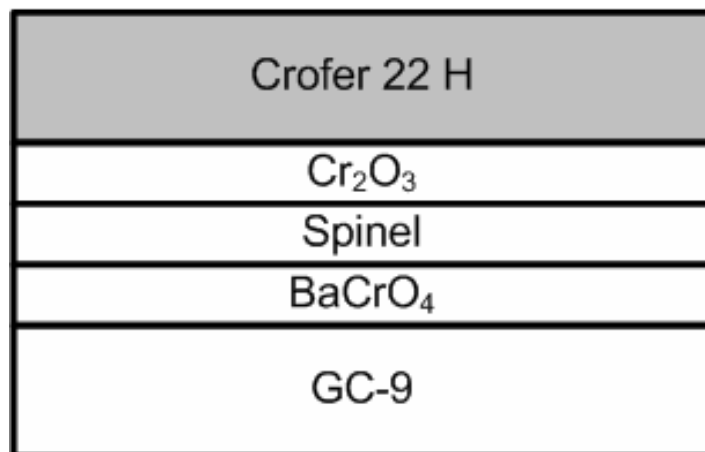
Fig. 21    Schematic of oxide layers between Crofer 22 H and GC-9 glass-ceramic.
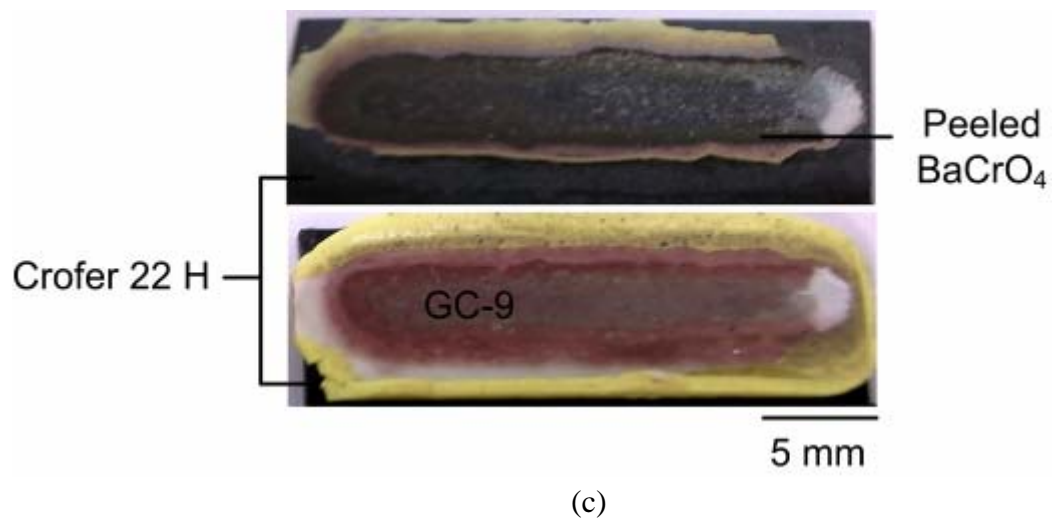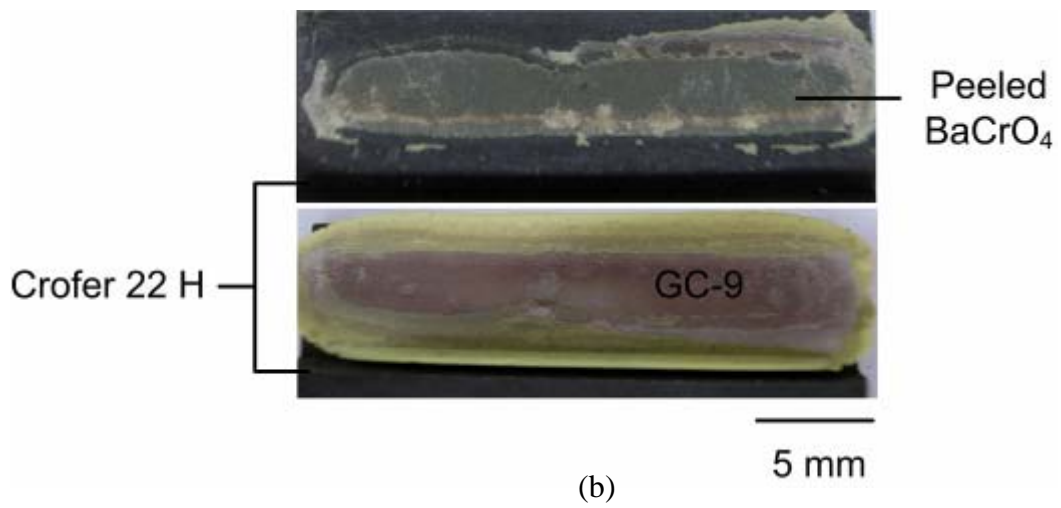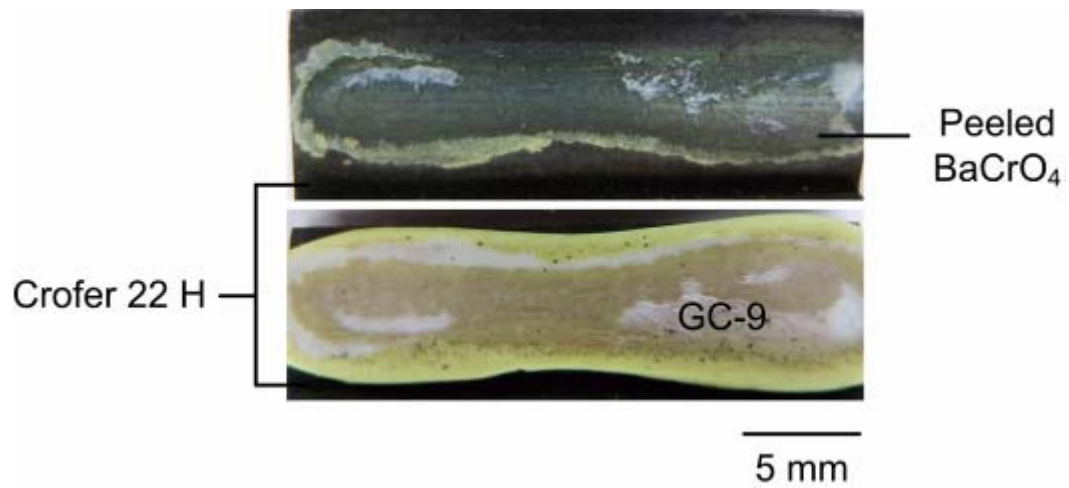
Fig. 22    Failure patterns in the shear specimens tested at 800 °C: (a) short creep rupture time; (b) medium-term creep rupture time; (c) long creep rupture time.

(a)



5 μm
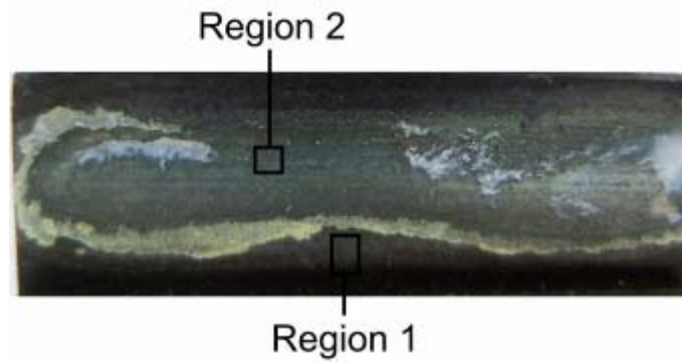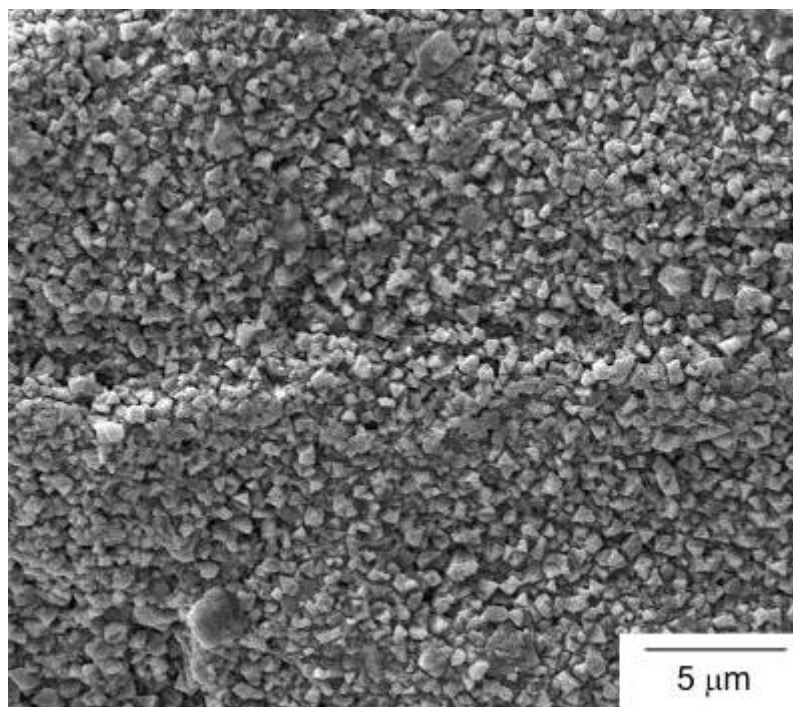
(b)

Fig. 23　A fracture surface region of the shear specimen shown in the upper part of Fig. 21(a): (a) optical micrograph showing the observed regions of SEM; (b) SEM micrograph of region 1; (c) SEM micrograph of region 2.
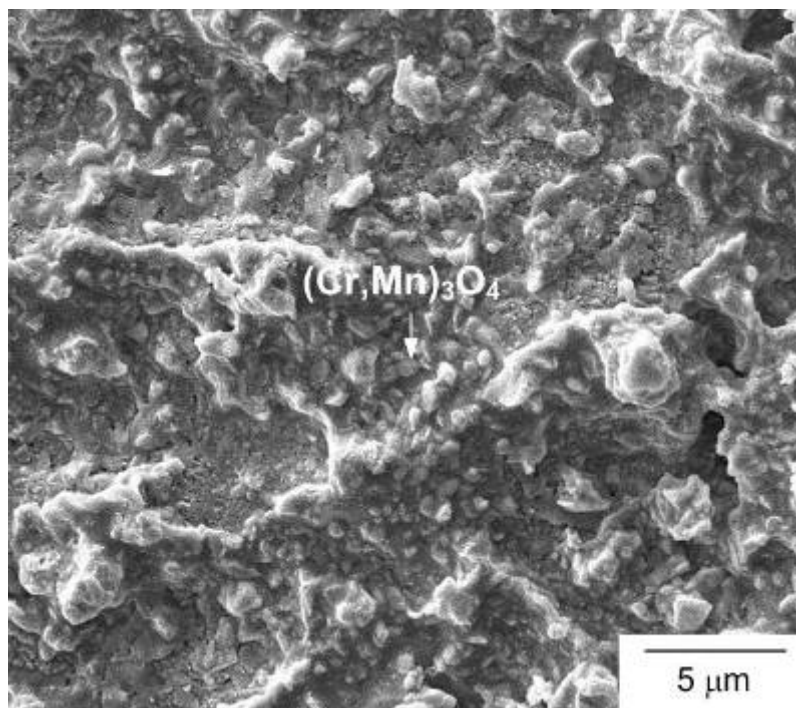
(c)

Fig. 23    (continued)

(a)



5 μm
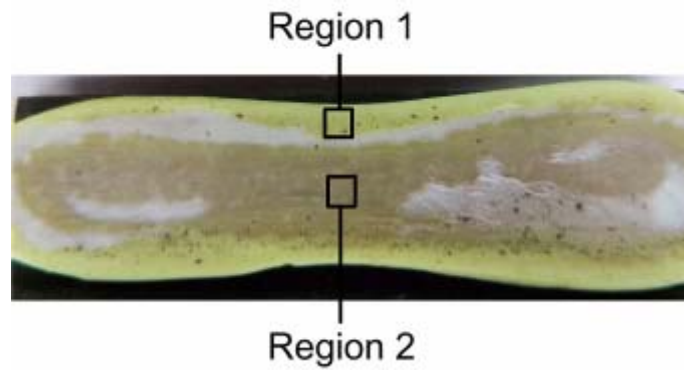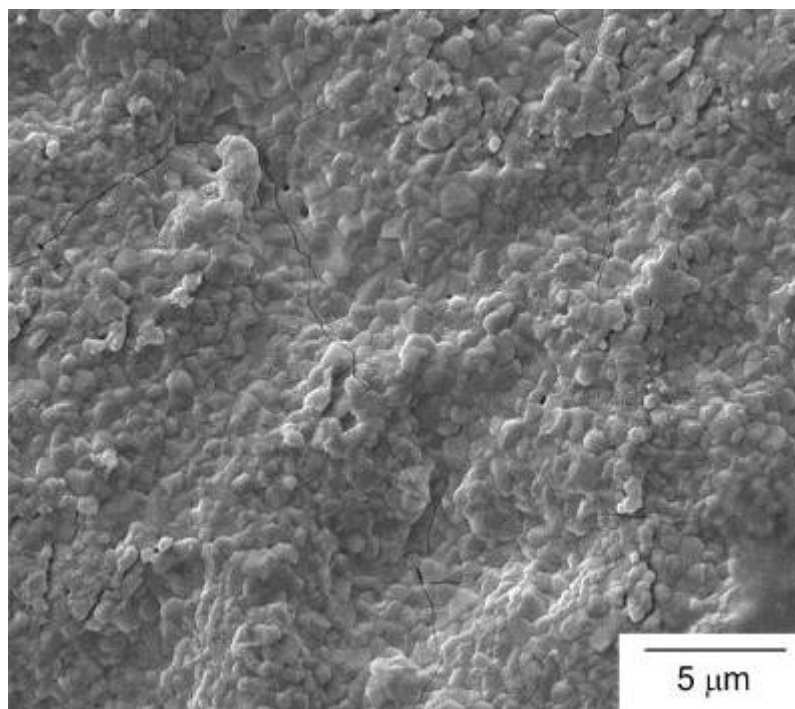
(b)

Fig. 24　A fracture surface region of the shear specimen shown in the lower part of Fig. 21(a): (a) optical micrograph showing the observed regions of SEM; (b) SEM micrograph of region 1; (c) SEM micrograph of region 2.
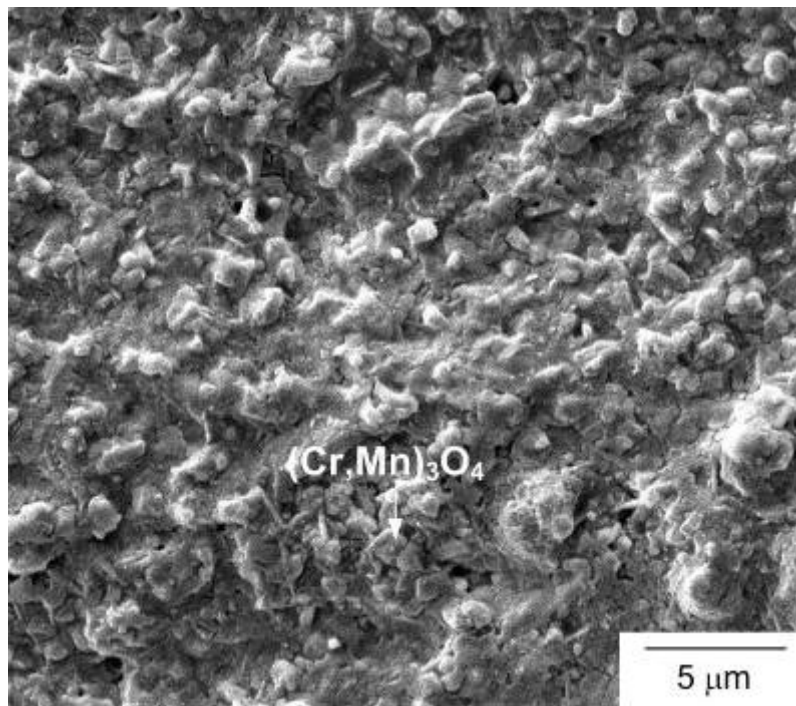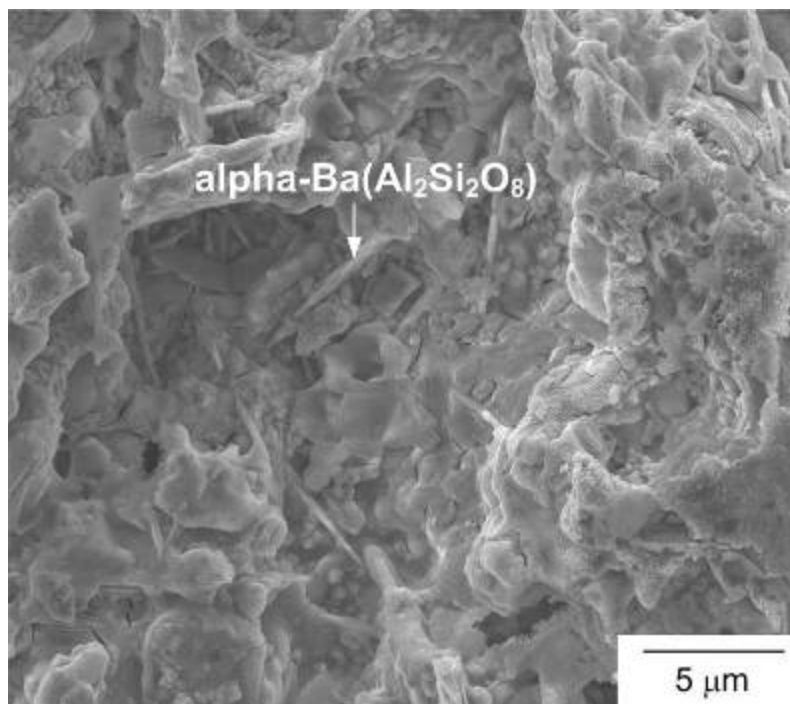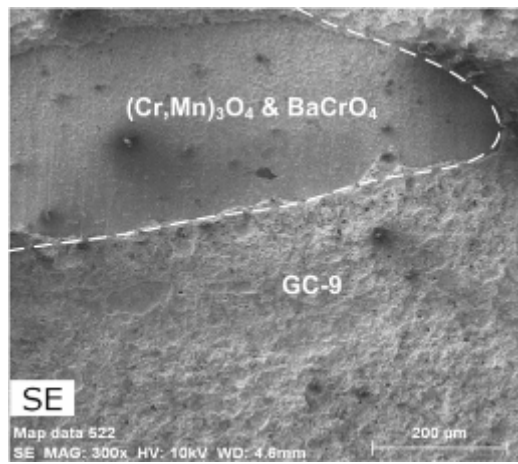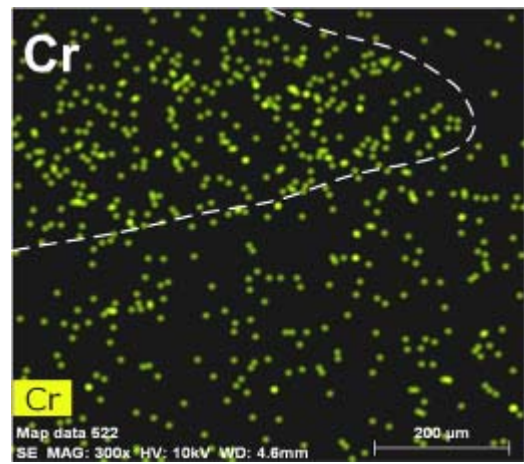
(c)

Fig. 24    (continued)
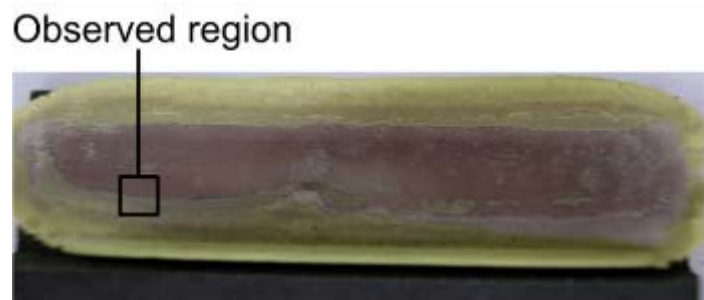
(a)
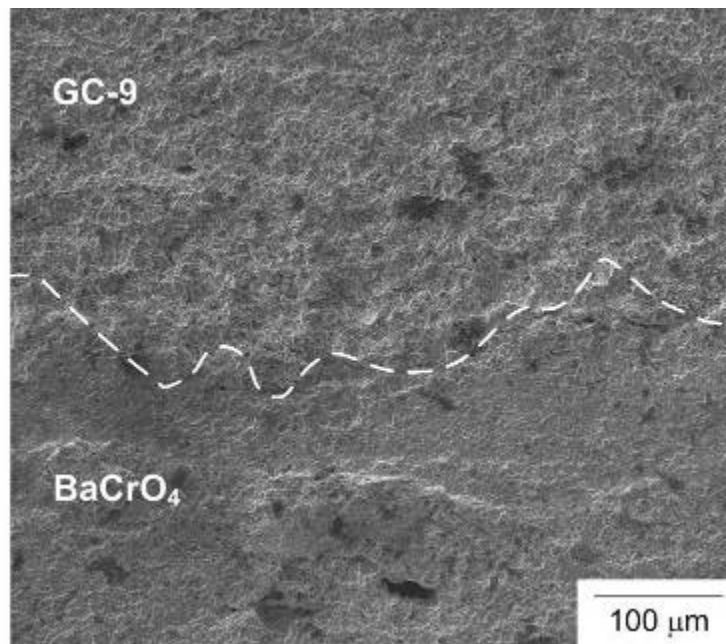


(b)

Fig. 25    A fracture surface region of the shear specimen shown in Fig. 21(b): (a) optical micrograph showing the observed region of SEM; (b) SEM micrograph of the outlined region.
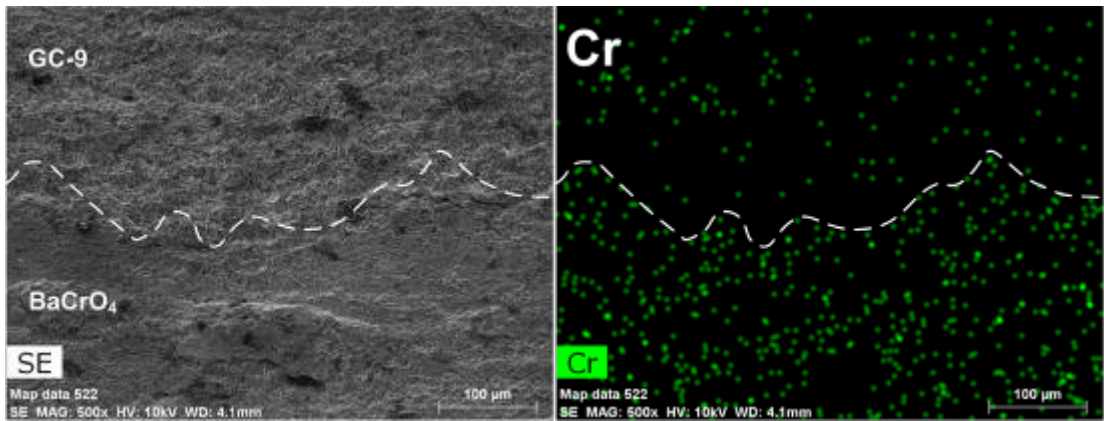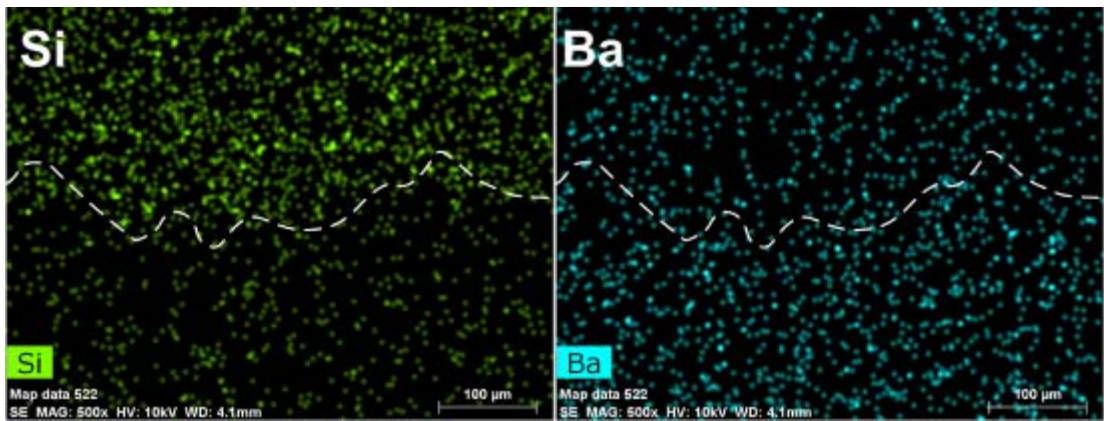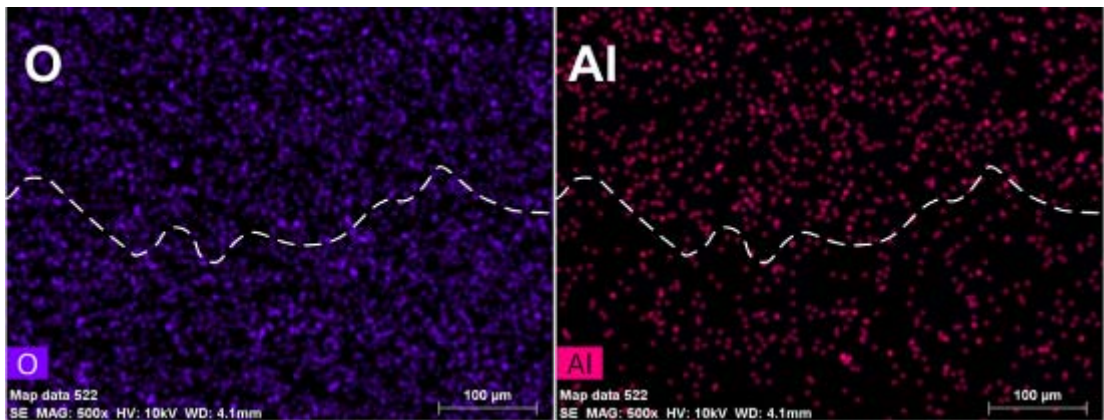
Fig. 26   EDS mapping of elements on the outlined fracture surface region of the shear
specimen shown in Fig. 24(b): (a) mapping region; (b) Cr; (c) Si; (d) Ba; (e) O;
(f) Al.
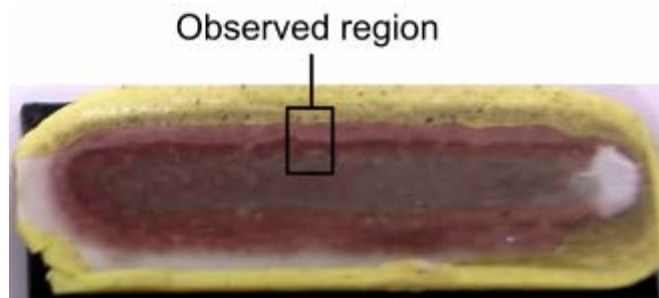
(a)
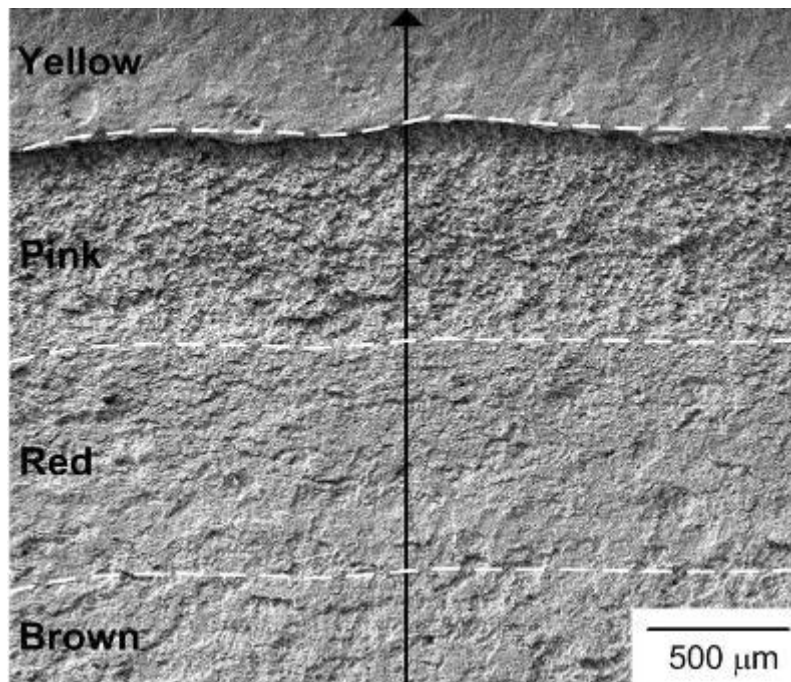


(b)

Fig. 27　A fracture surface region of the shear specimen shown in Fig. 21(c): (a) optical micrograph showing the observed region of SEM; (b) SEM micrograph of the outlined region. (The arrow indicates the direction of linescan analysis.)
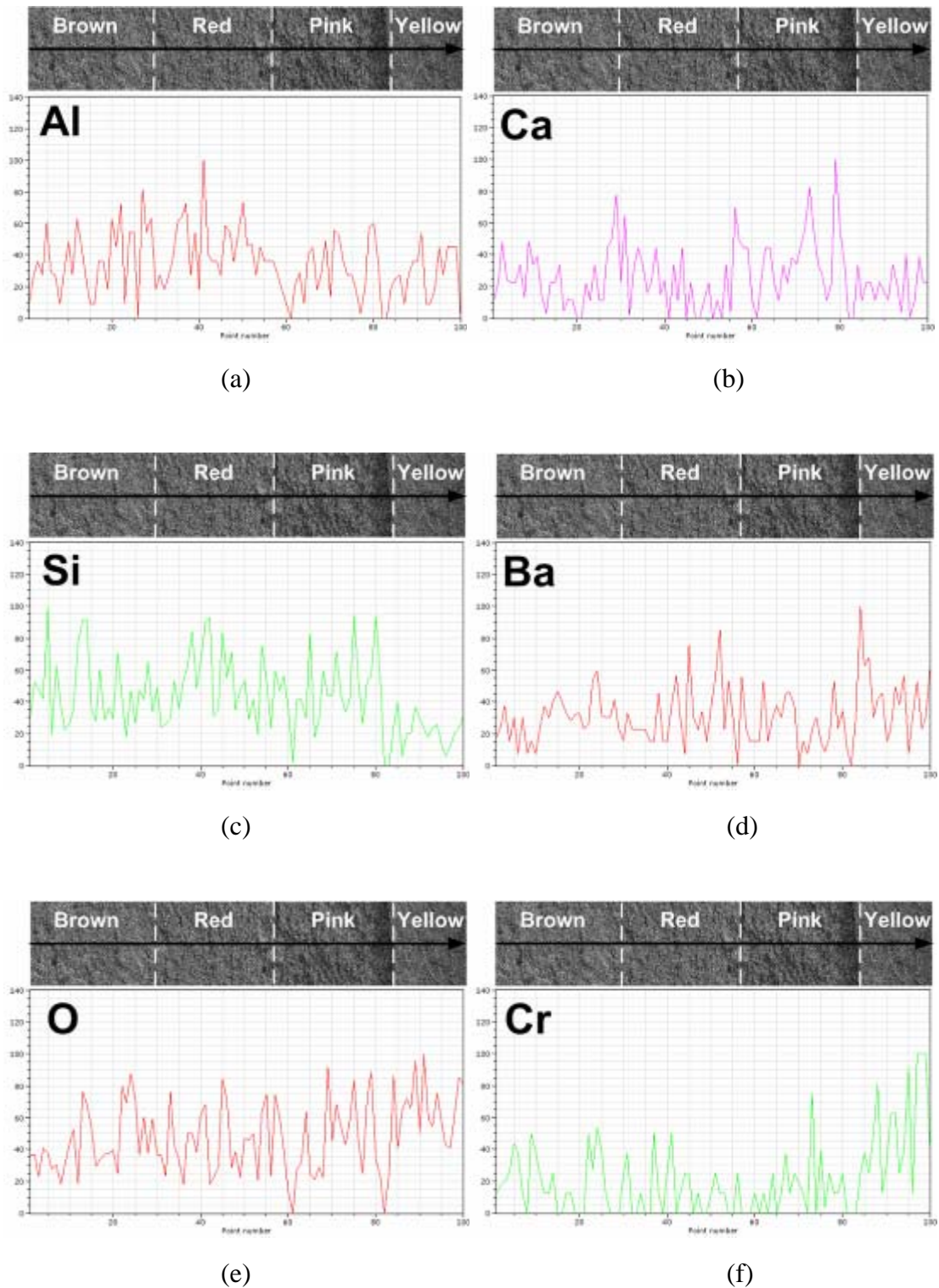
Fig. 28　Linescan analysis of element distribution in Fig. 26(b): (a) Al; (b) Ca; (c) Si; (d) Ba; (e) O; (f) Cr. (The direction of the arrow in the SEM micrograph is the same as that in Fig. 26(b).)
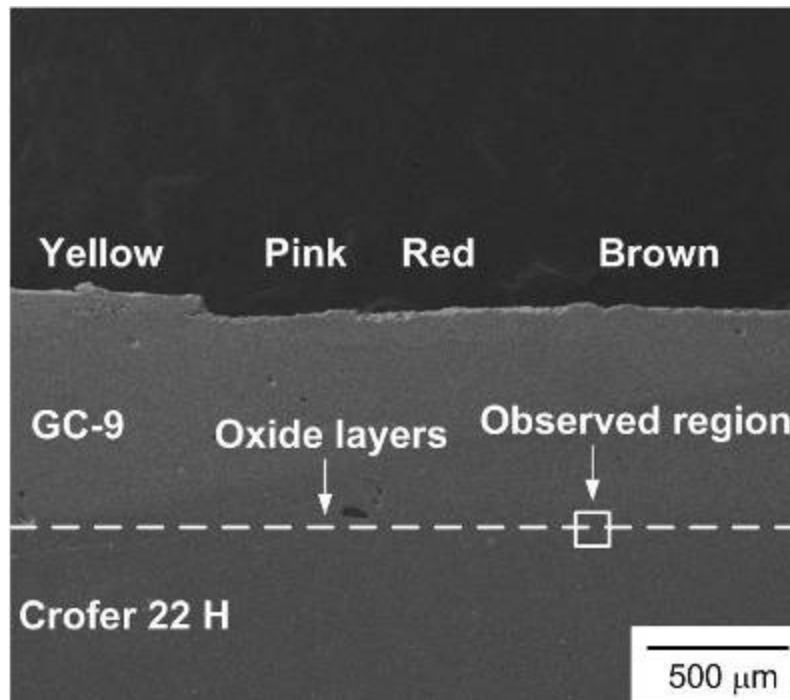
(a)
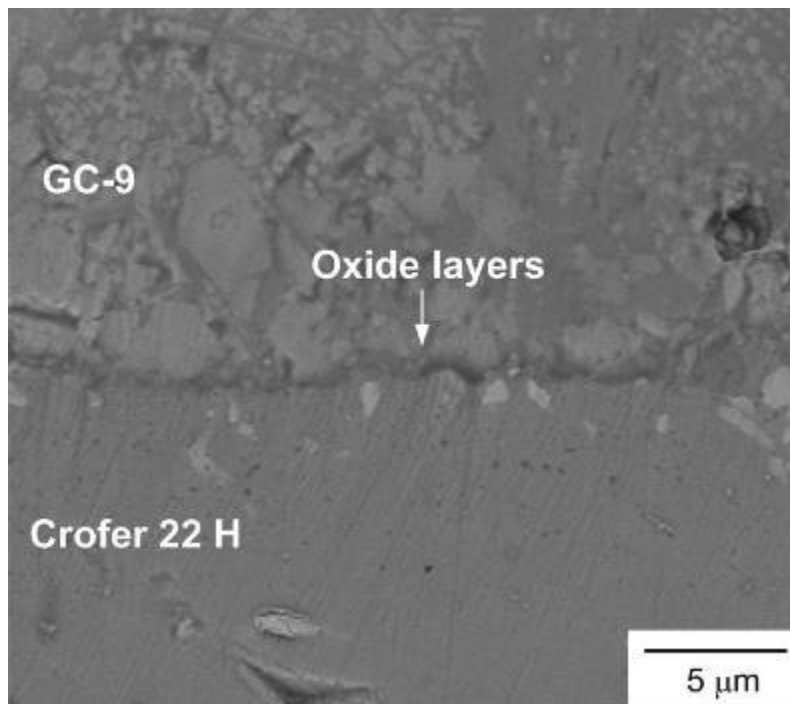


(b)

Fig. 29    SEM micrographs of the cross section of the outlined region in Fig. 26(a): (a) full region in SE mode; (b) outlined region of (a) in BSE mode.
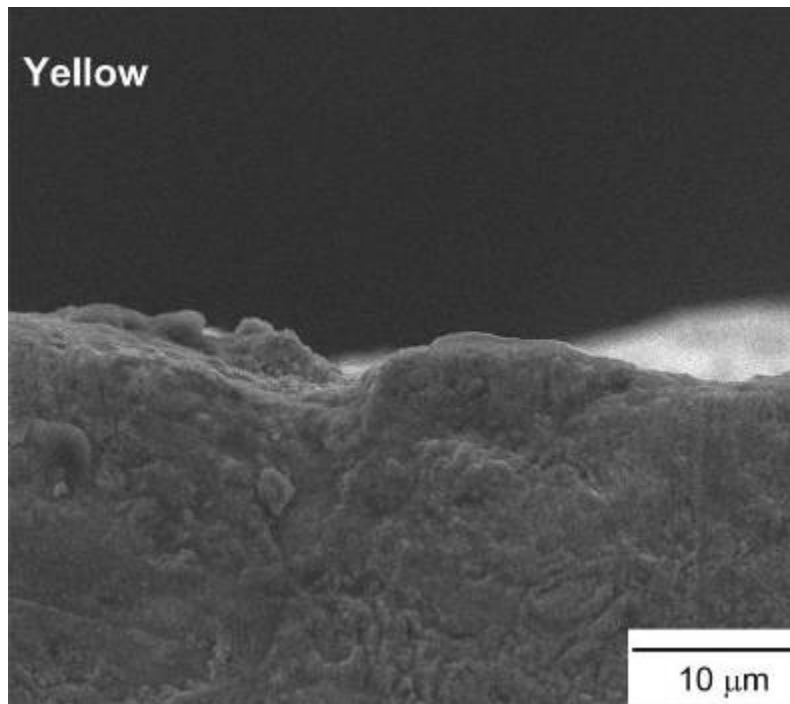
(a)
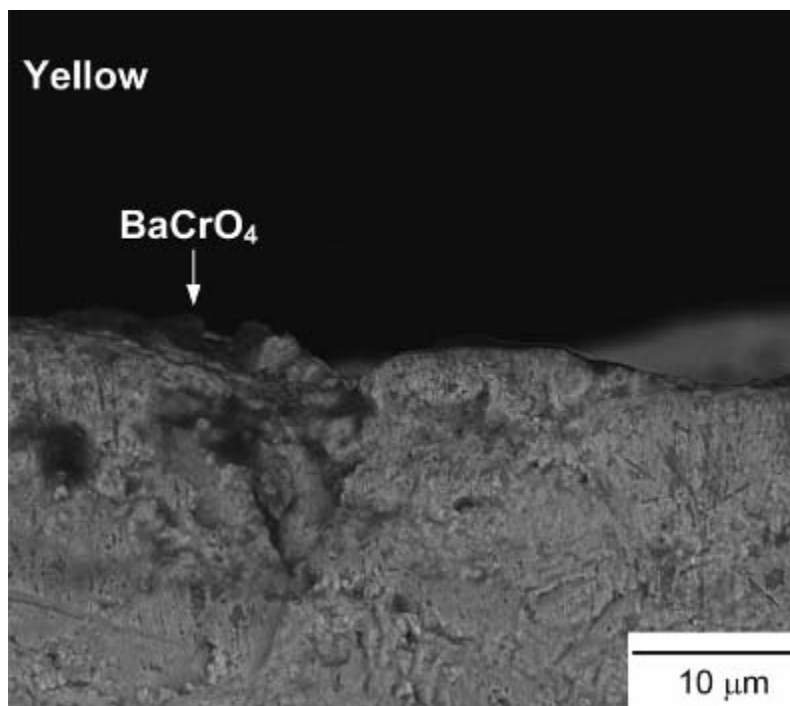


(b)

Fig. 30    SEM micrographs of various color regions in Fig. 28(a): (a) yellow region in SE mode; (b) yellow region in BSE mode; (c) pink region in SE mode; (d) pink region in BSE mode; (e) red region in SE mode; (f) red region in BSE mode; (g) brown region in SE mode; (h) brown region in BSE mode.
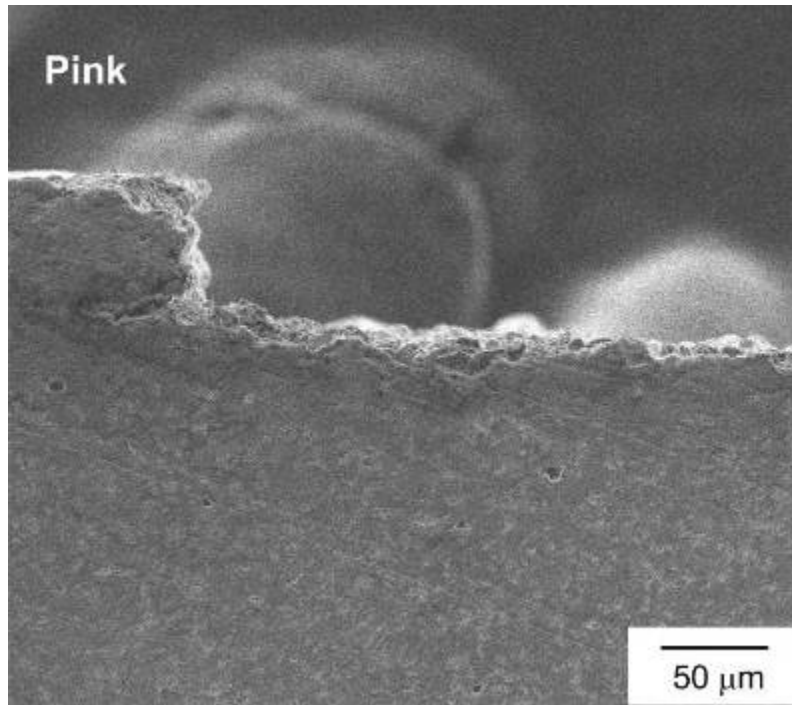
(c)
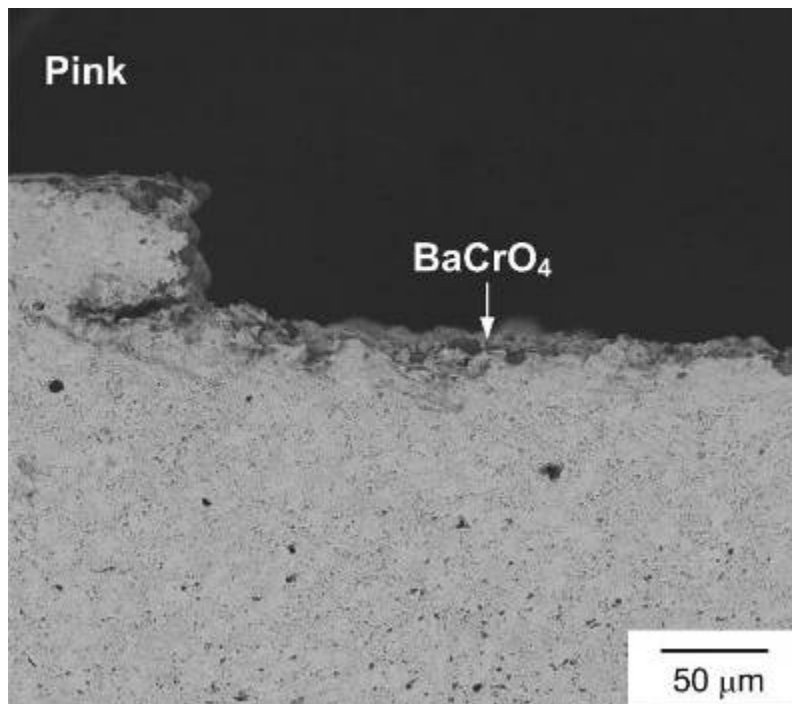


(d)

Fig. 30    (continued)
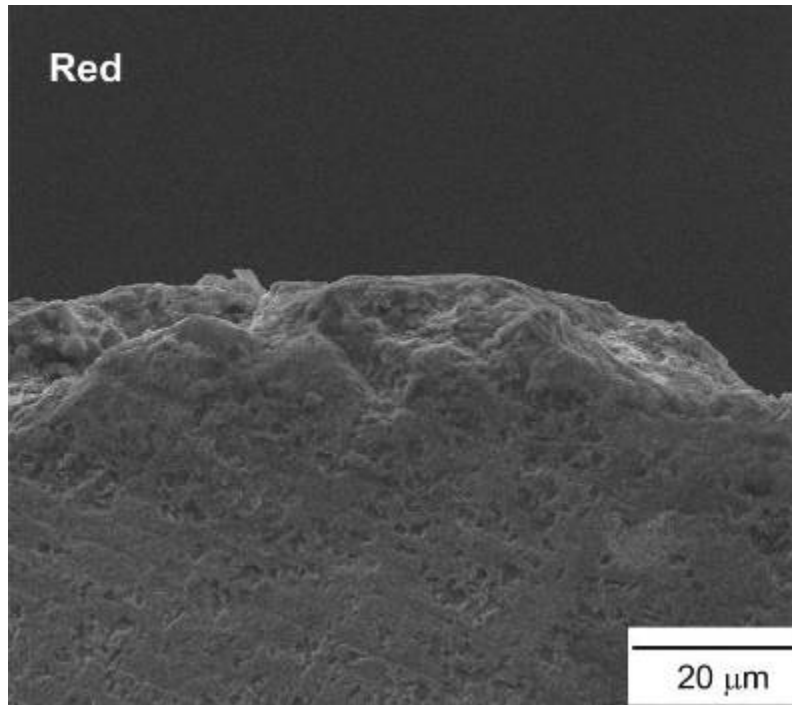
(e)
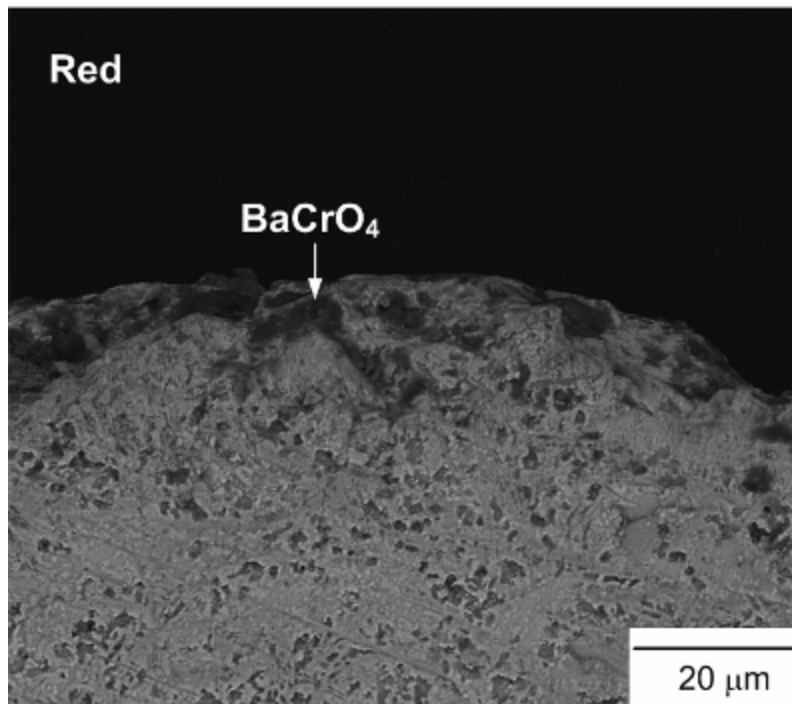


(f)

Fig. 30 (continued)
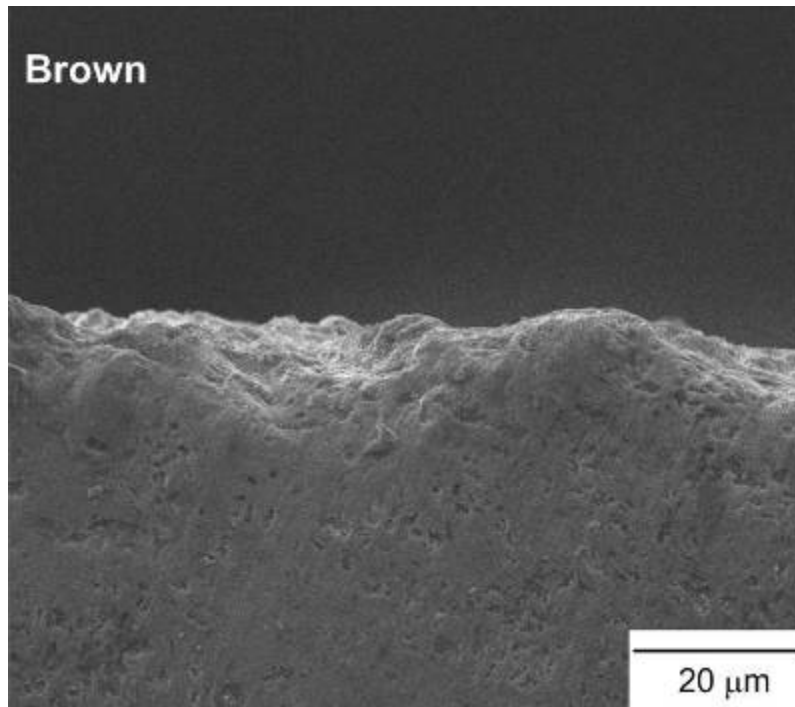
(g)
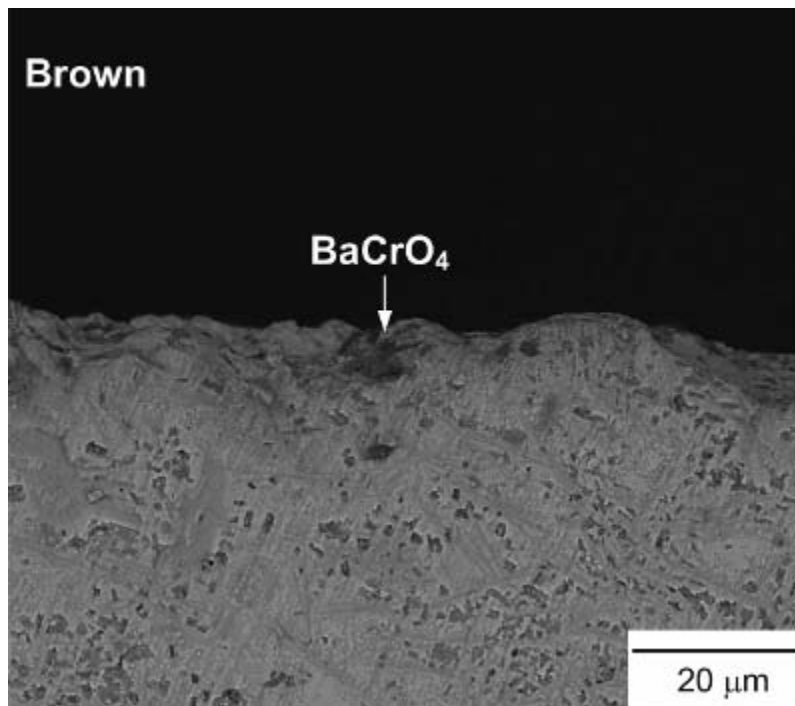


(h)

Fig. 30    (continued)
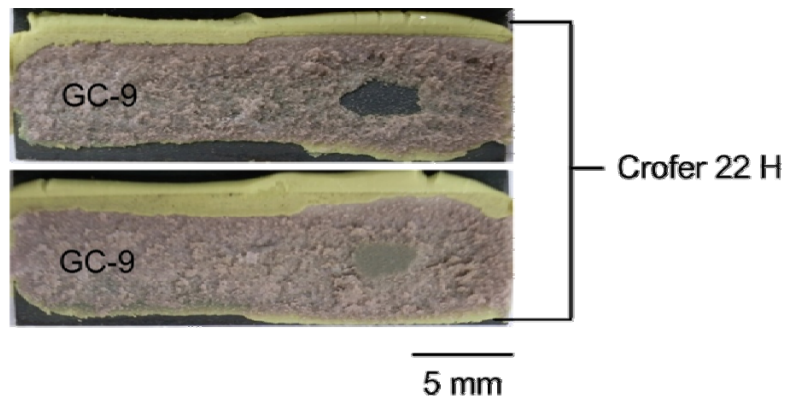
(a)
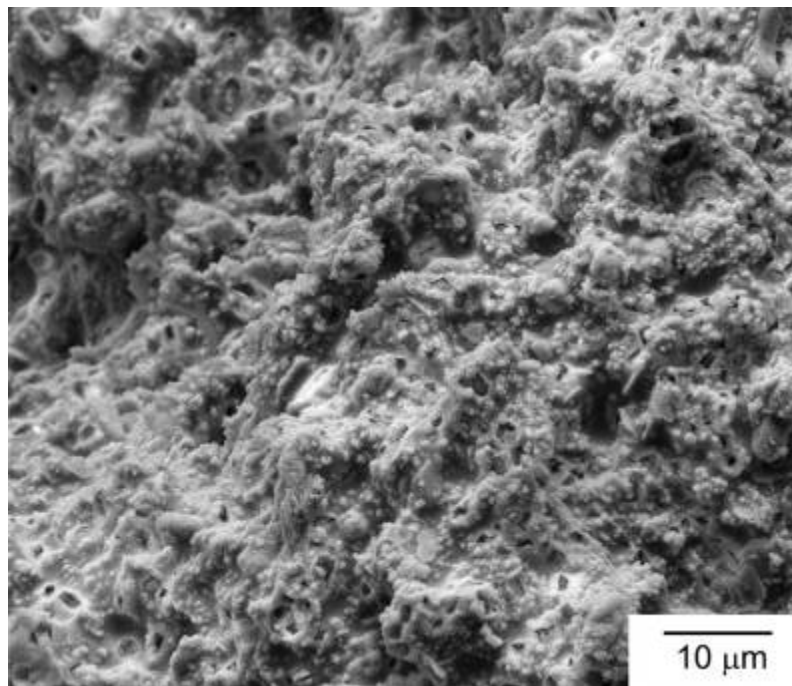


(b)

Fig. 31   (a) Failure pattern of a 1000-h pre-aged specimen after a shear strength test at 800 $^{o}$C; (b) SEM micrograph of fracture surface on the brown glass-ceramic region. [33]

(a)



alpha-Ba(Al$_2$Si$_2$O$_8$)
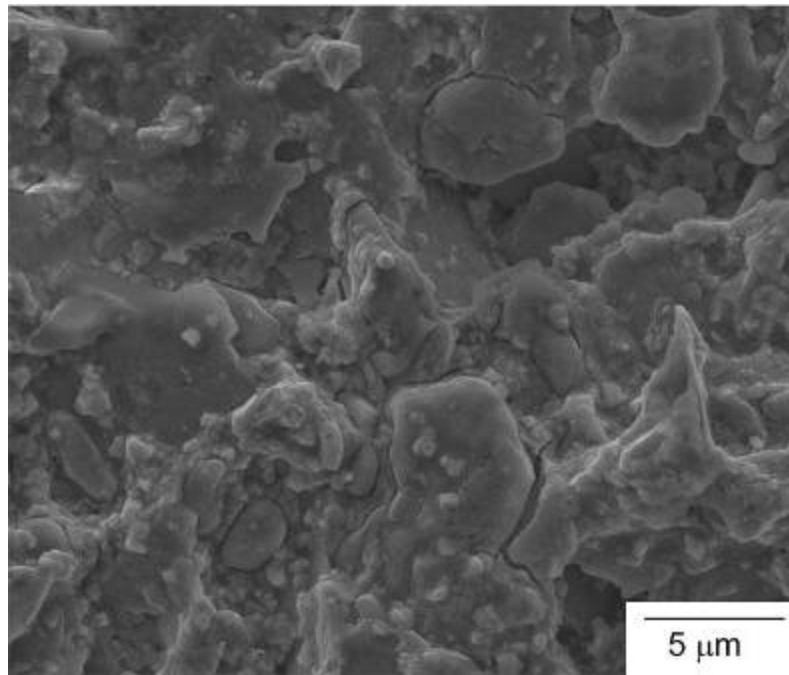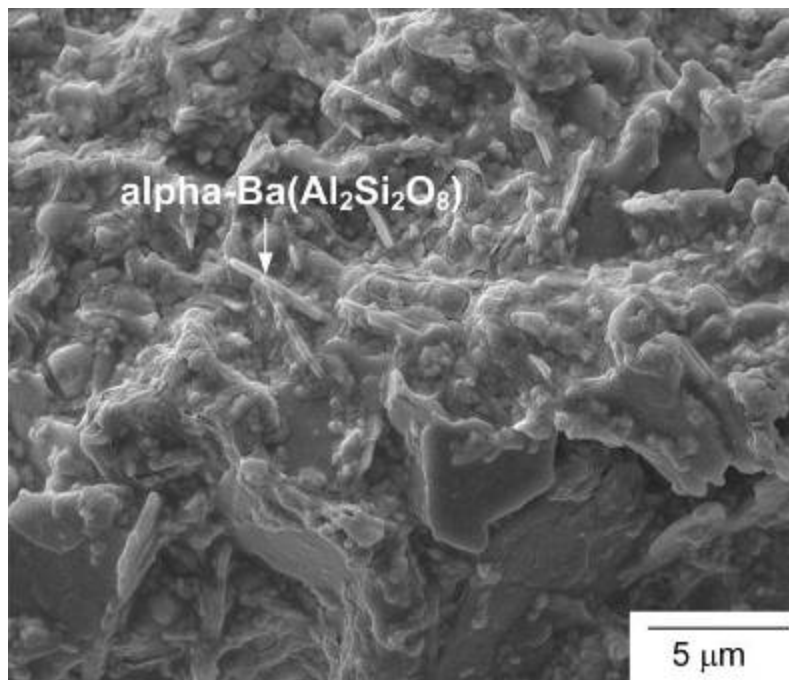
(b)

Fig. 32  Comparison of the microstructure of GC-9 glass-ceramic substrate with residual chromate layer in Fig. 21(b) and (c): (a) pink region in the lower part of Fig. 21(b); (b) brown region in the lower part of Fig. 21(c).
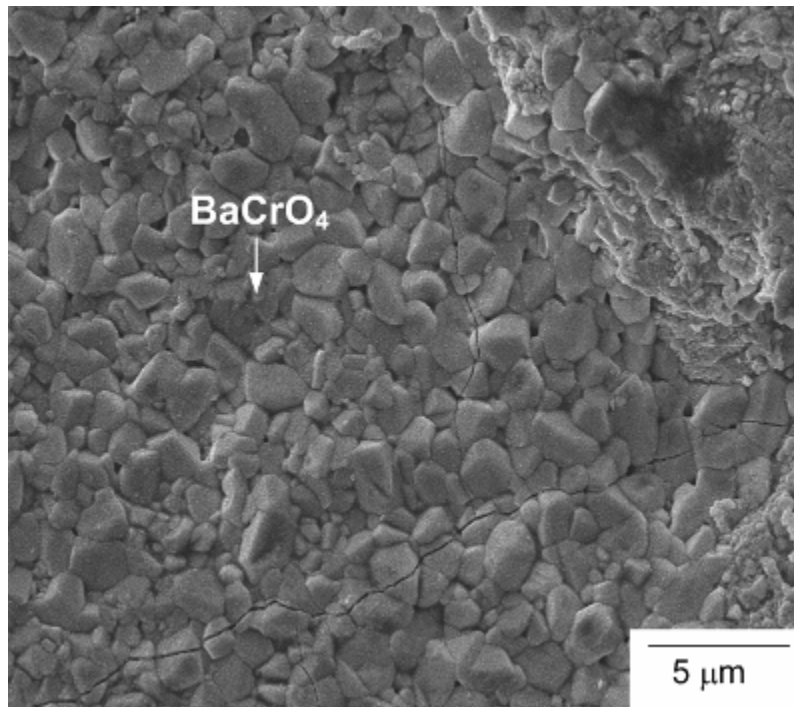
(a)
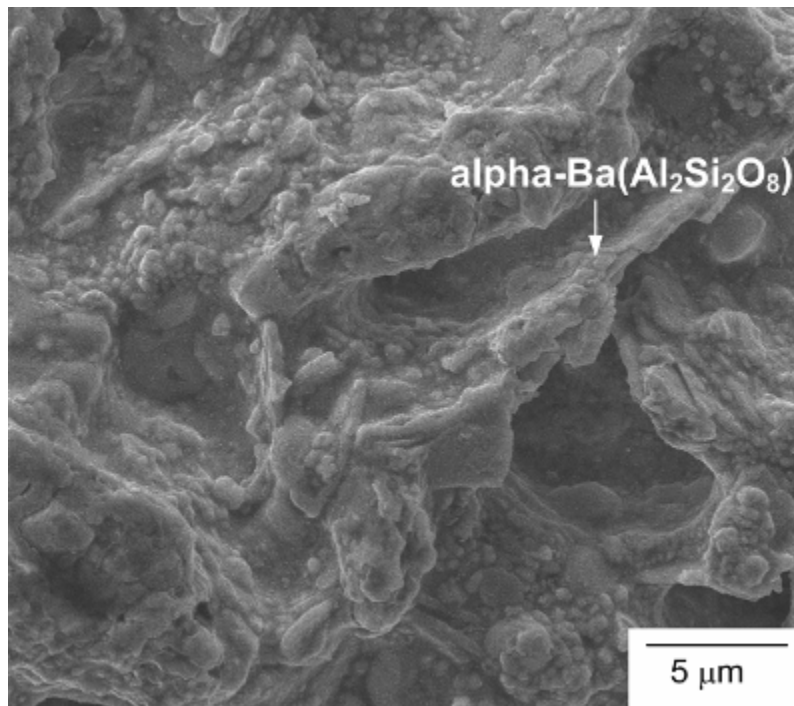


(b)

Fig. 33    SEM micrographs of the microstructure of various color regions in Fig. 21(c): (a) yellow region; (b) pink region; (c) red region; (d) brown region.
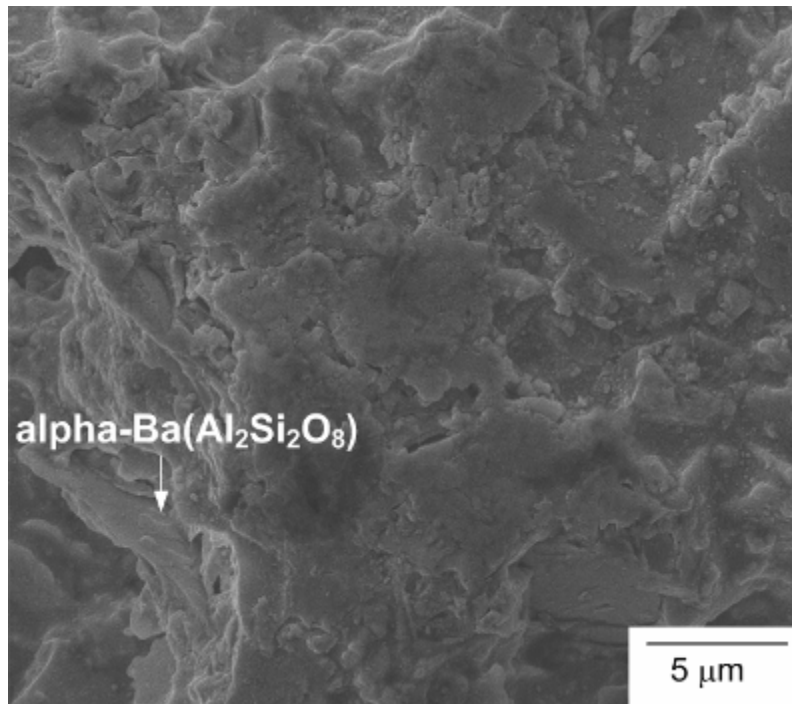
(c)



(d)
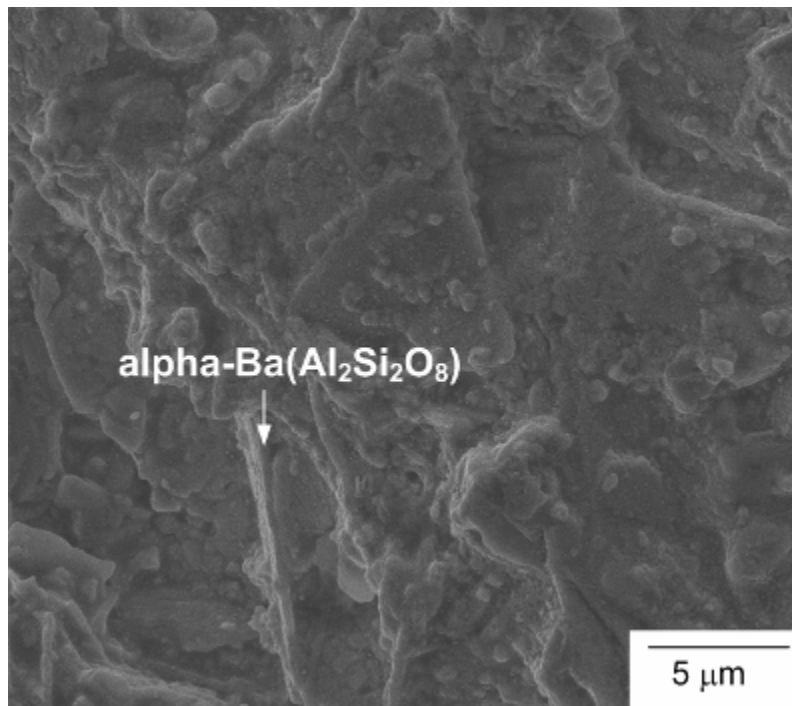
Fig. 33    (continued)
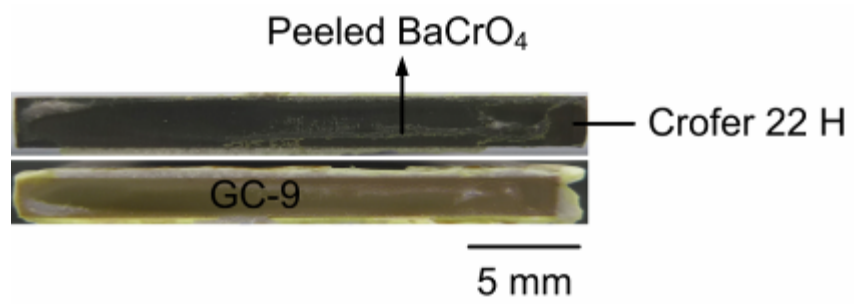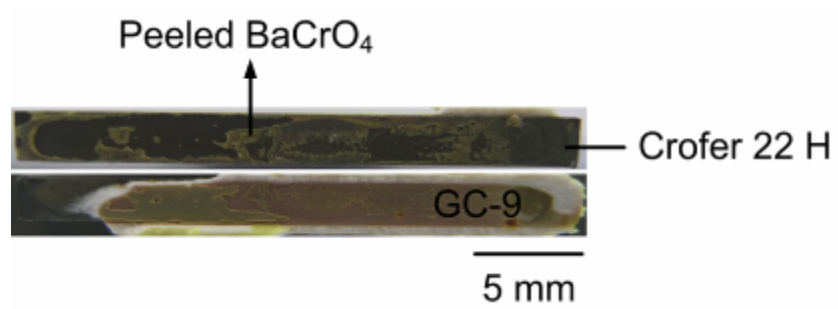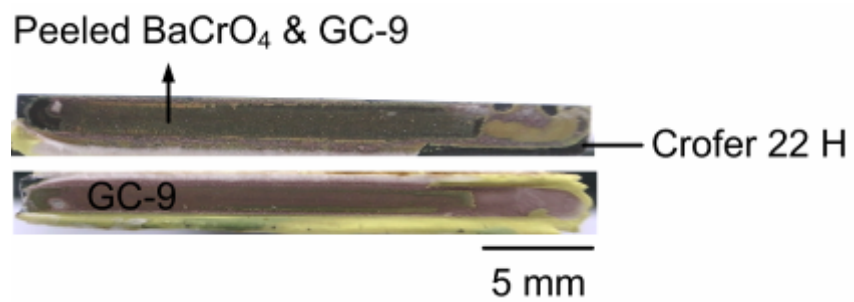
Fig. 34    Failure patterns in the tensile specimens tested at 800 $^{\circ}$C: (a) short creep rupture time; (b) medium-term creep rupture time; (c) long creep rupture time.
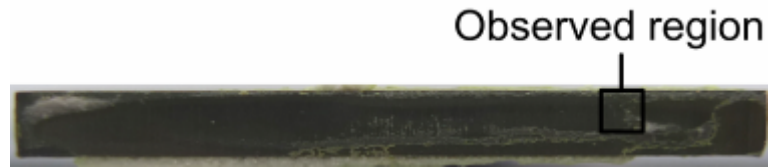
(a)
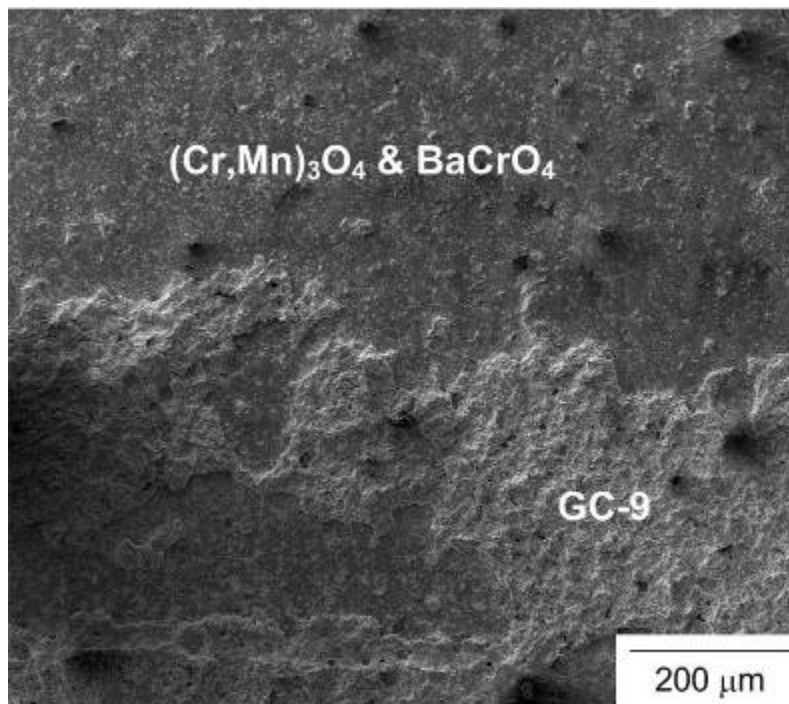


(b)

Fig. 35 A fracture surface region of the tensile specimen shown in Fig. 33(a): (a) optical micrograph showing the observed region of SEM; (b) SEM micrograph of the outlined region; (c) microstructure of the spinel layer buried in the chromate layer; (d) microstructure of GC-9 substrate.
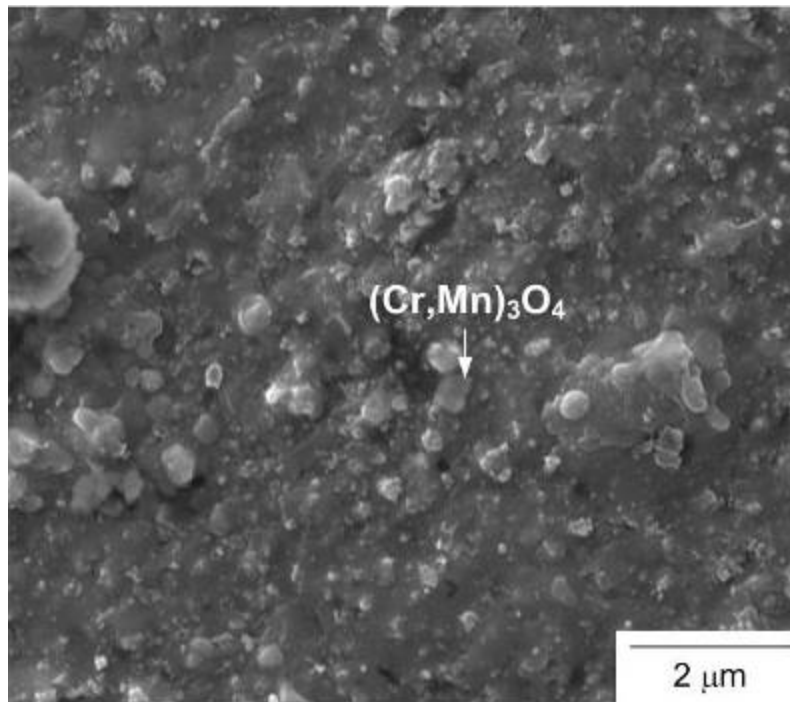
(c)
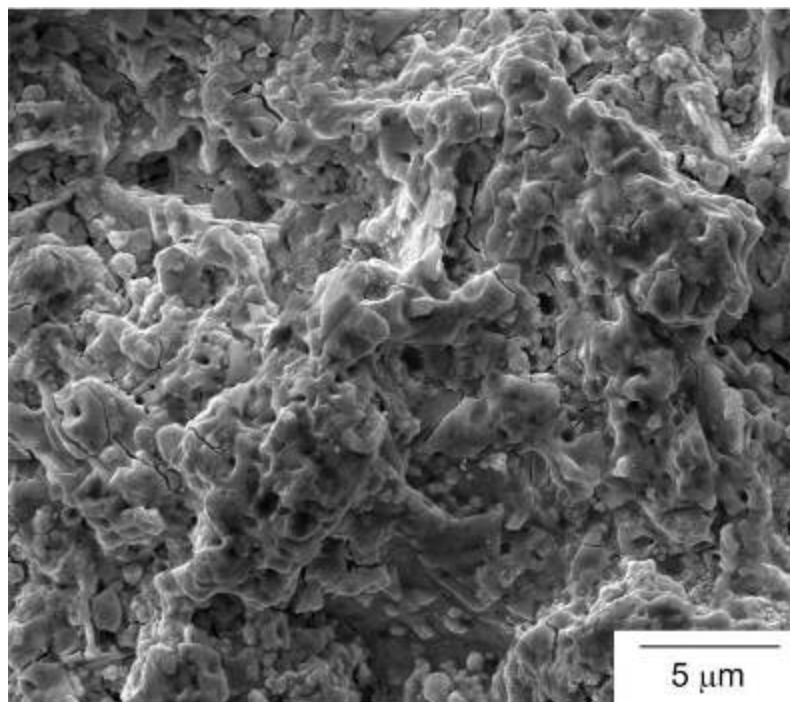


(d)

Fig. 35    (continued)
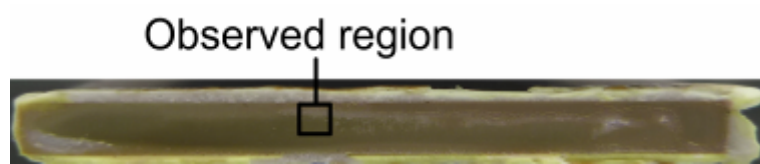
(a)
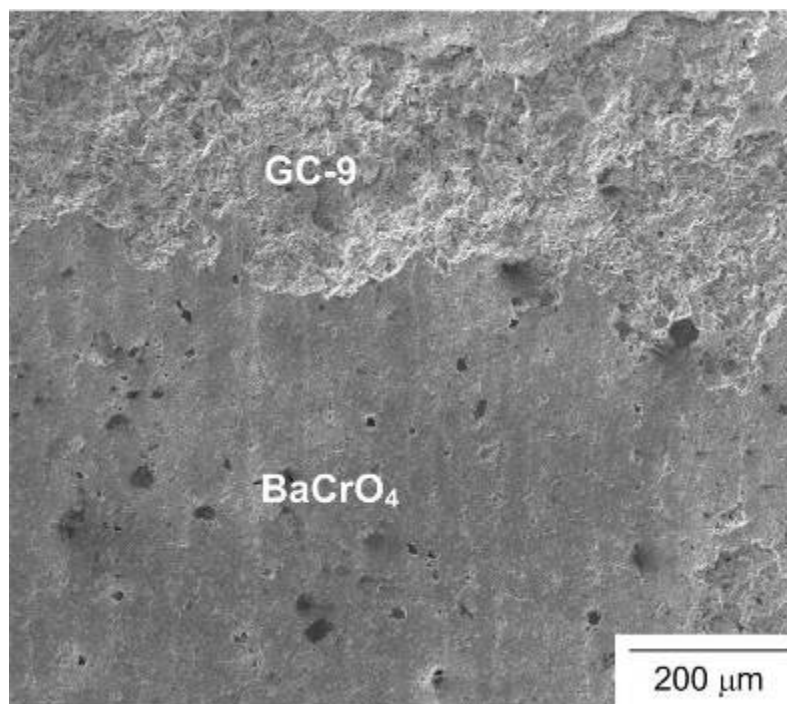


(b)

Fig. 36  A fracture surface region of the tensile specimen shown in Fig. 33(a): (a) optical micrograph showing the observed region of SEM; (b) SEM micrograph of the outlined region; (c) microstructure of chromate layer.

(c)

Fig. 36    (continued)

Observed region
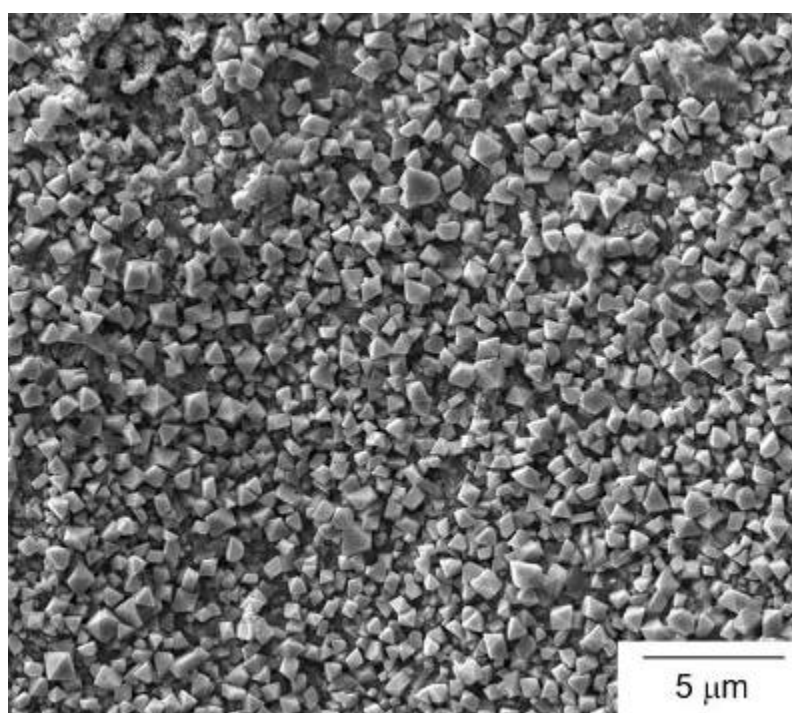
(a)



(Cr,Mn)$_3$O$_4$ & BaCrO$_4$

GC-9

200 μm
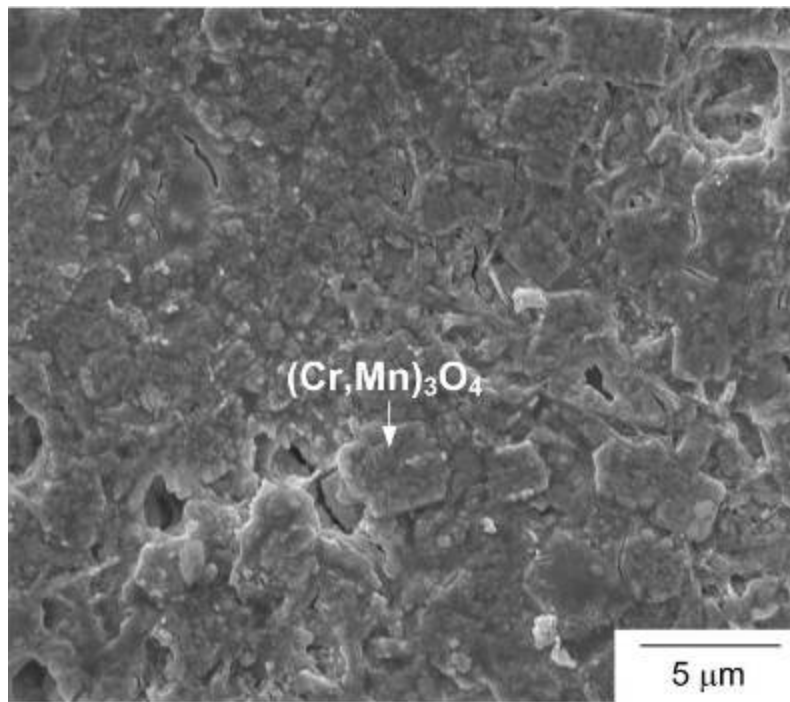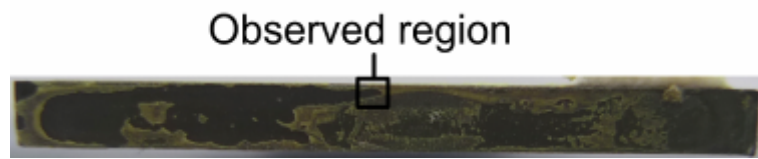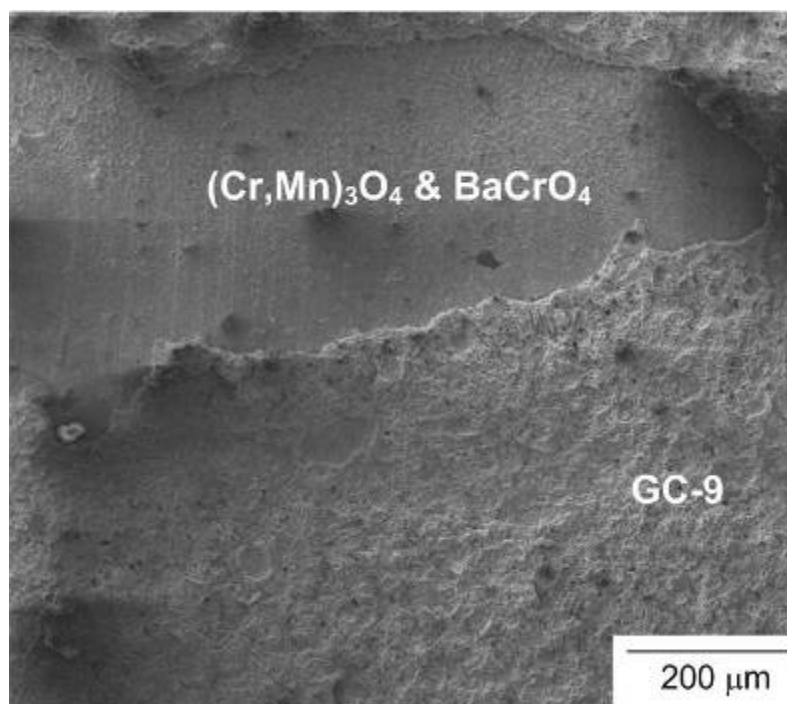
(b)

Fig. 37    A fracture surface region of the tensile specimen shown in Fig. 33(b): (a) optical micrograph showing the observed region of SEM; (b) SEM micrograph of the outlined region; (c) microstructure of the spinel layer buried in the chromate layer; (d) microstructure of GC-9 substrate with residual chromate.
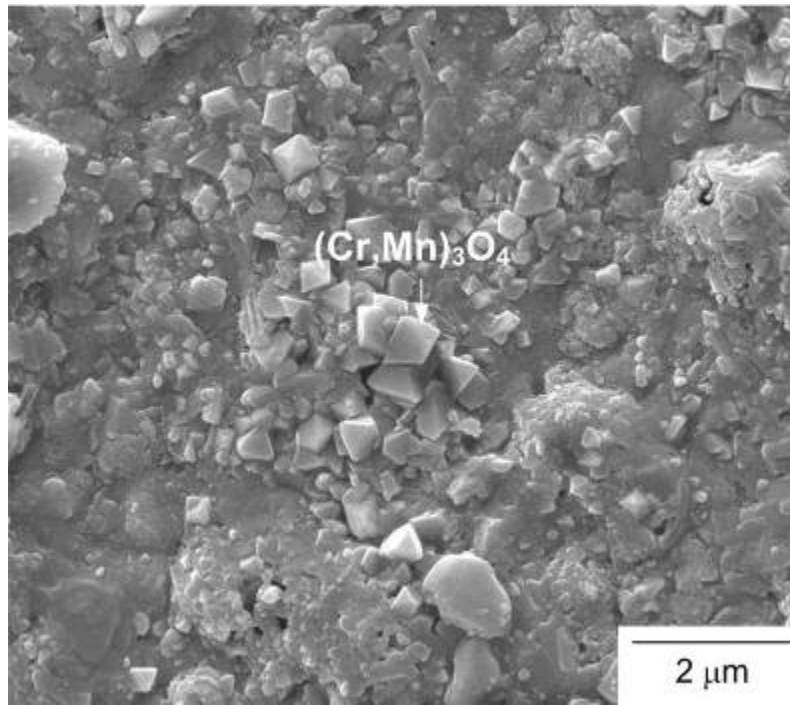
(c)



(d)

Fig. 37    (continued)
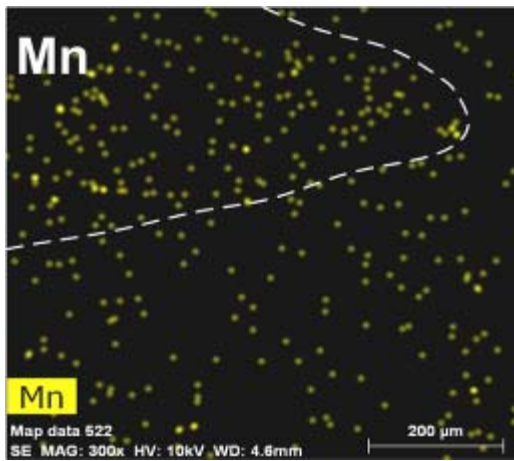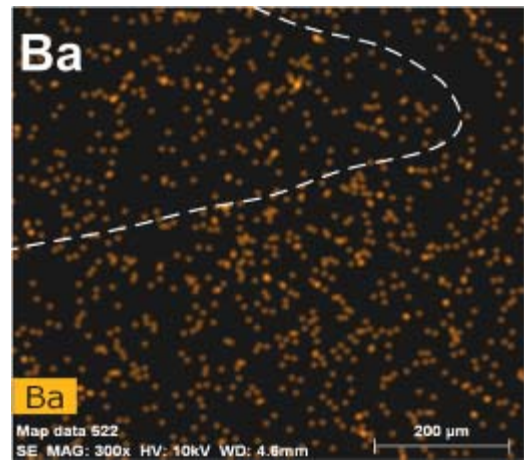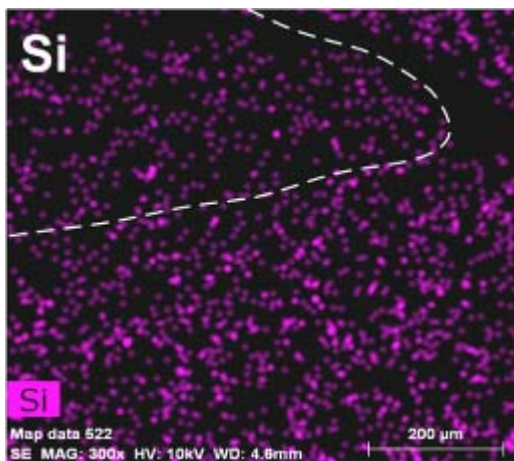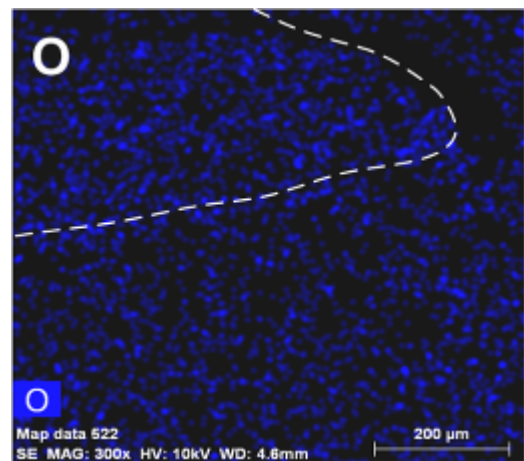
Fig. 38  EDS mapping of elements on the outlined fracture surface region of the tensile
specimen shown in Fig. 36(b): (a) mapping region; (b) Cr; (c) Mn; (d) Ba; (e) Si;
(f) O.
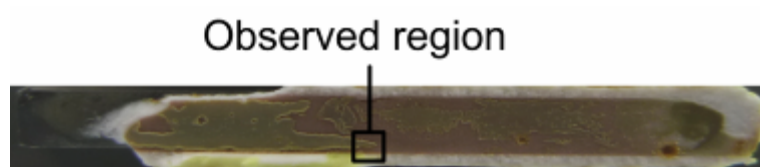
(a)
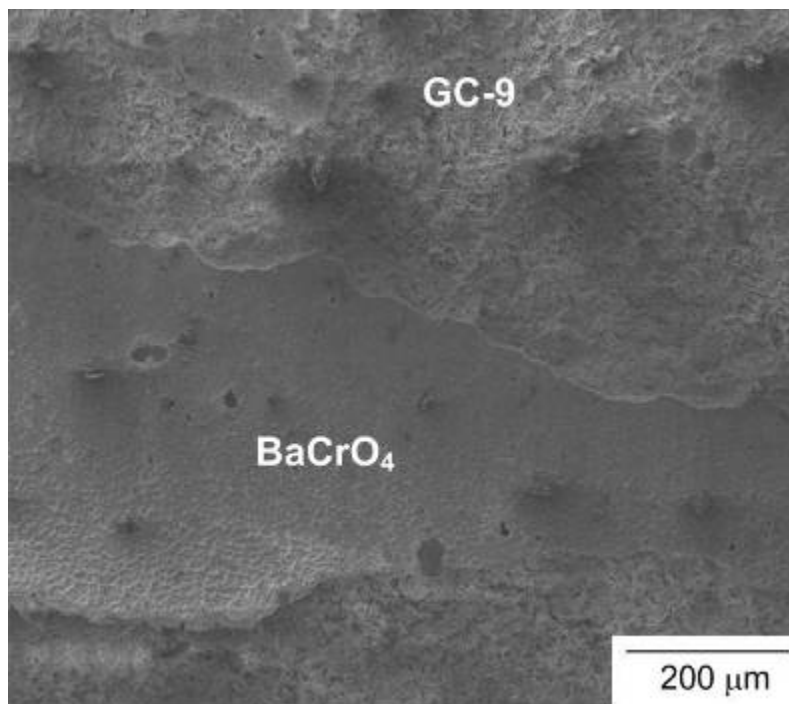


(b)

Fig. 39    A fracture surface region of the tensile specimen shown in Fig. 33(b): (a) optical micrograph showing the observed region of SEM; (b) SEM micrograph of the outlined region; (c) microstructure of the chromate layer; (d) microstructure of GC-9 substrate with residual chromate.
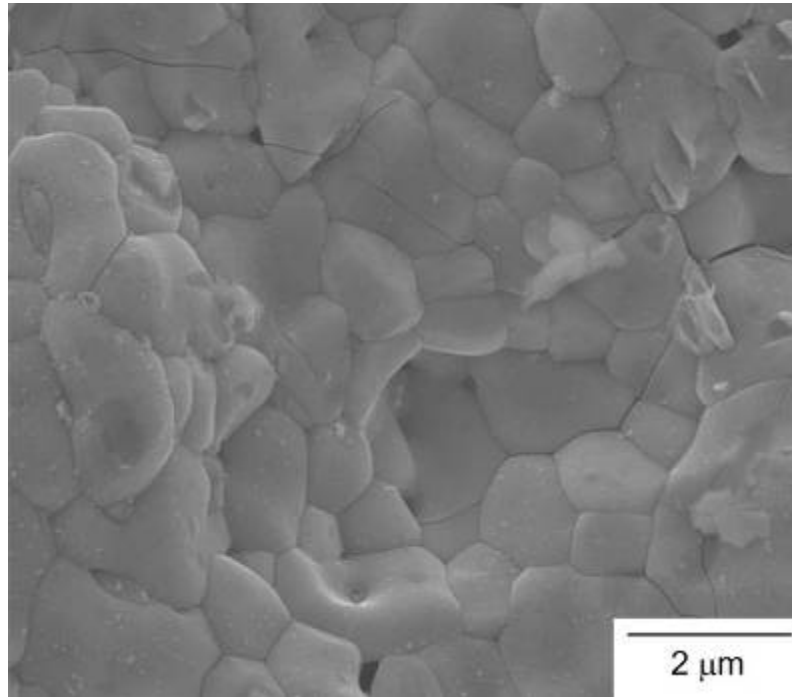
(c)



(d)
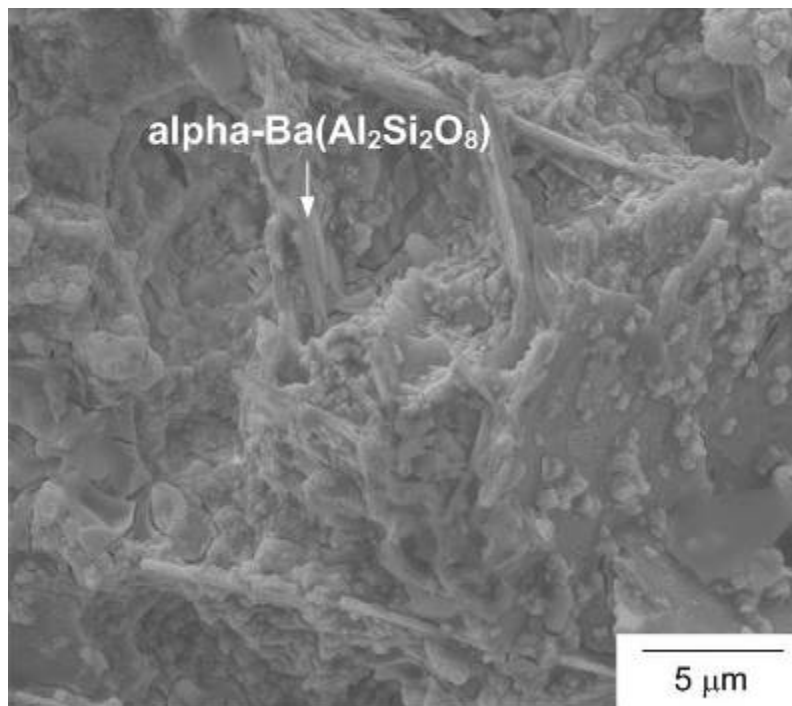
Fig. 39    (continued)
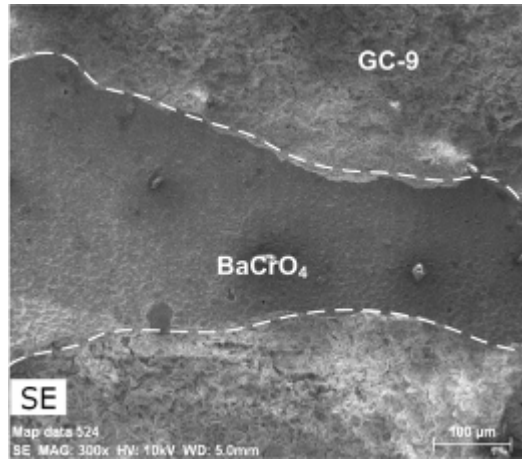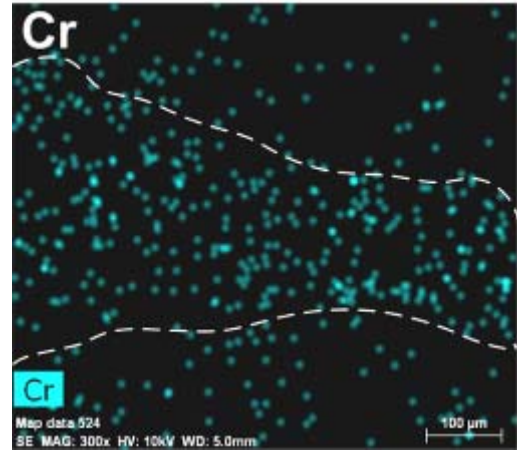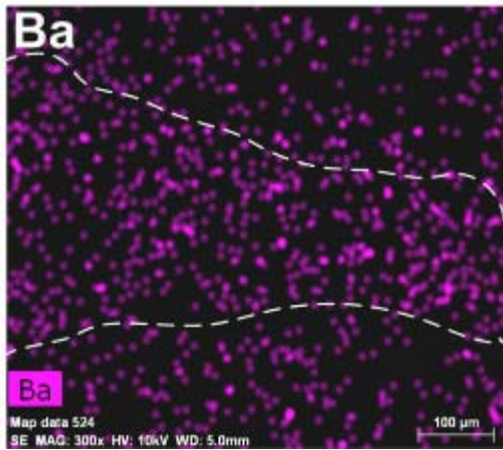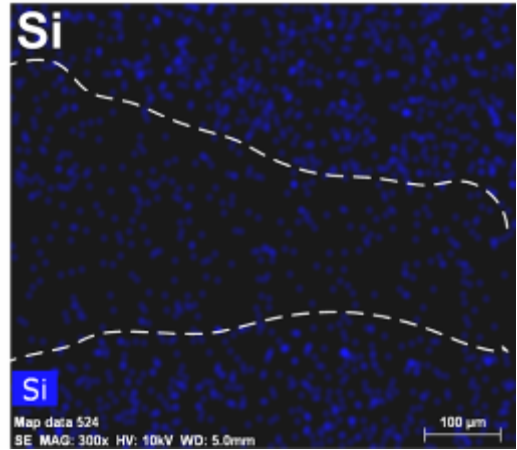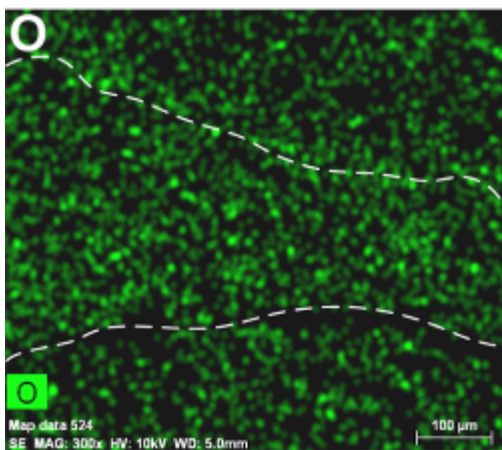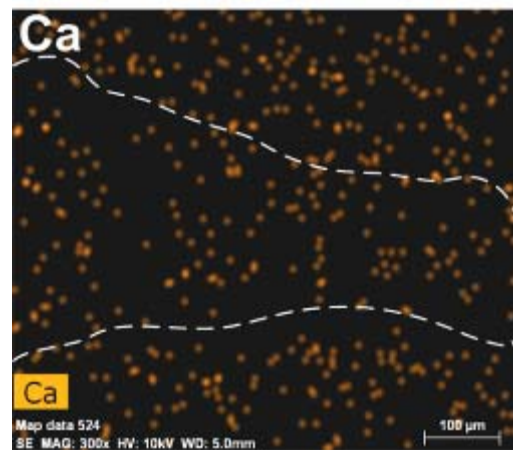
Fig. 40    EDS mapping of elements on the outlined fracture surface region of the tensile
specimen shown in Fig. 38(b): (a) mapping region; (b) Cr; (c) Ba; (d) Si; (e) O;
(f) Ca.

Observed region

(a)



GC-9

$(Cr,Mn)_3O_4$

500 μm
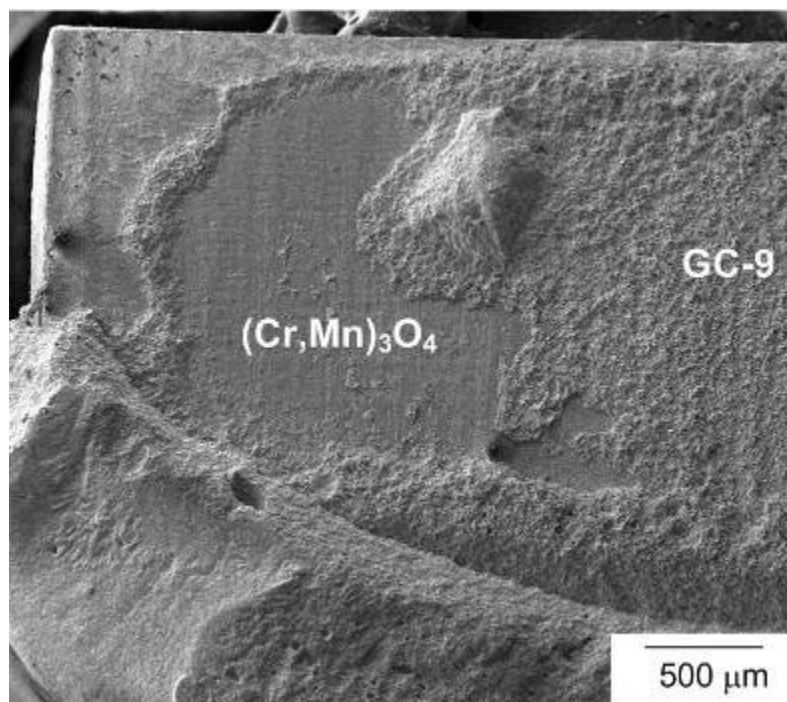
(b)

Fig. 41    A fracture surface region of the tensile specimen shown in Fig. 33(c): (a) optical micrograph showing the observed region of SEM; (b) SEM micrograph of the outlined region; (c) microstructure of the spinel layer.

(c)

Fig. 41    (continued)

(a)



500 μm
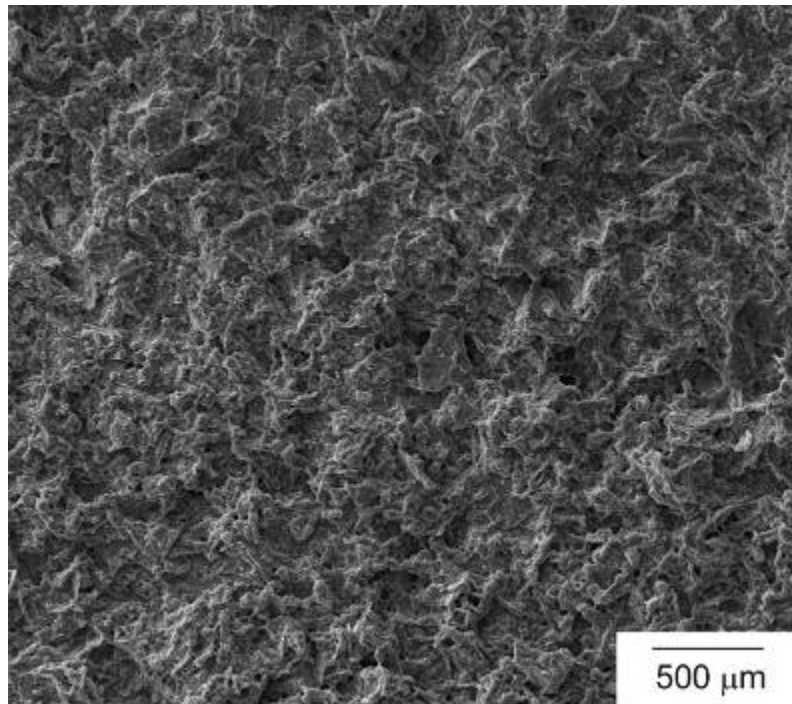
(b)

Fig. 42　A fracture surface region of the tensile specimen shown in Fig. 33(c): (a) optical micrograph showing the observed regions of SEM; (b) SEM micrograph of region 1; (c) SEM micrograph of region 2.
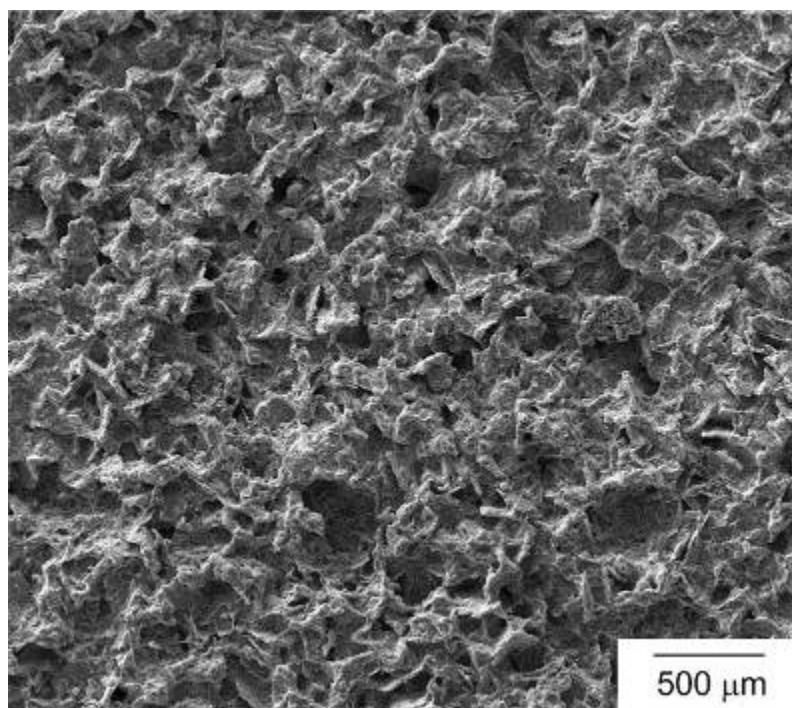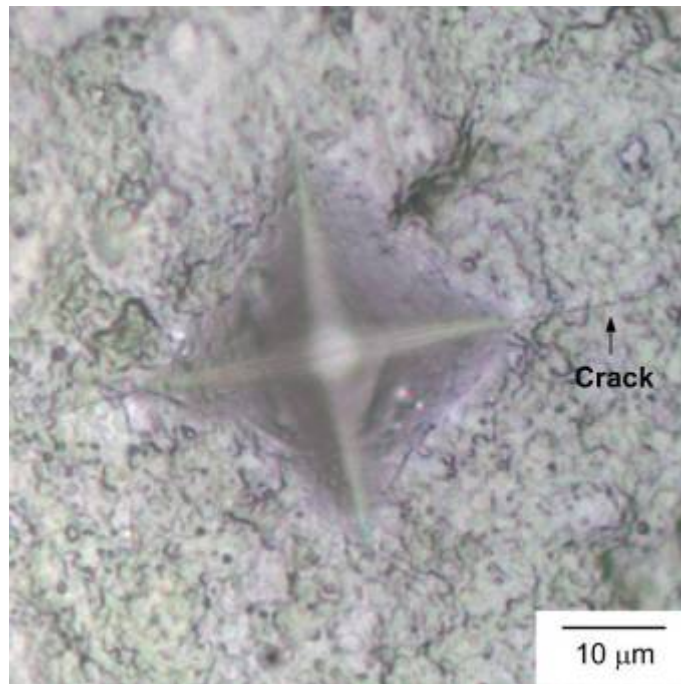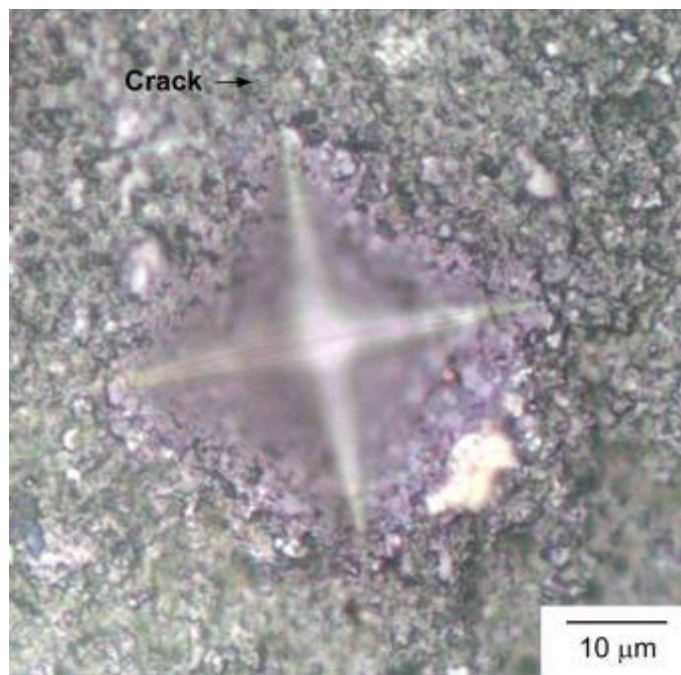
(c)

Fig. 42    (continued)
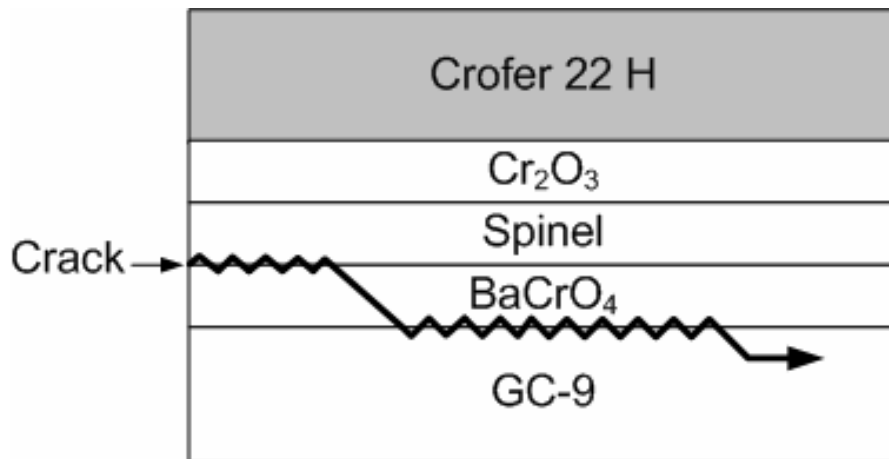
Fig. 43    Schematic of creep crack propagation path in joint specimens.
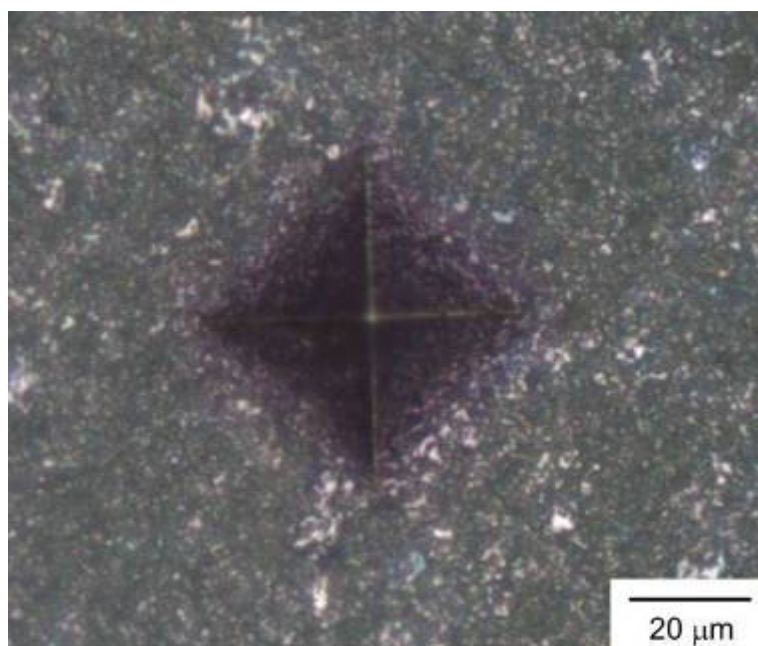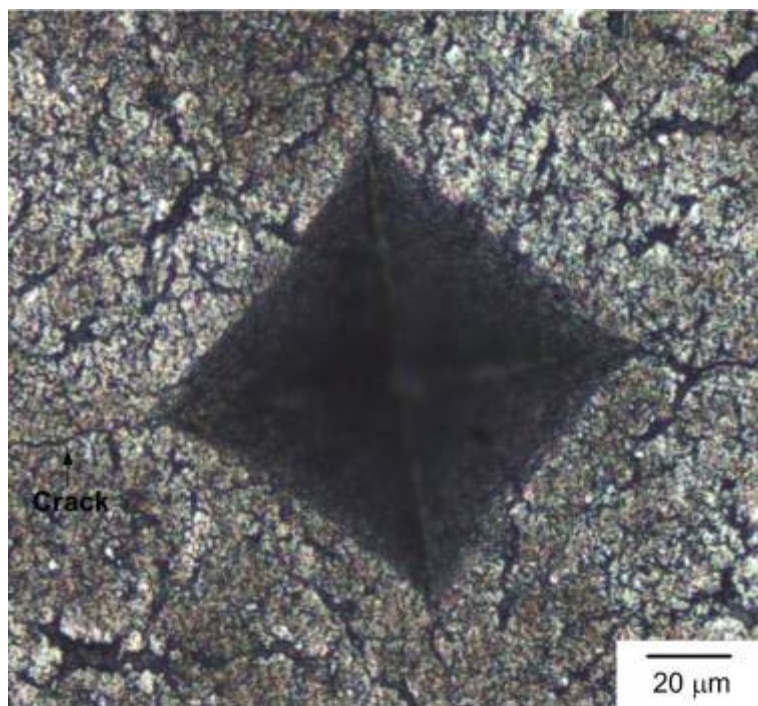
(a)



(b)

Fig. 44   Vickers indentation impressions on a half cell: (a) anode side; (b) electrolyte
         side.

(a)



(b)

Fig. 45　Vickers indentation impressions on a full cell: (a) anode side; (b) cathode side.